UNIVERSITY OF SOUTHAMPTON

FACULTY OF PHYSICAL AND APPLIED SCIENCES

School of Physics and Astronomy

Southampton High Energy Physics Group

The Evaluation of $K \to \pi\pi$ Decay Amplitudes from Lattice Quantum Chromodynamics

by

Elaine Jennifer Goode

Presented for the degree of

Doctor of Philosophy

July 2012

UNIVERSITY OF SOUTHAMPTON

ABSTRACT

FACULTY OF PHYSICAL AND APPLIED SCIENCES

School of Physics and Astronomy

DOCTOR OF PHILOSOPHY

THE EVALUATION OF $K \to \pi\pi$ DECAY AMPLITUDES FROM LATTICE QUANTUM CHROMODYNAMICS

by Elaine Jennifer Goode

We present results for the $\Delta I = 3/2$ $K \to \pi\pi$ decay amplitude computed using lattice quantum chromodynamics. The calculation is performed using $2+1$ flavours of domain wall fermion and the Iwasaki gauge action modified by the dislocation suppressing determinant ratio, on a lattice volume of $32^3 \times 64 \times 32$ at lattice spacing $a^{-1} = 1.364$ GeV. The resulting valence pion mass is $m_\pi = 142.11$ MeV, and the kaon mass is $m_K = 505.5$ MeV. A total of 146 configurations are analysed, giving $\mathrm{ReA}_2 = 1.381(46)_{\mathrm{stat}}(258)_{\mathrm{syst}} \times 10^{-8}$ GeV and $\mathrm{ImA}_2 = -6.54(46)_{\mathrm{stat}}(120)_{\mathrm{syst}} \times 10^{-8}$ GeV. The experimental results for ReA_0 and ReA_2 and ϵ'/ϵ are combined with this lattice result for ImA_2 to give $\mathrm{ImA}_0/\mathrm{ReA}_0 = -1.61(28) \times 10^{-4}$.

We also present reslts from a second calculation where both the $\Delta I = 1/2$ and $\Delta I = 3/2$ $K \to \pi\pi$ decay amplitudes are calculated. This calculation is performed using $2+1$ flavours of domain wall fermions with the Iwasaki gauge action and a lattice size of $16^3 \times 32 \times 16$. Since the evaluation of A_0 is technically challenging, this first ever determination of A_0 is performed at threshold with a heavy pion mass of $m_\pi \sim 420$ MeV. The results are $\mathrm{Re}(A_0) = 3.80(82) \times 10^{-7}$ GeV and $\mathrm{Im}(A_0) = -2.5(2.2) \times 10^{-11}$ GeV.

Contents

List of Figures

List of Tables

Declaration of Authorship

Chapters 1, 2 and 4 are almost exclusively background material, the content of which is drawn from various text books and review articles, and for which I make no claim of originality. In particular, I found the following to be helpful when writing:

- J. F. Donoghue, E. Golwich and B. Holstein, *Dynamics of the Standard Model* [1]
- C. Gatringer and C. B. Lang, *Quantum Chromodynamics on the Lattice* [2]
- The Particle Data Group, *The Review of Particle Physics* [3].

In Chapter 3 the Wilson coefficients are calculated using the equations in [4]. Although I did not work directly on the evaluation of the NPR factors in Chapter 5, a discussion of this calculation has been included for completeness.

I worked directly on all the computations and analysis presented in chapters 7-9. In particular I evaluated all the Wick contractions for the $K \to \pi\pi$ decays, wrote code for these contractions using UKhadron and tested this code against existing CPS code using sample lattices. I made a full and independent analysis of all the data that contribute to the evaluation of the lattice $K \to \pi\pi$ matrix elements and Lellouch-Lüscher finite volume corrections in both chapters 8 and 9.

Chapter 8 briefly makes reference to a calculation of the $K \to \pi\pi$ matrix elements on quenched lattices. I worked directly on the analysis for this quenched calculation, although the results of this calculation have not been included in this thesis.

Chapter 8 includes a comprehensive error budget for the final calculation. I worked directly on the contributions to this error budget from the unphysical kinematics,

the derivative of the phase shift, the Wilson coefficients and the uncertainties in the renormalisation. However, I do not claim credit for three of the contributions to the error budget. The estimate of the error due to partial quenching is taken from work Matthew Lightman presented in his doctoral thesis [5], the estimate of the error due to discretisation errors was written by Chris Kelly and the estimate of the error due to the finite volume was written by Matthew Lightman. These three contributions have been included for completeness.

This thesis contains work which has previously been published in the following journals

- T. Blum et al, Phys. Rev. Lett. **108**(2012) 141601 [arXiv:1111.1699[hep-lat]][6]
- T. Blum et al, *K to $\pi\pi$ Decay amplitudes from Lattice QCD*, Phys. Rev. **D84**, 114503 (2011) [arXiv:1106.2714[hep-lat]][7]

along with

- T. Blum et al, *Lattice determination of the $K \to (\pi\pi)_{I=2}$ Decay Amplitude A_2*, [arXiv:1206.5142[hep-lat]], (awaiting publication).

I also contributed to the work presented at several lattice conferences:

- E. Goode and M. Lightman, PoS **LATTICE2011**, 335,(2011),[arXiv:1111.4889[hep-lat]] [8]
- Goode, E. J. and Lightman, M, PoS **LATTICE2010**, 313, [arXiv:1101.2473[hep-lat]] [9]
- Lightman, Matthew and Goode, Elaine, PoS **LAT2009**, 254 (2009), [arXiv:0912.1667[hep-lat]] [10]

Signed: .....

Date: .....

Acknowledgements

I would like to thank my supervisor Chris Sachrajda, for his support, instruction, patience and guidance throughout my Ph.D. and while completing this project. I would also like to thank him for the sympathy he showed me during the stressful period when I was learning to drive. I benefited from the help of all of my colleagues in the RBC and UKQCD collaborations. In particular, I worked closely with Dirk Brömmel, Matthew Lightman, Qi Liu and Andrew Lytle, and am grateful to each one of them for answering the many questions I had during the course of this work. I have enjoyed working as part of the SHEP group at Southampton, where I have found the environment to be friendly and enriching. Seb has provided me with constant love and support over the last three years. Finally, I would like to thank my parents.

Chapter 1

Introduction

A quantitative understanding of the origin of CP-violation, both within and beyond the Standard Model, remains one of the principal goals of particle physics research. It was in 1964 that indirect CP-violation in $K \to \pi\pi$ decays was first discovered [11], demonstrating that the neutral kaon mass eigenstates were not CP eigenstates. More than twenty years after this discovery, direct CP-violation was observed in neutral kaon decays [12, 13, 14, 15], where the CP-odd eigenstate of a neutral kaon can decay to a two-pion state, which is CP-even.

Direct CP violation is characterised by the parameter $\mathrm{Re}(\epsilon'/\epsilon)$, which will be defined in Chapter 2. While forty years of experimental effort have produced the measured result $\mathrm{Re}(\epsilon'/\epsilon) = 1.65(26) \times 10^{-3}$ [3], with only a 16% error, there is no reliable theoretical calculation of this quantity based on the Standard Model.

The Cabibbo-Kobayashi-Maskawa (CKM) theory for the weak interactions of the quarks, when combined with QCD, provides a framework describing in complete detail all the properties and interactions of the six quarks. This framework appears capable of explaining all observed phenomena in which these quarks participate. However, to date, the non-perturbative character of low energy QCD has obscured many of the consequences of the CKM theory. In particular, both the direct CP violation seen in K meson decays and the factor of 22.5 enhancement of the $I = 0$, $K \to \pi\pi$ decay amplitude A_0 relative to the $I = 2$ amplitude A_2 (the $\Delta I = 1/2$ rule) lack a quantitative explanation.

Calculations of the $K \to \pi\pi$ decay amplitudes are usually studied in the framework of a low-energy effective theory, where the Hamiltonian is written in terms of local low-energy operators, and the high energy effects of the W-boson and heavy quarks are encoded in Wilson coefficients which can be calculated in perturbation theory. Wilson coefficients evaluated at a QCD scale of about 2 GeV represent the short distance physics and can be evaluated from the CKM theory using QCD and electro-weak perturbation theory. However, these factors explain only a factor of two enhancement of the $I = 0$ amplitude [16, 17]. The remaining enhancement must arise from the hadronic matrix elements which require non-perturbative treatment.

Direct CP violation in kaon decays provides a critical test of the Standard Model's CKM mechanism of CP violation. Lattice QCD provides the opportunity of computing the non-perturbative QCD effects in general and in hadronic CP-violating processes in particular. A direct lattice calculation of $K \to \pi\pi$ decay is extremely important to provide an explanation for the $\Delta I = 1/2$ rule and to test the standard model of CP violation from first principles. A previous lattice QCD calculation using 2+1 dynamical domain wall fermions failed to give a conclusive result because of the large systematic errors associated with the use of chiral perturbation theory at the scale of the kaon mass [18]. However, there are on-going efforts using chiral perturbation theory [19]. Earlier quenched results [20, 21] are subject to this same difficulty together with uncontrolled uncertainties associated with quenching [22, 23, 24].

Major progress has been made in this thesis by peforming a calculation at nearly-physical kinematics of the (complex) decay amplitude A_2, corresponding to the decay in which the two-pion final state has isospin 2. This represents the first realistic *ab initio* calculation of a weak hadronic decay in Lattice QCD and forms the main result of this thesis. The lattice ensemble on which this calculation is performed is referred to in the Table of Contents and List of Figures as the IDSDR lattices.

The evaluation of the isospin= 0 amplitude is an unusually difficult calculation because a contribution from the vacuum obscures the $K \to \pi\pi$ signal. The $K \to \pi\pi$

signal decays exponentially in Euclidean time while the vacuum contribution is constant in time. Consequently, extracting the $K \to \pi\pi$ signal from the noisy background vacuum contribution requires the collection of large statistics. However, with the continuing increase of available computing power and the development of improved algorithms, calculations of this kind are now no longer out of reach.

This thesis takes a major step towards the computation of the physical $I = 0$ $K \to \pi\pi$ amplitudes by performing a complete calculation at unphysical kinematics with pions of mass 422 MeV at rest in the kaon rest frame. With this simplification it has been possible to resolve $\mathrm{Re}A_0$ from zero for the first time, with a 25% statistical error. Methods for computing the complete, complex amplitude A_0, a calculation central to understanding the $\Delta = 1/2$ rule and testing the standard model of CP violation in the kaon system, have also been developed. The lattices on which this calculation is performed are referred to in the Table of Contents and List of Figures as the 16^3 Iwasaki lattices.

The format for the rest of this thesis is as follows. In Chapter 2 an introduction to kaon phenomenology and CP violation within the Standard Model is given. This chapter defines the conventions used throughout the remainder of the thesis for the $K \to \pi\pi$ decay amplitudes and CP violating parameters ϵ' and ϵ. Chapter 3 establishes the theoretical framework for the calculation of the $K \to \pi\pi$ decay in terms of the operator product expansion. The basis of operators used in the calculation is made explicit and a description of how the high-energy contributions are included in the form of Wilson coefficients is given. An introduction to Lattice QCD is presented in Chapter 4, and the calculation of the renormalisation constants which relate the bare operators used in the lattice calculation to suitably renormalised operators is given in Chapter 5. The lattice evaluation of $K \to \pi\pi$ decays must necessarily take place in a finite volume. A detailed description of how to account for this finite volume in the case of a two-pion final state is given in Chapter 6. Technical details relating to the lattice calculation of $K \to \pi\pi$ decays in general are given in Chapter 7. The main work of this thesis, a calculation of A_2 at nearly-physical kinematics, is presented in Chapter 8. Chapter 9 includes the results from the first ever calculation of A_0, albeit at unphysical kinematics. In the

final chapter the conclusions from Chapters 8 and 9 are drawn together.

Chapter 2

Kaon Phenomenology and CP Violation

This chapter begins with an introduction to the phenomenology of $K \to \pi\pi$ decays and a definition of the conventions that will be used throughout the remainder of the thesis. The chapter then goes on to discuss CP violation in neutral kaon decays, before parameterising the CP violation in terms of $K \to \pi\pi$ decay amplitudes.

2.1 Phenomenology

Single pions have isospin $I = 1$, with the third component of isospin, $I_z = 1, 0, -1$ for π^+, π^0 and π^- respectively. A state containing two pions may then have isospin $I = 0$, 1 or 2. In the decays of $K \to \pi\pi$, the two final state pions are in an $l = 0$ state. In order to obtain a symmetric state the total isospin must therefore be even. This restricts the pions to be in a state with $I = 0$ or $I = 2$. Since kaons, which contain one s-quark and one light quark have isospin $I = 1/2$, transitions to an $I = 0$, 2 final state are referred to as $\Delta I = 1/2$ and $\Delta I = 3/2$ respectively.

The $K \to \pi\pi$ decay amplitudes with isospin I and third component of isospin I_z are defined as follows:

$$A_I = \sqrt{2}\left\langle (\pi\pi)^I_{I_z=0} | \mathcal{L} | K^0 \right\rangle, \tag{2.1}$$

where the two-pion states of definite isospin are

$$\left|(\pi\pi)^{I=2}_{I_z=2}\right\rangle = \left|\pi^+\pi^+\right\rangle \tag{2.2a}$$

$$\left|(\pi\pi)^{I=2}_{I_z=1}\right\rangle = \frac{1}{\sqrt{2}}\left\{\left|\pi^+\pi^0\right\rangle + \left|\pi^0\pi^+\right\rangle\right\} \tag{2.2b}$$

$$\left|(\pi\pi)^{I=2}_{I_z=0}\right\rangle = \frac{1}{\sqrt{6}}\left\{\left|\pi^+\pi^-\right\rangle + 2\left|\pi^0\pi^0\right\rangle + \left|\pi^-\pi^+\right\rangle\right\} \tag{2.2c}$$

and

$$\left|(\pi\pi)^{I=0}_{I_z=0}\right\rangle = \frac{1}{\sqrt{3}}\left\{\left|\pi^+\pi^-\right\rangle - \left|\pi^0\pi^0\right\rangle + \left|\pi^-\pi^+\right\rangle\right\}. \tag{2.2d}$$

In order to establish the conventions used throughout this calculation, the $K \to \pi\pi$ decay widths, which are measured experimentally, are written in terms of the following decay amplitudes:

$$A_{K^+\to\pi^+\pi^0} \equiv A_{+0} = \left\langle \pi^+(p)\pi^0(-p)\right| \mathcal{L}_W \left|K^+\right\rangle \tag{2.3a}$$

$$A_{K_S\to\pi^+\pi^-} \equiv A_{+-} = \left\langle \pi^+(p)\pi^-(-p)\right| \mathcal{L}_W \left|K_S\right\rangle \tag{2.3b}$$

$$A_{K_S\to\pi^0\pi^0} \equiv A_{00} = \left\langle \pi^0(p)\pi^0(-p)\right| \mathcal{L}_W \left|K_S\right\rangle. \tag{2.3c}$$

In terms of these amplitudes, the corresponding decay widths are

$$\Gamma_{+0} = \frac{1}{8\pi}|A_{+0}|^2 \frac{\sqrt{m^2_{K^+}/4 - (m^2_{\pi^+} + m^2_{\pi^0})/2 + (m^2_{\pi^0} - m^2_{\pi^+})^2/4m^2_{K^+}}}{m^2_{K^+}} \tag{2.4a}$$

$$\Gamma_{+-} = \frac{1}{8\pi}\frac{|A_{+-}|^2}{m^2_{K_S}}\sqrt{\frac{m^2_{K_S}}{4} - m^2_{\pi^+}} \tag{2.4b}$$

$$\Gamma_{00} = \frac{1}{16\pi}\frac{|A_{00}|^2}{m^2_{K_S}}\sqrt{\frac{m^2_{K_S}}{4} - m^2_{\pi^0}}. \tag{2.4c}$$

The amplitudes in Eq. (2.3) can then be parametrised in terms of A_0 and A_2 as

follows:

$$\begin{aligned} A_{+-} &= \sqrt{\frac{2}{3}} A_2 e^{i\delta_2} + \frac{2}{\sqrt{3}} A_0 e^{i\delta_0} \\ A_{00} &= 2\sqrt{\frac{2}{3}} A_2 e^{i\delta_2} - \frac{2}{\sqrt{3}} A_0 e^{i\delta_0} \\ A_{+0} &= \sqrt{\frac{3}{2}} A_2^+ e^{i\delta_2}. \end{aligned} \tag{2.5}$$

Final state interactions of the two pions introduce the $\pi\pi$ phase shifts δ_I as described by Watson's Theorem [25]. This follows from the unitarity of the scattering operator, which is used to provide a constraint for the transition operator T, where T is defined by $S = 1 - iT$. Matrix elements of T must obey

$$i(\langle f|T|i\rangle - \langle i|T|f\rangle^*) = \sum_n \langle n|T|f\rangle^* \langle n|T|i\rangle \,. \tag{2.6}$$

In the special case of $K \to \pi\pi$ followed by a strong final-state interaction of the two pions, $i = K$ and $n = f = \pi\pi$. If the weak and strong matrix elements are denoted $|T_W|e^{i\delta_W}$ and $|T_S|e^{i\delta_S}$ it follows from time-reversal invariance that $\delta_W = \delta_S$

In the presence of isospin violation, a $\Delta I = 5/2$ contribution will distinguish between the amplitudes A_2 and A_2^+ entering in the K^0 and K^+ decays respectively. There are two sources of isospin breaking in the Standard Model. These are strong isospin breaking due to $m_u \neq m_d$ and electromagnetic corrections. Electromagnetic isospin breaking has $I = 0, 1, 2$ components, while to $\mathcal{O}(m_u - m_d)$, strong isospin breaking is purely $I = 1$. Thus a $\Delta I = 5/2$ $K \to \pi\pi$ transition can arise from either a $\Delta I = 3/2$ transition combined with strong isospin breaking effects, or a $\Delta I = 1/2$ transition followed by the $I = 2$ component of the electromagnetic interaction. In Eqns. 2.7 and 2.8 we will see that the $\Delta I = 1/2$ transition is enhanced compared to the $\Delta I = 3/2$ transition, so the dominant $\Delta I = 5/2$ effect is expected to arise from electromagnetic isospin breaking [26]. However, if isospin breaking effects are ignored then within the Standard Model we have $A_2^+ = A_2$. This is the assumption made throughout this thesis. The effects of isospin breaking in $K \to \pi\pi$ decays and in two-pion scattering have been investigated in several publications, including

Table 2.1: *Parameters used to evaluate A_0 and A_2*

m_{K^+}	493.667 ± 0.016 MeV
m_{K^0}	497.614 ± 0.024 MeV
m_{π^+}	139.57018 ± 0.00035 MeV
m_{π^0}	134.9766 ± 0.0006 MeV
τ_{K_s}	$(0.89530 \pm 0.0005) \times 10^{-10}$ s
τ_{K^+}	$(1.2380 \pm 0.0021) \times 10^{-8}$ s
$\mathrm{Br}(K^0 \to \pi^0\pi^0)$	$(30.69 \pm 0.05)\%$
$\mathrm{Br}(K^0 \to \pi^+\pi^-)$	$(69.20 \pm 0.05)\%$
$\mathrm{Br}(K^+ \to \pi^+\pi^0)$	$(20.66 \pm 0.08)\%$
$\Gamma(K_S \to \pi^0\pi^0)$	$(2.2563 \pm 39) \times 10^{-12}$ MeV
$\Gamma(K_S \to \pi^+\pi^-)$	$(5.0875 \pm 46) \times 10^{-12}$ MeV
$\Gamma(K^+ \to \pi^+\pi^0)$	$(1.0984 \pm 90) \times 10^{-14}$ MeV
$\delta_2 - \delta_0$	$47.7°$

Refs. [26],[27],[28] and [29].

The pion and kaon masses and the kaon decay widths and branching ratios are known experimentally [3]. The relevant branching ratios and meson masses are listed in Tab. 2.1, and using these numbers the experimental decay amplitudes are found to be

$$\begin{aligned} |A_0| &\approx \mathrm{ReA}_0 = 3.3197(14) \times 10^{-7}\mathrm{GeV} \\ |A_2| &\approx \mathrm{ReA}_2 = 1.570(53) \times 10^{-8}\mathrm{GeV} \end{aligned} \tag{2.7}$$

from neutral kaon decays, and

$$\begin{aligned} \mathrm{ReA}_0 &= 3.3201(14) \times 10^{-7}\mathrm{GeV} \\ \mathrm{ReA}_2 &= 1.4787(31) \times 10^{-8}\mathrm{GeV} \end{aligned} \tag{2.8}$$

where A_2 is taken from charged kaon decays.

From Eq. (2.8) the ratio $\mathrm{ReA}_0/\mathrm{ReA}_2 = 22.45$. Although the kaon decays via the W-boson, a calculation which fully takes into accout the QCD corrections is necessary in order to fully understand this enhancement of the $\Delta I = 1/2$ transition, commonly referred to as the $\Delta I = 1/2$ rule.

In the following section CP violation in the neutral kaon sector is discussed. In chapter 2.3 it will become clear that the isospin amplitudes A_0 and A_2 feature in the description of CP-violation within the neutral kaon sector.

2.2 Mass matrix phenomenology in the neutral kaon system

The subject of CP violation in the neutral kaon sector is related to the mixing between the K^0 and $\bar{K}^0$. In describing the mixing of neutral kaons, it is convenient to write the neutral kaon system in terms of a two-component column vector

$$|\psi(t)\rangle \equiv \begin{pmatrix} a(t) \\ b(t) \end{pmatrix} = a(t) \left|K^0\right\rangle + b(t) \left|\bar{K}^0\right\rangle . \tag{2.9}$$

The time development is described in terms of the hamiltonian H

$$i\frac{d}{dt} |\psi(t)\rangle = H |\psi(t)\rangle ,$$

where H is non hermitian in order to allow for kaon decays. If H were hermitian the above equation would only describe mixing in the $K^0 - \bar{K}^0$ system. It is possible to write H in terms of two hermitian matrices, $H = M - i\frac{\Gamma}{2}$. The diagonal elements of M and Γ are associated with flavour conserving transitions, while the off-diagonal elements describe mixing between the K^0 and $\bar{K}^0$ states. Since M and Γ are hermitian, it must be the case that $M_{12}^* = M_{21}$ and $\Gamma_{12}^* = \Gamma_{21}$. The diagonal elements of H are equal by CPT invariance, leading to the general form

$$M - i\frac{\Gamma}{2} = \begin{pmatrix} A & p^2 \\ q^2 & A \end{pmatrix} . \tag{2.10}$$

The states $\left|K^0\right\rangle$ and $\left|\bar{K}^0\right\rangle$ are related by the operation CP $\left|K^0\right\rangle = e^{i\xi} \left|\bar{K}^0\right\rangle$, CP $\left|\bar{K}^0\right\rangle = e^{-i\xi} \left|K^0\right\rangle$. In this thesis the CP phase ξ is chosen such that CP $\left|K^0\right\rangle = - \left|\bar{K}^0\right\rangle$. The CP eigenstates $K_\pm^0$ are then

$$\left|K_\pm^0\right\rangle = \frac{1}{\sqrt{2}} \left(\left|K^0\right\rangle \mp \left|\bar{K}^0\right\rangle\right) , \tag{2.11}$$

with

$$\mathrm{CP}\left|K^0_\pm\right\rangle = \pm\left|K^0_\pm\right\rangle. \tag{2.12}$$

Experimentally it is observed that kaon decays are not CP invariant, and so the mass eigenstates of the Hamiltonian, denoted K_L and K_S, are not the CP eigenstates. The parameter $\bar{\epsilon}$ is introduced in order to include this CP-violation in the formalism. The mass eigenstates can then be expressed in terms of the CP eigenstates as follows:

$$\left|K^{L}_{S}\right\rangle = \frac{1}{\sqrt{1+|\bar{\epsilon}|^2}}\left(\left|K^0_\mp\right\rangle + \bar{\epsilon}\left|K^0_\pm\right\rangle\right). \tag{2.13}$$

The names K_L, K_S are clear if one considers the phase space available for the decays. In the limit of CP conservation, $|K_S\rangle \to \left|K^0_+\right\rangle$ and $|K_L\rangle \to \left|K^0_-\right\rangle$. The K_S would decay to a CP–even final state such as $\pi\pi$ and K_L would decay to CP–odd final state such as $\pi\pi\pi$. At m_K, the two-pion phase space is much larger than the three-pion phase space, so the K_S has a much shorter lifetime than K_L.

The eigenvalues of H are given by $\lambda_\pm = M_{11} - i\Gamma_{11}/2 \pm pq$, with

$$\frac{p}{q} = \frac{\sqrt{M_{12} - i\Gamma_{12}/2}}{\sqrt{M^*_{12} - i\Gamma^*_{12}/2}}. \tag{2.14}$$

The difference in eigenvalues is

$$\begin{aligned} 2pq &= (m_L - m_S) - i/2(\Gamma_L - \Gamma_S) \\ &= 2\left(M_{12} - \frac{i}{2}\Gamma_{12}\right)^{1/2}\left(M^*_{12} - \frac{i}{2}\Gamma^*_{12}\right)^{1/2}. \end{aligned} \tag{2.15}$$

In the limit where CP violation is small, the approximation $2pq \simeq 2\mathrm{Re}M_{12} - i\mathrm{Re}\Gamma_{12}$ is valid, resulting in the following relations:

$$m_L - m_S \simeq 2\mathrm{Re}M_{12} \tag{2.16a}$$

$$\Gamma_L - \Gamma_S \simeq 2\mathrm{Re}\Gamma_{12}. \tag{2.16b}$$

Using these relations along with the property that M and Γ are hermitian, $\bar{\epsilon}$ can be expressed as follows:

$$\frac{p}{q} = \frac{1+\bar{\epsilon}}{1-\bar{\epsilon}}, \tag{2.17a}$$

$$\bar{\epsilon} = \frac{p-q}{p+q} = \frac{i}{2}\frac{\mathrm{Im}M_{12} - \frac{i}{2}\mathrm{Im}\Gamma_{12}}{\mathrm{Re}M_{12} - \frac{i}{2}\mathrm{Re}\Gamma_{12}} \simeq \frac{1}{2}\frac{M_{12} - M_{21} - \frac{i}{2}(\Gamma_{12} - \Gamma_{21})}{m_L - m_S - \frac{i}{2}(\Gamma_L - \Gamma_S)}. \tag{2.17b}$$

The $K_L - K_S$ mass difference and decay widths are measured experimentally and found to be $m_L - m_S = (3.483 \pm 0.006) \times 10^{-12}$ MeV and $\Gamma_{K_S} - \Gamma_{K_S} = (7.339 \pm 0.004) \times 10^{-12}$ MeV, which leads to the numerical result $\Delta M/\Delta\Gamma = 0.4749 \pm 0.0009 \approx 1/2$. Making this approximation in Eq. (2.17b), an alternative expression for $\bar{\epsilon}$ is obtained:

$$\bar{\epsilon} \simeq \frac{e^{i\pi/4}}{\sqrt{2}}\left(\frac{\mathrm{ImM}_{12}}{\Delta m} - i\frac{\mathrm{ImA}_0}{\mathrm{ReA}_0}\right). \tag{2.18}$$

2.3 CP Violation in Neutral Kaon Systems

There are three types of CP violation in neutral meson decays: CP violation during the decay (type 1), CP violation in mixing (type 2) and CP violation in the interference between mixing and decay (type 3). In the previous section the mixture of CP eigenstates generated by the $K - \bar{K}$ mixing was described, which provides one souce of CP violation in K_L decays. However, the possibility of direct CP violation, where a CP-odd kaon eigenstate decays directly to $\pi\pi$ is also present. If such direct CP violation occurs, the $K \to \pi\pi$ isospin amplitudes defined in Eq. (2.5), are complex valued: $A_I = |A_I|e^{i\xi_I}$. The phases ξ_I characterise the CP violation in the decay.

It is standard to define the following measures of CP violation:

$$\frac{\langle\pi^+\pi^-|H_W|K_L\rangle}{\langle\pi^+\pi^-|H_W|K_S\rangle} \equiv \eta_{+-} \equiv \epsilon + \epsilon', \qquad \frac{\langle\pi^0\pi^0|H_W|K_L\rangle}{\langle\pi^0\pi^0|H_W|K_S\rangle} \equiv \eta_{00} \equiv \epsilon - 2\epsilon' \tag{2.19}$$

where $\epsilon = \bar{\epsilon} + i\mathrm{ImA}_0/\mathrm{ReA}_0$ parametrises indirect CP violation while

$$\epsilon' = \frac{\mathrm{Re}A_2 e^{i(\delta_2 - \delta_0)}}{\sqrt{2}\mathrm{Re}A_0}\left(\frac{\mathrm{Im}A_2}{\mathrm{Re}A_2} - \frac{\mathrm{Im}A_0}{\mathrm{Re}A_0}\right) \tag{2.20}$$

parametrises direct CP violation. In particular Re(ϵ) measures CP violation in mixing, Re(ϵ') measures CP violation in decay, and Im(ϵ) and Im(ϵ') measure type3 CP violation.

It is conventional to use Eq. (2.18) to write a formula for ϵ as follows:

$$\begin{aligned}\epsilon = \bar{\epsilon} + i\frac{\mathrm{ImA_0}}{\mathrm{ReA_0}} &\simeq \frac{e^{i\pi/4}}{\sqrt{2}}\left(\frac{\mathrm{ImM_{12}}}{\Delta m} - i\frac{\mathrm{ImA_0}}{\mathrm{ReA_0}}\right) + i\frac{\mathrm{ImA_0}}{\mathrm{ReA_0}} \\ &= \frac{e^{i\pi/4}}{\sqrt{2}}\left(\frac{\mathrm{ImM_{12}}}{2\mathrm{ReM_{12}}} + i\frac{\mathrm{ImA_0}}{\mathrm{ReA_0}}\right),\end{aligned} \tag{2.21}$$

where the phase convention is the same as in Ref. [1].

This leads to the well known formula for Re(ϵ'/ϵ):

$$\mathrm{Re}\left(\frac{\epsilon'}{\epsilon}\right) = \frac{\omega}{\sqrt{2}|\epsilon|}\left(\frac{\mathrm{ImA_2}}{\mathrm{ReA_2}} - \frac{\mathrm{ImA_0}}{\mathrm{ReA_0}}\right), \tag{2.22}$$

where $\omega \equiv \mathrm{Re(A_2)/Re(A_0)}$. Experimental values for the CP violating parameters can be found in [3]:

$$\mathrm{Re}\left(\frac{\epsilon'}{\epsilon}\right) = (1.65 \pm 0.26) \times 10^{-3} \text{ and } |\epsilon| = (2.228 \pm 0.011) \times 10^{-3}.$$

2.4 The CKM Matrix

Electroweak interactions are included within the Standard Model in the form of a local $SU(2)_L \otimes U(1)_Y$ gauge symmetry which is spontaneously broken by the Higgs mechanism to a $U(1)_Q$ symmetry, where Y and Q refer to the hypercharge and electric charge generators respectively.

The left-handed quarks and leptons transform as $SU(2)_L$ doublets

$$\begin{pmatrix} \nu_e \\ e^- \end{pmatrix}_L \quad \begin{pmatrix} \nu_\mu \\ \mu^- \end{pmatrix}_L \quad \begin{pmatrix} \nu_\tau \\ \tau^- \end{pmatrix}_L \tag{2.23}$$

$$\begin{pmatrix} u \\ d' \end{pmatrix}_L \quad \begin{pmatrix} c \\ s' \end{pmatrix}_L \quad \begin{pmatrix} t \\ b' \end{pmatrix}_L \tag{2.24}$$

while the right-handed fields, $e_R, \mu_R, \tau_R, u_R, d'_R$, transform as $SU(2)_L$ singlets. The primes on the down-type quarks indicate that the weak eigenstates (d', s', b') are not the same as the mass eigenstates (d, s, b). The two are related by the unitary Cabibo-Kobayashi-Maskawa (CKM) matrix [30]:

$$\begin{pmatrix} d' \\ s' \\ b' \end{pmatrix} = \begin{pmatrix} V_{ud} & V_{us} & V_{ub} \\ V_{cd} & V_{cs} & V_{cb} \\ V_{td} & V_{ts} & V_{tb} \end{pmatrix} \begin{pmatrix} d \\ s \\ b \end{pmatrix}. \tag{2.25}$$

The CKM matrix is parametrised by three Euler angles and one phase. The standard parametrisation of the CKM matrix is

$$V_{CKM} = \begin{pmatrix} c_{12}c_{13} & s_{12}c_{13} & s_{13}e^{i\delta} \\ -s_{12}c_{23} - c_{12}s_{23}s_{13}e^{i\delta} & c_{12}c_{23} - s_{12}s_{23}s_{13}^{i\delta} & s_{23}c_{13} \\ s_{12}s_{23} - c_{12}c_{23}s_{13}^{i\delta} & -c_{12}s_{23} - s_{12}c_{23}s_{13}e^{i\delta} & c_{23}c_{13} \end{pmatrix} \tag{2.26}$$

If $\delta \neq 0$ or π then the CKM matrix is complex, which leads to CP violation in the Standard Model.

Chapter 3

Weak Hamiltonian and Operator Basis

3.1 Operator Product Expansion

The energy binding the quarks in hadrons is typically $\mathcal{O}(\Lambda_{\rm QCD})$, where the scale $\Lambda_{\rm QCD} \approx 200$ MeV. This is much lower than the scale of the weak interactions, which take place at energies of $\mathcal{O}(M_W)$. Perturbation theory is not valid at energies $\mathcal{O}(\Lambda_{\rm QCD})$, so to make progress when calculating hadronic decays it is helpful to construct a low energy effective theory describing the weak decay of the quarks. The operator product expansion provides the appropriate theoretical framework for this.

The operator product expansion allows the product of two charged currents to be expanded into a series of local effective operators, whose contributions are weighted by Wilson coefficients. In this effective theory the W-boson is integrated out, and the effects of the short-range force mediated by the W-boson are approximated by a point interaction. Similarly, loop effects due to the Z-boson and heavy quarks can also be integrated out, until a theory containing f light quarks remains. The high energy effects of the W boson, Z boson, and heavy quarks are included in the Wilson coefficients, while the low energy non-perturbative physics is encoded in matrix elements of the effective operators.

In the calculation of $K \to \pi\pi$ matrix elements a 3-flavour effective theory is adopted, where only the u, d, and s quarks are included in the local operators. The perturbative calculation of the Wilson coefficients is described in section 3.3.

3.2 Operator Basis

The $\Delta S = 1$ effective Hamiltonian can be written in a 3-flavour effective theory as follows

$$H_{\text{eff}} = \frac{G_F}{\sqrt{2}} V_{us}^* V_{ud} \sum_{i=1}^{10} C_i(\mu) Q_i(\mu), \tag{3.1}$$

and the $K \to \pi\pi$ decay amplitudes are evaluated in terms of matrix elements of this effective Hamiltonian. The energy scale μ provides the separation of scales between the low energy physics encoded in the operators $Q_i(\mu)$ and the perturbative corrections encoded in the Wilson coefficients $C_i(\mu)$. The operators and Wilson coefficients must be renormalised at the same scale (μ) and in the same scheme, so that the resulting Hamiltonian is independent of μ. The conventional choice for the evaluation of the Wilson coefficients is the $\overline{\text{MS}}$-NDR scheme. There are ten operators in the $\Delta S = 1$ Hamiltonian. These are enumerated below, where

$$(\bar{q}_i q_j)_{V\pm A} (\bar{q}_j q_i)_{V\pm A} \equiv (\bar{q}_i \gamma^\mu (1 \pm \gamma^5) q_j)_{\alpha\beta} (\bar{q}_j \gamma^\mu (1 \pm \gamma^5) q_i)_{\gamma\delta},$$

α, β, γ and δ label the spinor indices and i and j label the colour indices. The sum over repeated μ indices is implicit.

$$\begin{aligned}
Q_1 &= (\bar{s}_i u_j)_{V-A} (\bar{u}_j d_i)_{V-A} & Q_3 &= (\bar{s}_i d_i)_{V-A} \sum_{q=u,d,s} (\bar{q}_j q_j)_{V-A} & Q_7 &= \frac{3}{2} (\bar{s}_i d_i)_{V-A} \sum_{q=u,d,s} e_q (\bar{q}_j q_j)_{V+A} \\
Q_2 &= (\bar{s}_i u_i)_{V-A} (\bar{u}_j d_j)_{V-A} & Q_4 &= (\bar{s}_i d_j)_{V-A} \sum_{q=u,d,s} (\bar{q}_j q_i)_{V-A} & Q_8 &= \frac{3}{2} (\bar{s}_i d_j)_{V-A} \sum_{q=u,d,s} e_q (\bar{q}_j q_i)_{V+A} \\
& & Q_5 &= (\bar{s}_i d_i)_{V-A} \sum_{q=u,d,s} (\bar{q}_j q_j)_{V+A} & Q_9 &= \frac{3}{2} (\bar{s}_i d_i)_{V-A} \sum_{q=u,d,s} e_q (\bar{q}_j q_j)_{V-A} \\
& & Q_6 &= (\bar{s}_i d_j)_{V-A} \sum_{q=u,d,s} (\bar{q}_j q_i)_{V+A} & Q_{10} &= \frac{3}{2} (\bar{s}_i d_j)_{V-A} \sum_{q=u,d,s} e_q (\bar{q}_j q_i)_{V-A}
\end{aligned} \tag{3.2}$$

The operators Q_2, Q_3, Q_5, Q_7 and Q_9 are colour diagonal, while the remaining operators are referred to as colour mixed. Operators Q_1 and Q_2 are current-current

operators arising from the interactions depicted in Fig. 3.1, $Q_3, \ldots, Q_6$ arise from QCD-penguin diagrams illustrated in Fig. 3.2(a) and $Q_7, \ldots, Q_{10}$ arise from electroweak penguin diagrams illustrated in Fig. 3.2(b).

All ten operators contribute to the $\Delta I = 1/2$ $K \to \pi\pi$ amplitude. A simplification can be made in the case of the $\Delta I = 3/2$ calculation, where the $\Delta I = 3/2$ effective Hamiltonian can be written in terms of just three operators. These operators are classified by their transformation properties under $SU(3)_{\rm L} \times SU(3)_{\rm R}$ symmetry:

$$\begin{aligned} Q^{3/2}_{(27,1)} &= (\bar{s}_i d_i)_{V-A}(\bar{u}_j u_j - \bar{d}_j d_j)_{V-A} + (\bar{s}_i u_i)_{V-A}(\bar{u}_j d_j)_{V-A} \\ Q^{3/2}_{(8,8)} &= (\bar{s}_i d_i)_{V-A}(\bar{u}_j u_j - \bar{d}_j d_j)_{V+A} + (\bar{s}_i u_i)_{V-A}(\bar{u}_j d_j)_{V+A} \\ Q^{3/2}_{(8,8)\rm mx} &= (\bar{s}_i d_j)_{V-A}(\bar{u}_j u_i - \bar{d}_j d_i)_{V+A} + (\bar{s}_i u_j)_{V-A}(\bar{u}_j d_i)_{V+A}. \end{aligned} \tag{3.3}$$

The effective Hamiltonian for the $\Delta I = 3/2$ transition is

$$\begin{aligned} H^{I=3/2}_{\rm eff} =& \frac{G_F}{\sqrt{2}} V^*_{us} V_{ud} \sum_{i=1}^{10} C_i(\mu) Q_i(\mu) \Big|_{3/2} \\ =& \frac{G_F}{\sqrt{2}} V^*_{us} V_{ud} \left[C^{3/2}_{(27,1)} Q^{3/2}_{(27,1)} + C^{3/2}_{(8,8)} Q^{3/2}_{(8,8)} + C^{3/2}_{(8,8)\rm mx} Q^{3/2}_{(8,8)\rm mx} \right]. \end{aligned} \tag{3.4}$$

The Wilson coefficients for the three $\Delta I = 3/2$ operators are related to the Wilson coefficients in the full 10-operator basis as follows:

$$C^{3/2}_{(27,1)} = \frac{(C_1 + C_2)}{3} + \frac{(C_9 + C_{10})}{2} \tag{3.5}$$

$$C^{3/2}_{(8,8)} = \frac{C_7}{2} \tag{3.6}$$

$$C^{3/2}_{(8,8)\rm mx} = \frac{C_8}{2}. \tag{3.7}$$

This is clear if one considers the full decomposition of the operators $Q_1, \ldots, Q_{10}$ in terms of operators with definite isospin and chirality, which can be found in Appendix B of [20].

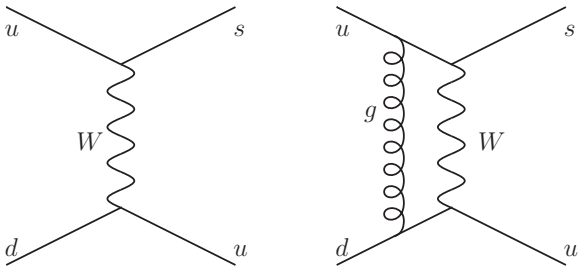

Figure 3.1: *Current-Current interaction generating Q1 and Q2.*

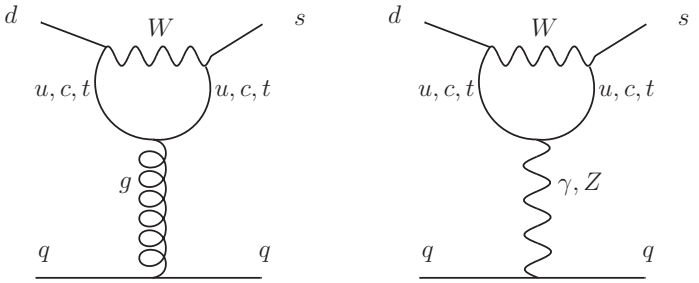

(a) QCD penguin (b) Electroweak penguin

Figure 3.2: *Penguin diagrams*

3.2.1 The Chiral Basis

The ten operators enumerated in section 3.2 are not linearly independent. Three of the operators can be eliminated with the following relations:

$$\begin{aligned} Q_4 &= Q_2 + Q_3 - Q_1 \\ Q_9 &= \frac{3}{2}Q_1 - \frac{1}{2}Q_3 \\ Q_{10} &= \frac{1}{2}(Q_1 - Q_3) + Q_2. \end{aligned} \tag{3.8}$$

The remaining seven operators can be recombined according to their transformation properties under the chiral flavour-symmetry group $SU(3)_L \times SU(3)_R$. This new

basis of seven operators is known as the chiral basis:

$$\begin{aligned} Q'_1 &= 3Q_1 + 2Q_2 - Q_3 \\ Q'_2 &= \frac{1}{5}(2Q_1 - 2Q_2 + Q_3) \\ Q'_3 &= \frac{1}{5}(-3Q_1 + 3Q_2 + Q_3) \\ Q'_{5,6} &= Q_{5,6} \\ Q'_{7,8} &= Q_{7,8}. \end{aligned} \tag{3.9}$$

In this basis there is a single $(27,1)$ operator Q'_1. The operators Q'_7 and Q'_8 transform according to the $(8,8)$ irreducible representation and the remaining operators transform according to the $(8,1)$ irreducible representation of $SU(3)_L \times SU(3)_R$.

3.2.2 Operators for $K \to \pi^+\pi^+$

The operators of Eq. (3.3) all have $I_z = 1/2$ and would be suitable to describe the physical decay of $K^+ \to \pi^+\pi^0$ for example. However, when A_2 is to be evaluated at close to physical kinematics, it is the $K^+ \to \pi^+\pi^+$ matrix element that is computed. The advantages of computing the $K^+ \to \pi^+\pi^+$ matrix element are explained in detail in Chapter 7.1, and are related to the mechanism used for giving the final-state pions momentum. Using the Wigner-Eckart theorem, the $\langle \pi^+\pi^+ | \, Q^{I=3/2}_{I_z=3/2} \, | K^+ \rangle$ matrix element is related to the $\langle \pi^+\pi^0 | \, Q^{I=3/2}_{I_z=1/2} \, | K^+ \rangle$ matrix element via a Clebsch-Gordan coefficient:

$$\langle \pi^+\pi^0 | \, Q^{I=3/2}_{I_z=1/2} \, | K^+ \rangle = \frac{\sqrt{3}}{2\sqrt{2}} \langle \pi^+\pi^+ | \, Q^{I=3/2}_{I_z=3/2} \, | K^+ \rangle \tag{3.10}$$

where we have used $\langle \pi^+\pi^0 | \, Q^{I=3/2}_{I_z=1/2} \, | K^+ \rangle = \frac{1}{\sqrt{2}} \langle (\pi\pi)^{I=2}_{I_z=1} | \, Q^{I=3/2}_{I_z=1/2} \, | K^+ \rangle$, and the $\langle \pi^+\pi^0 |$ state is not symmetrised.

By applying the isospin raising operator to the operators of Eq. (3.3) an expression for $\Delta I = 3/2$, $\Delta I_z = 3/2$ operators can be found:

$$Q^{I=3/2}_{I_z=3/2} = -\sqrt{3}(\bar{s}\Gamma_{\mu,a}d)(\bar{u}\Gamma_{\mu,b}d), \tag{3.11}$$

where $\Gamma_{\mu,x} = \gamma_\mu(1 \mp \gamma_5)$. The convention is that u annihilates an up-quark and $\overline{u}$ creates an up-quark. Similarly d annihilates a down quark and $\overline{d}$ creates a down-quark. The raising operator transforms u to $-d$ and $\overline{d}$ to $\overline{u}$.

The operators used in the lattice simulation are

$$\begin{gathered} Q'^{3/2}_{(27,1)} = (\bar{s}_i d_i)_{\text{V-A}}(\bar{u}_j d_j)_{\text{V-A}}, \qquad Q'^{3/2}_{(8,8)} = (\bar{s}_i d_i)_{\text{V-A}}(\bar{u}_j d_j)_{\text{V+A}}, \\ Q'^{3/2}_{(8,8)} = (\bar{s}_i d_j)_{\text{V-A}}(\bar{u}_j d_i)_{\text{V+A}}. \end{gathered} \tag{3.12}$$

Specifically, $\langle \pi^+\pi^+| \, Q^{I=3/2}_{I_z=3/2} \, |K^+\rangle = -\sqrt{3} \, \langle \pi^+\pi^+| \, Q'^{I=3/2}_j \, |K^+\rangle$ where $Q'^{I=3/2}_j$ is one of the operators defined in Eq. (3.12).

3.3 Wilson Coefficients

Expressions for the $\Delta S = 1$ Wilson Coefficients evaluated at M_W are given in Eqns. (7.3) - (7.12) of [4]. The running of the Wilson coefficients from M_W down to scales below m_c is described in [4] and summarised here.

At scales of $\mathcal{O}(M_W)$ the Wilson coefficients may be calculated using ordinary perturbation theory. While α_s is a valid expansion parameter down to scales $\mathcal{O}(1 \text{ GeV})$, the presence of large logarithms $\alpha_s \log M_W^2/\mu^2$ when $\mu \ll M_W$ render the perturbative expansion invalid at such low energies. These large logarithms can be resummed using renormalisation group techniques. In the leading logarithm approximation (LLA), all terms of $\mathcal{O}\left[\alpha_s(\mu) \ln (M_W/\mu)\right]^n$ are resummed. This leads to renormalisation group improved perturbation theory. The final result of this section will be the evaluation of the Wilson Coefficient functions $C_i(\mu)$ at energies $\mathcal{O}(1 \text{ GeV})$ at next-to-leading order in renormalisation group improved perturbation theory.

3.3.1 Renormalisation group evolution matrix

The renormalisation group equation for the Wilson Coefficient functions is

$$\frac{d}{d\ln\mu}\vec{C}(\mu) = \gamma_s^T(g)\vec{C}(\mu), \tag{3.13}$$

where $\gamma_s(g)$ is the QCD anomalous dimension matrix

$$\gamma_s(\alpha_s) = \gamma_s^{(0)}\frac{\alpha_s(\mu)}{4\pi} + \gamma_s^{(1)}\left(\frac{\alpha_s(\mu)}{4\pi}\right)^2 \tag{3.14}$$

and $\alpha_s(\mu) = \dfrac{g^2(\mu)}{4\pi}$.

Equation(3.13) has solution

$$\vec{C}(\mu) = U(\mu, M_W)\vec{C}(M_W) \tag{3.15}$$

where the evolution matrix U is given by

$$U(m_1, m_2) \equiv T_g \exp\int_{g(m_2)}^{g(m_1)} dg' \frac{\gamma^T(g'^2)}{\beta(g')}. \tag{3.16}$$

The beta-function $\beta(g)$ is given at next-to-leading order in perturbation theory by

$$\beta(g) = -\beta_0\frac{g^3}{16\pi^2} - \beta_1\frac{g^5}{(16\pi^2)^2}, \tag{3.17}$$

where $\beta_0 = (11N - 2f)/3$ and $\beta_1 = (34N^2/3 - 10Nf/2 - 2C_F f)$. Here N is the number of colours, f is the number of active quark flavours and $C_F = (N^2-1)/2N$. The g-ordering operator T_g orders functions of the coupling g such that the coupling constants increase from right to left.

At next-to-leading order, the first two terms of Eq. (3.14) and Eq. (3.17) and are kept and the evolution matrix can be written in terms of $U^{(0)}$, the evolution matrix in the LLA, along with a next-to-leading order correction J:

$$U(\mu, m) = (1 + \frac{\alpha_s(\mu)}{4\pi}J)U^{(0)}(\mu, m)(1 - \frac{\alpha_s(m)}{4\pi}J). \tag{3.18}$$

Working in a basis where $\gamma^{(0)}$ is diagonal, the expression for $U^{(0)}(\mu, m)$ is

$$U^{(0)}(\mu, m) = V \left(\left[\frac{\alpha_s(m)}{\alpha_s(\mu)} \right]^{\vec{\gamma}^{(0)}/2\beta_0} \right)_D V^{-1}, \tag{3.19}$$

where V diagonalises $\gamma_s^{(0)T}$:

$$\gamma_D^{(0)} = V^{-1} \gamma_s^{(0)T} V. \tag{3.20}$$

A detailed description of how to calculate the matrix J is given in [4]. Equation (3.18) is valid in the absence of electromagnetic interactions. However, since operators $Q_7, \ldots, Q_{10}$ originate from electromagnetic-penguin interactions it is necessary to modify Eq. (3.18) to include electromagnetic effects.

The perturbative expansion of the anomalous dimension matrix including QCD and QED effects is given by Eq. (3.14) plus an additional term proportional to the electromagnetic coupling α:

$$\gamma(g^2, \alpha) = \gamma_s(g^2) + \frac{\alpha}{4\pi} \Gamma(g^2), \tag{3.21}$$

where $\Gamma(g^2)$ has the expansion

$$\Gamma(g^2) = \gamma_e^{(0)} + \frac{\alpha_s}{4\pi} \gamma_{se}^{(1)} + \cdots . \tag{3.22}$$

The anomalous dimension matrices are calculated in [4], where expressions for $\gamma_s^{(0)}$, $\gamma_s^{(1)}$, $\gamma_e^{(0)}$ and $\gamma_{se}^{(1)}$ in the $\overline{\text{MS}}$-NDR scheme can be found in Eq (6.25) + Tab. XIV, Eq (6.26) + Tab. XV, Tab. XVI, and Tab. XVII respectively.

In analogy with Eq. (3.18), where the NLO corrections were included in the matrix J, the evolution matrix now gains an additional term proportional to α:

$$U(m_1, m_2, \alpha) = U(m_1, m_2) + \frac{\alpha}{4\pi} R(m_1, m_2). \tag{3.23}$$

The matrix R in Eq. (3.23) is analogous to the matrix J in Eq. (3.18). Full expressions for R are given in Eqns. (7.23) - (7.28) of [4]. A notable feature is that R contains a contribution of $\mathcal{O}(1)$ along with a contribution $\mathcal{O}(1/\alpha_s)$. Thus, in the

power counting adopted in [4], the evolution matrix as written in Eq.(3.23) contains terms of $\mathcal{O}(1)$, $\mathcal{O}(\alpha_s)$, $\mathcal{O}(\alpha)$ and $\mathcal{O}(\alpha/\alpha_s)$.

3.3.2 Matching Matrix

The Wilson coefficients of the ten operators in Eq. (3.2) are first evaluated at a scale $\mathcal{O}(M_W)$ in a five-flavour effective theory. The evolution matrix in Eq. (3.23) can then be used to calculate the Wilson coefficients at scales down to $\mu \approx m_b$, the mass of the bottom-quark. In order to evaluate the Wilson coefficients at scales lower than m_b, we can formulate a new effective theory for $\mu < m_b$ where the b-quark is removed as an explicit degree of freedom. The Wilson coefficients in the four-flavour theory are related to those in the five-flavour theory by a *matching matrix* M.

To establish the notation, let the matrix elements of the ten operators in Eq. (3.2), written in vector form $\vec{Q}$ and renormalised at the scale m, be related to the tree level matrix elements $\left\langle \vec{Q}^{(0)} \right\rangle$, by

$$\left\langle \vec{Q}_f(m) \right\rangle = \left(1 + \frac{\alpha_s^{(f)}(m)}{4\pi} r_s^{(f)} + \frac{\alpha}{4\pi} r_e^{(f)} \right) \left\langle \vec{Q}_f^{(0)} \right\rangle, \tag{3.24}$$

where $r_s^{(f)}$ and $r_e^{(f)}$ are matrices characterising the QCD and EM radiative corrections.

In the general case of matching from an f-flavour theory to an $(f-1)$-flavour theory, the matching matrix M is calculated by imposing the condition

$$\left\langle \vec{Q}_f(m) \right\rangle^T \vec{C}_f(m) = \left\langle \vec{Q}_{f-1}(m) \right\rangle^T \vec{C}_{f-1}(m), \tag{3.25}$$

where $m = m_b, m_c$ is a flavour threshold. Using Eq. (3.24), it is then apparent that

$$\left\langle \vec{Q}_f(m) \right\rangle = \left(1 + \frac{\alpha_s(m)}{4\pi} \delta r_s + \frac{\alpha}{4\pi} \delta r_e \right) \left\langle \vec{Q}_{f-1}(m) \right\rangle \tag{3.26}$$

where the matrices $\delta r = r^{(f)} - r^{(f-1)}$ are given in Eqns. (7.31)-(7.34) of [4]. Thus the Wilson coefficients in an f-flavour theory at scale m are related to those in an

$(f-1)$-flavour theory (also at scale m) by

$$\vec{C}_{f-1}(m) = M(m)\vec{C}_f(m) \tag{3.27}$$

where

$$M(m) = 1 + \frac{\alpha_s(m)}{4\pi}\delta r_s^T + \frac{\alpha}{4\pi}\delta r_e^T. \tag{3.28}$$

One result of a non-trivial matching matrix is the presence of discontinuities in the Wilson coefficients.

3.3.3 Wilson Coefficients in a 3-flavour theory

At scales below m_c the $\Delta S = 1$ effective Hamiltonian in Eq. (3.1) can be rewritten:

$$\mathcal{H}_{\text{eff}}(\Delta S = 1) = \frac{G_F}{\sqrt{2}} V_{\text{us}}^* V_{\text{ud}} \sum_{i=1}^{10} (z_i(\mu) + \tau y_i(\mu)) Q_i(\mu), \tag{3.29}$$

with

$$\tau = -\frac{V_{\text{ts}}^* V_{\text{td}}}{V_{\text{us}}^* V_{\text{ud}}}.$$

Numerical values for the Fermi constant G_F and the CKM matrix elements are $G_F = 1$, $V_{us} = 0.2253$, $V_{ud} = 0.97429$ and $\tau = 0.0014606 - 0.00060408i$. This factorisation of the Wilson coefficients arises because there is no GIM mechanism in the 3-flavour theory. The Wilson coefficients $y_i(\mu)$ and $z_i(\mu)$ and related by the elements of the vector $\vec{v}(\mu)$ by

$$y_i(\mu) = v_i(\mu) - z_i(\mu) \tag{3.30}$$

where

$$\vec{v}(\mu) = U_3(\mu, m_c) M(m_c) U_4(m_c, m_b) M(m_b) U_5(m_b, M_W) \vec{C}(M_W) \tag{3.31}$$

and

$$\vec{z}(\mu) = U_3(\mu, m_c)\vec{z}(m_c). \tag{3.32}$$

The subscript $f = 3, 4, 5$ on the evolution matrices indicates the number of flavours active in the effective theory. The Wilson coefficients are evaluated in the NDR scheme at NLO in perturbation theory using Eqns. (3.30), (3.31) and (3.32). The convention of [4] is to keep only the terms that are $\mathcal{O}(1)$, $\mathcal{O}(\alpha_s)$, $\mathcal{O}(\alpha)$, and $\mathcal{O}(\alpha/\alpha_s)$ in the matrix multiplication of Eq. (3.31). The power counting is such that terms $\mathcal{O}(\alpha_s) \times \mathcal{O}(\alpha/\alpha_s)$ are counted as $\mathcal{O}(\alpha)$.

Using this counting, the results of tables XVIII - XX of [4] in the NDR scheme have been reproduced. Tables 3.1 and 3.2 give the Wilson coefficients $y^{\overline{\rm MS}}$ and $z^{\overline{\rm MS}}$ at 2.15 GeV and 3 GeV in a 3-flavour theory using PDG(2010) values (in the case of 2.15 GeV) and PDG(2011) values (in the case of 3 GeV) wherever standard model parameters are required as input.

The coupling constant α_s is calculated by solving the equation

$$\frac{d\alpha_s}{d\ln\mu} = \beta(g), \tag{3.33}$$

where $\beta(g)$ was given at next-to-leading order in Eq. (3.17). The beta function depends on the number of active quark flavours, and so the coupling constant must be matched across flavour thresholds. The calculation of the strong coupling constant is based on the initial condition $\alpha_s^{(5)}(M_Z) = 0.1184$ for $M_Z = 91.1876$ MeV. The evaluation of the Wilson coefficients at 2.15 GeV used the two-loop formula for α_s given in Eq. (3.19) of [4], with the result $\alpha_s^{(3)}(2.15\,\text{GeV}) = 0.286758$. However, the evaluation of the Wilson coefficients at 3 GeV which are used in Chapter 8 were evaluated using a four-loop formula for α_s, given in Appendix A of [31], with the result is $\alpha_s^{(3)}(3\,\text{GeV}) = 0.24544$.

Wilson Coefficients in the chiral basis

The weak Hamiltonian is independent of the choice of operator basis, so it must be the case that

$$\sum_{i=1}^{7} C_i'^{\overline{\rm MS}}(\mu) Q_i'^{\overline{\rm MS}}(\mu) = \sum_{i=1}^{10} C_i^{\overline{\rm MS}}(\mu) Q_i^{\overline{\rm MS}}(\mu), \tag{3.34}$$

Table 3.1: *Wilson Coefficients in the $\overline{MS}$ scheme, at energy scale $\mu = 2.15\,GeV$.*

Weak Operator	$z_i^{\overline{MS}}(\mu)$	$y_i^{\overline{MS}}(\mu)$
Q_1	-0.29829	0
Q_2	1.14439	0
Q_3	-0.0024382	0.02414
Q_4	0.0099515	-0.058119
Q_5	-0.0011054	0.010248
Q_6	0.006574	-0.069970
Q_7	0.000070158	-0.00021118
Q_8	-0.0000901047	0.000776652
Q_9	0.0000150176	-0.0106552
Q_{10}	0.000065648	0.00297397

Table 3.2: *Wilson Coefficients in the $\overline{MS}$ scheme, at energy scale $\mu = 3\,GeV$.*

weak operator	$z_i^{\overline{\rm MS}}$	$y_i^{\overline{\rm MS}}$
Q_1	-0.241415	0
Q_2	1.11228	0
Q_3	-0.00392423	0.0211096
Q_4	0.0169695	-0.0558734
Q_5	-0.00349963	0.0117843
Q_6	0.0120747	-0.0610235
Q_7	0.0000940198	-0.000161911
Q_8	-0.000104478	0.000652032
Q_9	0.0000275290	-0.0103828
Q_{10}	0.0000798557	0.00243775
$Q^{3/2}_{(27,1)}$	0.290342	-0.00397252
$Q^{3/2}_{(8,8)}$	4.70099 $\times 10^{-5}$	-8.09555$\times 10^{-5}$
$Q^{3/2}_{(8,8)_{\rm mix}}$	-5.22390$\times 10^{-5}$	3.26016 $\times 10^{-4}$

where the prime (') referes to the operator basis defined in Eq. (3.9). The relation between the Wilson coefficients in the chiral basis and the physical basis is found in [32]:

$$C_j^{\prime\overline{\rm MS}}(\mu) = C_i^{\overline{\rm MS}}(\mu)(T_{ij} + \Delta T_{ij}) \tag{3.35}$$

with

$$T = \begin{pmatrix} 1/5 & 1 & 0 & 0 & 0 & 0 & 0 \\ 1/5 & 0 & 1 & 0 & 0 & 0 & 0 \\ 0 & 3 & 2 & 0 & 0 & 0 & 0 \\ 0 & 2 & 3 & 0 & 0 & 0 & 0 \\ 0 & 0 & 0 & 1 & 0 & 0 & 0 \\ 0 & 0 & 0 & 0 & 1 & 0 & 0 \\ 0 & 0 & 0 & 0 & 0 & 1 & 0 \\ 3/10 & 0 & -1 & 0 & 0 & 0 & 0 \\ 3/10 & -1 & 0 & 0 & 0 & 0 & 0 \end{pmatrix} \tag{3.36}$$

and

$$\Delta T = \frac{\alpha_s}{4\pi} \begin{pmatrix} 0 & 0 & 0 & 0 & 0 & 0 & 0 \\ 0 & 0 & 0 & 0 & 0 & 0 & 0 \\ 0 & 0 & 0 & 0 & 0 & 0 & 0 \\ 0 & \frac{3}{N_c} - 2 & \frac{2}{N_c} - 3 & \frac{1}{N_c} & -1 & 0 & 0 \\ 0 & 0 & 0 & 0 & 0 & 0 & 0 \\ 0 & 0 & 0 & 0 & 0 & 0 & 0 \\ 0 & 0 & 0 & 0 & 0 & 0 & 0 \\ 0 & 0 & 0 & 0 & 0 & 0 & 0 \\ 0 & 0 & 0 & 0 & 0 & 0 & 0 \\ 0 & 0 & 0 & 0 & 0 & 0 & 0 \end{pmatrix} \tag{3.37}$$

3.3.4 Wilson Coefficients at leading order

In Sec. 3.7 of Chapter 8, an attempt is made to estimate the systematic error in the calculation of the decay amplitude A_2 due to the truncation in the perturbative evaluation of the Wilson coefficients. To this end the LO contribution to the Wilson coefficients is evaluated in the $\overline{MS}$ scheme at energy scale 3 GeV. The LO contribution to the Wilson coefficients is evaluated using a one-loop formula for the beta-function and anomalous dimension matrices. Furthermore, the QED corrections introduced in Eqns. (3.21) and (3.23) are neglected. The LO contribution to the Wilson coefficients are then defined according to the following

procedure:

1. A value is chosen for the Λ parameter of four-flavor QCD. An appropriate choice of Λ is obtained by first using a four-loop running formula to evaluate $\alpha_s(M_b)$. The energy scale $\Lambda^{(4)} \equiv \Lambda_{QCD}$ is then evaluated in a four-flavour theory using the leading-order formula for α_s:

$$\alpha_s^{(f)}(\mu) = \frac{4\pi}{\beta_0^{(f)} \ln(\mu^2/\Lambda^{(f)})}, \tag{3.38}$$

   with the result $\Lambda_{QCD} = 328$ MeV. With this value for Λ_{QCD}, α_s can be evaluated at all other energy scales using Eq. (3.38) and matching at flavour boundaries as usual.

2. In setting the initial conditions for the Wilson coefficients at the scale of the W mass, corrections of $O(\alpha)$ and $O(\alpha_s)$ are only included when they depend on the top-quark mass. This also applies when calculating the coefficients z_i at the scale of the charm mass (Eq.(VII.17) in [4]).

3. In the QCD running to lower energies the one-loop expressions for the anomalous dimension matrix and β-function are used. In the presence of electromagnetic interactions, the LO anomalous dimension matrix also includes the term $\frac{\alpha}{4\pi}\gamma_e^{(0)}$.

4. At leading order the Wilson coefficients are continuous when crossing quark-mass thresholds, i.e. at LO the matching matrices defined in section 3.3.2 are trivially the identity matrix.

The LO contribution to the Wilson coefficients, evaluated at energy scale 3 GeV, are given in Tab. 3.3.

Table 3.3: *Leading order contribution to the Wilson Coefficients in the $\overline{MS}$ scheme, at energy scale $\mu = 3GeV$.*

weak operator	$z_i^{\overline{\rm MS}}$	$y_i^{\overline{\rm MS}}$
Q_1	-0.391608	0
Q_2	1.19262	0
Q_3	-0.00590226	0.0245797
Q_4	0.0227256	-0.0592354
Q_5	-0.00818322	0.0180197
Q_6	0.0199481	-0.0698914
Q_7	-0.0000852011	0.000405289
Q_8	0.000020126	0.000489482
Q_9	-0.0000708857	-0.0103101
Q_{10}	-0.0000233252	0.00327317
$Q^{3/2}_{(27,1)}$	0.26696	-0.0035185
$Q^{3/2}_{(8,8)}$	4.260055 $\times 10^{-5}$	-2.026445$\times 10^{-4}$
$Q^{3/2}_{(8,8)_{\rm mix}}$	-1.0063$\times 10^{-5}$	2.44741$\times 10^{-4}$

Chapter 4

Quantum Field Theory on the Lattice

4.1 Introduction

The fundamental objective of quantum field theory is the computation of correlation functions, the vacuum expectation of a time ordered product of operators. The path integral expression for such an object is

$$\langle 0| O_1(x_1)...O_n(x_n) |0\rangle = \frac{1}{Z}\int \mathcal{D}[A,\psi,\overline{\psi}]O_1(x_1)...O_n(x_n)e^{iS_{\mathrm{QCD}}} \tag{4.1}$$

where S_{QCD} is the action for QCD, and the partition function Z is given by

$$Z = \int \mathcal{D}[A,\psi,\overline{\psi}]e^{iS_{\mathrm{QCD}}}. \tag{4.2}$$

Lattice QCD allows correlation functions to be computed by evaluating the path integral in a brute force fashion. This is achieved by first Wick-rotating to Euclidean space-time, where the coordinates are defined in terms of Minkowski-space coordinates as:

$$x^0 = -ix_E^4, \quad x^i = x_E^i \tag{4.3}$$

and the Euclidean gamma matrices are related to the Minkowski gamma matrices by

$$\gamma_i^E = i\gamma_i, \quad \gamma_4^E = \gamma_0. \tag{4.4}$$

The Euclidean-space partition function is then given by

$$Z = \int \mathcal{D}[A, \psi, \overline{\psi}] e^{-(S_G + S_F)}, \tag{4.5}$$

where S_G is the pure gauge part of the action and $S_F = \overline{\psi}\left(\not{D} + m\right)\psi \equiv \overline{\psi} K \psi$ is the fermionic action. K is a function of the fermion mass and the gauge fields, and will often be referred to as the Dirac operator. The Euclidean-space path integral is to be interpreted as a statistical mechanics partition function with weighting $e^{-S^E_{\mathrm{QCD}}}$, where S^E_{QCD} is a shorthand for the Euclidean QCD action $S^E_{\mathrm{QCD}} = (S_G + S_F)$. The superscript E will subsequently be dropped.

4.2 Lattice Actions

Lattice actions are built by replacing integrals with sums and derivatives with finite differences. There is no unique choice for the discretised action, provided that the formal QCD Lagrangian is recovered in the limit that the lattice spacing $a \to 0$. A desirable lattice action will preserve as far as possible the symmetries of the continuum theory. Gauge invariance and chiral symmetry are of particular importance.

4.2.1 Gauge Actions

Lattice implementations of gauge fields are non-trivial because a gauge symmetry is a relation between the gauge field A^μ and the derivatives of other fields. When quantum field theory is formulated on a lattice, derivatives are replaced by finite differences. The fermion fields are defined on the lattice sites, and so a gauge transformation of a fermion field at lattice site x must be compensated for by a transformation at site $x + \hat{\mu}$. To make this explicit, consider the following example.

The fermion fields transform under a gauge transformation according to $\psi(x) \to \Omega(x)\psi(x)$ and $\bar{\psi}(x) \to \bar{\psi}(x)\Omega^\dagger(x)$, so the term

$$\bar{\psi}(x)\psi(x+\hat{\mu}) \to \bar{\psi}(x)\Omega^\dagger(x)\Omega(x+\hat{\mu})\psi(x+\hat{\mu}) \tag{4.6}$$

is not gauge invariant. In order to construct a covariant derivative, the gauge fields must be implemented in a way that connects the gauge transformation at the site x with the transformation at the site $x+\hat{\mu}$. This can be achieved by introducing $SU(3)$ matrix-valued link variables, $U_\mu(x)$ with the transformation property

$$U_\mu(x) \to \Omega(x)U_\mu(x)\Omega(x+\hat{\mu})^\dagger. \tag{4.7}$$

It is now possible to construct a covariant derivative for the fermion fields:

$$\bar{\psi}\not{D}\psi = \bar{\psi}(x)\gamma^\mu \left(\frac{U_\mu(x)\psi(x+\hat{\mu}) - U_\mu^\dagger(x-\hat{\mu})\psi(x-\hat{\mu})}{2a} \right). \tag{4.8}$$

The link variables are related to the Lie algebra valued gauge fields $A_\mu(x)$ by

$$U_\mu(x) = e^{iaA_\mu(x)}, \tag{4.9}$$

and have the property $U_{-\nu}(x+\hat{\nu}) = U_\nu^\dagger(x)$. Any closed loop of link variables will form a gauge invariant object. In particular, the plaquette variable $U_{\mu\nu}$, illustrated in Fig. 4.1, is the shortest nontrivial closed loop of link variables:

$$\begin{aligned} U_{\mu\nu}(x) &= U_\mu(x)U_\nu(x+\hat{\mu})U_{-\mu}(x+\hat{\mu}+\hat{\nu})U_{-\nu}(x+\hat{\nu}) \\ &= U_\mu(x)U_\nu(x+\hat{\mu})U_\mu^\dagger(x+\hat{\nu})U_\nu^\dagger(x). \end{aligned} \tag{4.10}$$

Wilson proposed a gauge invariant action for the gauge fields defined in terms of plaquette variables.

$$S_G = \frac{2}{g^2} \sum_{x\in\Lambda} \sum_{\mu<\nu} \text{Re Tr}\left[1 - U_{\mu\nu}(x)\right]. \tag{4.11}$$

The sum in Eq. (4.11) is over all plaquettes, with each plaquette counted with only one orientation. The discretisation of space and time introduces errors proportional

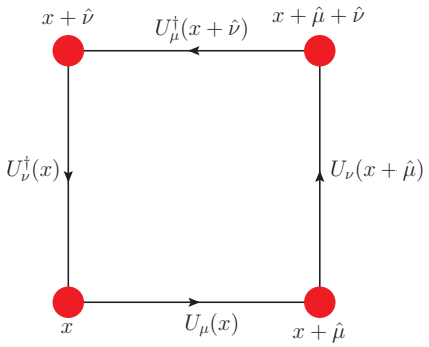

Figure 4.1: *Plaquette variable*

to some power of the lattice spacing. The tree level Wilson gauge action approximates the continuum gauge action up to $\mathcal{O}(a^2)$ corrections, which only vanish as the lattice spacing is sent to zero.

In order to reduce the size of the discretisation errors, different actions can be considered. The Iwasaki and DBW2 gauge actions are renormalisation group improved actions in truncated two-parameter space. They can be written down as

$$S_G[U] = \frac{-\beta}{3}\left((1-8c_1)\sum_{x;\mu<\nu} P[U]_{x,\mu\nu} + c_1 \sum_{x;\mu\neq\nu} R[U]_{x,\mu\nu}\right) \tag{4.12}$$

where $P[U]_{x,\mu\nu}$ is the real part of the trace of the path ordered product of links around the 1×1 plaquette in the μ,ν plane at point x, $\beta \sim 1/g_0^2$ and $R[U]$ denotes the real part of the trace of ordered product of $SU(3)$ link matrices along 1×2 rectangles in the μ,ν plane. The coefficient c_1 is chosen to be $c_1 = -0.331$ for the Iwasaki gauge action and $c_1 = -1.4069$ for the DBW2 gauge action. The Iwasaki and DBW2 actions are particularly significant because they have been shown to reduce the chiral symmetry breaking in domain wall fermion formulations for the fermion action [33].

4.3 Fermions on the Lattice

The naive discretisation of the fermion action is

$$\begin{aligned} S_F &= a^4 \sum_{x,\mu} \left[\bar{\psi}(x)\gamma^\mu \left(\frac{U_\mu(x)\psi(x+\hat{\mu}) - U_\mu^\dagger(x-\hat{\mu})\psi(x-\hat{\mu})}{2a} \right) + m\bar{\psi}(x)\psi(x) \right] \\ &\equiv a^4 \sum_{x,\mu} \bar{\psi}(x) K(x,y) \psi(y), \end{aligned} \tag{4.13}$$

where the link variables U were defined in the previous section and

$$K(x,y) = \frac{\left(\gamma^\mu U_\mu(x)\delta_{x+\hat{\mu},y} - U_\mu^\dagger(x-\hat{\mu})\delta_{x-\hat{\mu},y} \right)}{2a} + m\delta_{x,y} \tag{4.14}$$

will be referred to as the Dirac operator. The spin and colour indices in Eqns. (4.13) and (4.14) have been suppressed. The naive fermion action suffers from artefacts known as fermion doublers. Working in the unit gauge, where all $U_\mu(x) = 1$, the momentum space fermion propagator (given by the inverse of the Dirac operator) is

$$K^{-1}(p) = \frac{m - ia^{-1}\sum_\mu \gamma_\mu \sin(p_\mu a)}{m^2 + a^{-2}\sum_\mu \sin(p_\mu a)^2}. \tag{4.15}$$

In the massless limit, the fermion propagator is

$$\begin{aligned} K^{-1}(p)\Big|_{m=0} &= \frac{-ia^{-1}\sum_\mu \gamma_\mu \sin(p_\mu a)}{a^{-2}\sum_\mu \sin(p_\mu a)^2} \\ &\xrightarrow{a\to 0} \frac{-i\sum_\mu \gamma_\mu p_\mu}{p^2}. \end{aligned} \tag{4.16}$$

The last line of Eq. (4.16) has a single pole in the propagator at $p = (0,0,0,0)$. This pole corresponds to a single fermion which is described by the continuum Dirac operator. However, looking at the first line of Eq. (4.16) it is clear that on the lattice the propagator has more than one pole. The denominator $\sin(p_\mu a)^2$ is equal to zero whenever the elements of p are all equal to 0 or π/a. Thus the lattice fermion propagator describes a total of 16 fermions. These additional fermions are referred to as the doublers.

A possible solution to avoid introducing the doublers was proposed by Wilson, who added an irrelevant operator to the fermion action in the form of a second derivative, $S_F \to S_F + S_{\text{Wilson}}$, where

$$\begin{aligned} S_{\text{Wilson}} &= \frac{-a^3 r}{2} \sum_{\mu,x} \bar{\psi}(x) \Big(U_\mu(x)\psi(x+\hat{\mu}) - 2\psi(x) + U_\mu^\dagger(x-\hat{\mu})\psi(x-\hat{\mu}) \Big) \\ &\to \frac{-ar}{2} \bar{\psi}\Box\psi, \end{aligned} \tag{4.17}$$

r is known as the Wilson parameter, and the second line of Eq. (4.17) shows the behaviour of S_{Wilson} in the continuum limit.

The free Dirac operator for Wilson fermions is

$$K(x,y) = \left(m + \frac{4r}{a} - \frac{1}{2a} \sum_{\mu=1}^{4} \{ (r-\gamma_\mu)\delta_{x+\hat{\mu},y} + (r+\gamma_\mu)\delta_{x-\hat{\mu},y} \} \right), \tag{4.18}$$

and the corresponding momentum-space propagator is

$$K^{-1}(p) = \frac{m + \frac{r}{a}\sum_{\mu=1}^{4}(1-\cos(p_\mu a)) - \frac{i}{a}\sum_{\mu=1}^{4}\gamma_\mu \sin(p_\mu a)}{\Big(m + \frac{r}{a}\sum_{\mu=1}^{4}(1-\cos(p_\mu a)) \Big)^2 + \frac{1}{a^2}\sum_{\mu=1}^{4}\sin^2(p_\mu a)} \tag{4.19}$$

The extra term $\frac{r}{a}\sum_{\mu=1}^{4}(1-\cos(p_\mu a))$ is large at $p_\mu = \pi/a$ ensuring that at the edges of the Brillouine zone the doublers become very heavy and decouple from the theory. The Wilson term successfully removes the doublers from the fermion action, but this comes at the cost of explicitly breaking chiral symmetry.

The loss of chiral symmetry in a lattice formulation of fermions where the doublers have been removed from the theory appears to be an inevitable consequence of the Nielsen-Ninomiya theorem, which states that in a lattice regularisation which is hermitian, translationally invariant, and whose Dirac operator has a well defined fourier transform and continuous first derivative everywhere in the Brillouine zone, it is not possible to remove the doublers without breaking chiral symmetry. Chiral symmetry can be expressed by the fact that a massless Dirac operator K anticommutes with γ_5:

$$K\gamma_5 + \gamma_5 K = 0. \tag{4.20}$$

Ginsparg and Wilson suggested an alternative formulation of chiral symmetry on the lattice, in the form of the Ginsparg-Wilson equation:

$$K\gamma_5 + \gamma_5 K = aK\gamma_5 K. \tag{4.21}$$

Chiral symmetry is recovered in the naive continuum limit $a \to 0$ while the restrictions of the Nielsen-Ninomiya theorem can be avoided. A solution to the Ginsparg-Wilson equation is given by Neuberger's overlap operator

$$K_{\text{ov}} = \frac{1}{a}\left(1 + \gamma_5 \text{sign}[H]\right), \tag{4.22}$$

where $H = \gamma_5 A$, A is a γ_5-hermitian Dirac operator such as Wilson and $\text{sign}[H] = H(H^2)^{-1/2}$. Overlap fermions are particularly expensive to simulate.

4.3.1 Domain Wall Fermions

Domain wall fermions (DWF) provide an alternative method for eliminating fermion doublers from the theory while maintaining chiral symmetry on the lattice. The DWF discretisation of the Dirac action was proposed by Kaplan [34] and developed by Furman and Shamir [35, 36]. Kaplan showed that for free Wilson-like fermions in five dimensions, the inclusion of a mass term that can vary in the fifth dimension, and takes the shape of a step-function (domain wall), results in a single chiral fermion which is bound to the four-dimensional wall. On a finite lattice with periodic boundary conditions an anti domain wall appears with a bound chiral fermion of opposite chirality. For large fifth dimension the fermions have exponentially small ovelap and do not mix. Kaplan's fermions retain the full $SU(3)_L \times SU(3)_R$ continuum chiral symmetry on the lattice. The interacting theory is defined by coupling the fermions to a four-dimensional gauge field.

The fermionic action for a single flavour has the following form:

$$S_F(\bar{\Psi}, \Psi, U) = -\sum_{x,x',s,s'} \bar{\Psi}_{x,s} (D_{\text{DWF}})_{x,s;x',x'} \Psi_{x',s'} \tag{4.23}$$

where the Grassmann valued fields $\Psi(x,s)$ and $\bar{\Psi}(x,s)$ are functions of a space-time coordinate x and and fifth-dimensional coordinate s. The extent of the fifth dimension will be denoted L_s, and s is in the range $0 < s < L_s - 1$. The domain wall Dirac operator, $(D_{DWF})_{x,s;x',s'}(M_5, m_f)$ contains two terms,

$$(D_{\mathrm{DWF}})_{x,s;x',s'}(M_5, m_f) = \delta_{s,s'} D^{\parallel}_{x,x'}(M_5) + \delta_{x,x'} D^{\perp}_{s,s'}(m_f). \tag{4.24}$$

The first term in Eq. (4.24), $D^{\parallel}_{x,x'}(M_5)$, is the usual four dimensional Dirac operator for massive Wilson fermions:

$$\begin{aligned} D^{\parallel}_{x,x'}(M_5) =& \frac{1}{2}\sum_{\mu=1}^{4}\left[(1-\gamma_\mu)U_\mu(x)\delta_{x+\hat{\mu},x'} + (1+\gamma_\mu)U^\dagger_\mu(x')\delta_{x-\hat{\mu},x'}\right] \\ &+ (M_5 - 4)\delta_{x,x'}. \end{aligned} \tag{4.25}$$

The second term, $D^{\perp}$, is independent of the gauge fields

$$\begin{aligned} D^{\perp}_{s,s'}(m_f) = & \frac{1}{2}\left[(1-\gamma_5)\delta_{s+1,s'} + (1+\gamma_5)\delta_{s-1,s'} - 2\delta_{s,s'}\right] \\ & -\frac{m_f}{2}\left[(1-\gamma_5)\delta_{s,L_s-1}\delta_{0,s'} + (1+\gamma_5)\delta_{s,0}\delta_{L_s-1,s'}\right]. \end{aligned} \tag{4.26}$$

In Eq. (4.25), M_5 is a Dirac mass term, and forms the height of the domain wall. The fermion mass m_f in Eq. (4.26) explicitly couples the wall at $s = 0$ with the wall at $s = L_s - 1$. The simplest way to define operators which create and destroy light four-dimensional quarks is

$$\begin{aligned} q(x) &= \frac{(1-\gamma_5)}{2}\Psi(x,0) + \frac{(1+\gamma_5)}{2}\Psi(x, L_s-1) \\ \bar{q} &= \bar{\Psi}(x,0)\frac{(1+\gamma_5)}{2} + \bar{\Psi}(x, L_s-1)\frac{(1-\gamma_5)}{2}. \end{aligned} \tag{4.27}$$

The fermion modes described by Eq. (4.27) describe left- and right-handed quark fields coupled to opposite walls in the fifth dimension. The residual mass, m_{res}, measures the residual chiral symmetry breaking due to the finite extend of the fifth dimension. The outcome of m_{res} is an additive renormalisation to the bare quark

masses,

$$m_f \to \tilde{m} = m_f + m_{\text{res}}. \tag{4.28}$$

However, it was shown in Ref. [35] that the current mass of the light Dirac fermion, m_q, is proportional to the bare quark mass m_f,

$$m_q = m_f M_5(2 - M_5), \tag{4.29}$$

so the fermion mass is *both* additively and multiplicatively renormalised.

At coarse lattice spacings, domain wall fermions exhibit increased chiral symmetry breaking. The residual mass can be approximated by [37]

$$m_{\text{res}} \sim R^4 \int_0^\infty d\lambda \rho(\lambda) e^{-L_s \lambda} \tag{4.30}$$

where λ are the eigenvalues of the four-dimensional Hamiltonian which describes the propagation of quarks in the fifth dimension and $\rho(\lambda)$ is the eigenvalue density. It was shown in [37] that a *mobility edge*, denoted λ_c exists, dividing the eigenstates into two regions. Eigenmodes with $\lambda > \lambda_c$ are extended, while eigenmodes with $\lambda < \lambda_c$ are localised. Picking out the dominant terms above and below the mobility edge in Eq. (4.30), the expected behaviour of m_{res} is

$$m_{\text{res}} = R_e^4 \rho(\lambda_c) \frac{e^{-\lambda_c L_s}}{L_s} + R_l^4 \rho(0) \frac{1}{L_s}, \tag{4.31}$$

where $\rho(0)$ is now the density of near-zero eigenmodes. The first term in Eq. (4.31) can be reduced by increasing the extent of the fifth dimension. Modern simulations are performed at relatively large L_s, so m_{res} is dominated by the second term in Eq. (4.31). Thus, in order to reduce the chiral symmetry breaking, $\rho(0)$ must be reduced. This can be achieved with the Dislocation Suppressing Determinant Ratio (DSDR). This is a term which is applied to the gauge action as a multiplicative weight. The DSDR term allows the near-zero eigenmodes to be suppressed, without eliminating the the very-near-zero modes which are necessary to ensure adequate topological sampling.

In order to make contact with the four-dimensional overlap theory, the five-dimensional path integral must also contain pseudofermion fields $\Phi, \overline{\Phi}$ which have the same indices as the fermion fields but are bosonic variables. These fields are often referred to as Pauli-Villars fields. The five-dimensional partition function is

$$Z = \int \mathcal{D}[\Psi\overline{\Psi}, \Phi, \overline{\Phi}, U]e^{-S}. \tag{4.32}$$

The action is given by

$$S = S_G(U) + S_F(\overline{\Psi}, \Psi, U) + S_{PV}(\overline{\Phi}, \Phi, U), \tag{4.33}$$

where S_G is an appropriate choice of gauge action such as Iwasaki, S_F was defined in Eq. (4.23) and the Pauli-Villars action is

$$S_{PV} = (\overline{\Phi}, \Phi, U) = \sum_{x,x',s,s'} \overline{\Phi}(x,s)D^{pf}(x,s;x',s')\Phi(x',s'), \tag{4.34}$$

with

$$D^{pf} = D_{\mathrm{DWF}}(M_5, 1), \tag{4.35}$$

and D_{DWF} was defined in Eq. (4.24). Neuberger showed that $\det(D_{DWF}) = \det(D^{ov}_{N5})\det(D^{\mathrm{pf}})$. Applying this relation to the path integral leads to,

$$\int \mathcal{D}[\Psi, \overline{\Psi}, \Phi, \overline{\Psi}]e^{(-S_F^{\mathrm{DWF}} - S_B^{\mathrm{pf}})} = \frac{\det(D^{DWF})}{\det(D^{\mathrm{pf}})} = \det(D^{ov}_{N5}), \tag{4.36}$$

so it is clear the the PV fields should be included to relate the five-dimensional DWF formalism to the four-dimensional overlap formalism. This step can be viewed as a change of integration variables with $\det[D^{\mathrm{pf}}]$ being the corresponding Jacobian.

4.4 Numerical Simulations

Even on a modest lattice, it would be impossible to evaluate the partition function of Eq. (4.5) in full. Consider for example a 10^4 space-time lattice, in which case the number of link variables is approximately 4×10^4. Each $SU(3)$ link variable is a

function of 8 real parameters, so there are 320000 integrations to be done. Using a mesh of only 10 points per integration, the path integral will be approximated by a sum of 10^{320000} terms. In order to evaluate the ensemble average, it is therefore necessary to employ statistical methods.

The expectation value of an observable $\Omega(\phi)$ that depends on a general field ϕ is

$$\langle\Omega\rangle = \frac{1}{Z}\int d\phi e^{-S(\phi)}\Omega(\phi). \tag{4.37}$$

In order to evaluate this expectation value, a sequence of field configurations $(\phi_1, \phi_2, \cdots \phi_n)$ is generated and chosen from the probability distribution

$$P(\phi_t)d\phi_t = \frac{1}{Z}e^{-S(\phi_t)}. \tag{4.38}$$

The observable is then measured on each configuration, and the ensemble average

$$\overline{\Omega} \equiv \frac{1}{N}\sum_{t=1}^{N}\Omega(\phi_t) \tag{4.39}$$

is calculated. In the limit that $N \to \infty$, the ensemble average is equal to the expectation value. The central limit theorem establishes the result that the ensemble average approaches a Gaussian distribution with $\langle\Omega\rangle$ as its mean and a standard deviation which falls as $1/\sqrt{N}$.

The QCD action is quadratic in the fermion fields, and these can be integrated out by hand, leading to the following expression for a typical correlation function

$$\langle\Omega(U, K(U))\rangle = \frac{1}{Z}\int \mathcal{D}[U]\Omega(U, S(U))e^{-(S_{\rm G}[U])}\det[K(U, m)]. \tag{4.40}$$

In Eq. (4.40) $K(U)$ is used to denote the Dirac operator. The gauge field configurations should be drawn according to the probability distribution

$$P(U_i) = \det[K(U, m)]e^{-(S_{\rm G}[U])}. \tag{4.41}$$

There are various Monte-Carlo algorithms designed to generate gauge ensembles

according to this probability distribution. In particular the ensembles studied in this thesis were generated using a variation of the Rational-Hybrid-Monte-Carlo (RHMC) algorithm, the details of which are beyond the scope of this thesis.

4.4.1 Reweighting

In order to overcome problems such as long autocorrelation times associated with using very light sea-quark masses in ensemble generation, simulations are usually performed with a heavier light-quark mass than the target valence light-quark mass. Reweighting is a technique that allows the sea-quark masses to be tuned after ensemble generation to match those used in the valence sector [38]. Let m_1 denote the light-sea-quark mass used in the ensemble generation and m_2 denote the target light-quark mass. The configurations that were generated with light sea quark mass m_1 can be reweighting to sea-quark mass m_2 by computing a reweighting factor $w(m_1, m_2)$ for each configuration on which measurements were performed. The reweighting factor is defined by

$$w(m_1, m_2) = \frac{\det\left\{K^\dagger(m_2)K(m_2)\right\}}{\det\left\{K^\dagger(m_1)K(m_1)\right\}}. \tag{4.42}$$

The goal is to calculate the expectation value of an observable $O[U]$ computed with light sea quark mass m_2. This quantity will be denoted $\langle O\rangle_2$. The reweighting factor allows $\langle O\rangle_2$ to be calculated from the ensemble generated with the sea-quark mass m_1. To see this, $\langle O\rangle_2$ is first written in terms of an ensemble generated with sea quark mass m_2. This is seen in Eq. (4.43), where Z_2 is the partition function for the sea quark mass m_2, and $K(m)$ denotes the Dirac operator generated with sea quark mass m. The discussion is phrased in $2+1$ flavours, so the quantity m_s is introduced to denote the mass of the strange quark.

$$\langle O\rangle_2 = \frac{1}{Z_2}\int DU O[U] e^{-S_G} \det\left\{\mathrm{K^\dagger(m_2)K(m_2)}\right\}\sqrt{\det\left\{(\mathrm{K^\dagger(m_s)K(m_s)}\right\}} \tag{4.43}$$

The expression for $\langle O \rangle_2$ is then modified by multiplying and dividing by both Z_1 and $\det\left\{\mathrm{K}^\dagger(\mathrm{m}_1)\mathrm{K}(\mathrm{m}_1)\right\}$, to obtain

$$\begin{aligned}\langle O \rangle_2 &= \frac{Z_1}{Z_2}\frac{1}{Z_1}\int DU\,[O[U]w(m_1,m_2)]\,e^{-S_G}\det\left\{\mathrm{K}^\dagger(\mathrm{m}_1)\mathrm{K}(\mathrm{m}_1)\right\}\sqrt{\det\left\{\mathrm{K}^\dagger(\mathrm{m}_\mathrm{s})\mathrm{K}(\mathrm{m}_\mathrm{s})\right\}} \\ &= \frac{\langle O[U]w(m_1,m_2)\rangle_1}{\langle w(m_1,m_2)\rangle_1}.\end{aligned} \tag{4.44}$$

In the last line of Eq. (4.44) the ratio Z_1/Z_2 has been rewritten as $\langle w(m_1,m_2)\rangle_1$, where the subscript 1 denotes that the ensemble average is for an ensemble generated with mass m_1.

A stochastic estimate can be used to evaluate the reweighting factor:

$$\begin{aligned}w(m_1,m_2) &= \frac{\int D\xi e^{-\left\langle \xi^\dagger K(m_1)^\dagger K(m_2)^{\dagger-1}K(m_2)^{-1}K(m_1)\xi - \xi^\dagger\xi\right\rangle}e^{-\xi^\dagger\xi}}{\int DU e^{-\xi^\dagger\xi}} \\ &= \left\langle e^{-\left\langle \xi^\dagger K(m_1)^\dagger K(m_2)^{\dagger-1}K(m_2)^{-1}K(m_1)\xi\right\rangle - \xi^\dagger\xi}\right\rangle_{1,\xi}\end{aligned} \tag{4.45}$$

where ξ is a stochastic variable drawn from a random Gaussian distribution $\exp(-\xi^\dagger\xi)$. The expectation value in the lower line of Eq. (4.45) is with respect to both ξ and the gauge fields at mass m_1, and these averages commute. It follows that the expectation value $\langle O \rangle_2$ can be evaluated with a single estimator s_i for the reweighting factor per configuration i:

$$s_i = e^{-\xi_i^\dagger K(U_i;m_1)^\dagger K(U_i;m_2)^{\dagger-1}K(U_i;m_2)^{-1}K(U_i;m_1)\xi_i - \xi_i^\dagger\xi_i}. \tag{4.46}$$

4.5 Measuring Observables

4.5.1 Propagators

After applying Wick's theorem, correlation functions contain products of spin matrices with quark propagators S.

The quark propagator is the inverse of the Dirac matrix, and satisfies γ_5-hermiticity:

$$S(x,t;x_0,t_0) = \gamma_5 S^\dagger(x_0,t_0;x,t)\gamma_5. \tag{4.47}$$

In this notation, the convention is that $S(x,t;x_0,t_0)$ is a propagator with a source at x_0, t_0 and a sink at x,t. The propagator matrix is extremely large, so typically only a subset is calculated. This is achieved by solving the matrix equation

$$\psi(\vec{x},t) = \sum_{\vec{y},t'} K^{-1}(\vec{x},t;\vec{y},t')\eta(\vec{y},t'). \tag{4.48}$$

In Eq. (4.48), η is a complex matrix source and ψ is the solution matrix, describing the propagator. This will be made more explicit below, when specific examples of sources are considered. This thesis makes use of several choices for the source η; these are the *wall-source*, *stochastic-source* and *cosine-source*.

In the case of the wall-source, η is set equal to the identity matrix at all points on a single timeslice at t_0. Solving Eq. (4.48) then leads to the wall-source propagator,

$$S^l(\vec{x},t;t_0) = \sum_{\vec{y}} S(\vec{x},t;\vec{y},t_0). \tag{4.49}$$

The notation is that $S^l(\vec{x},t;t_0)$ will be used to denote a light-quark propagator with a wall-source along the timeslice t_0 and a sink at space-time position $(\vec{x},t)$. Similarly $S^s(\vec{x},t;t_0)$ will be used to denote a strange-quark propagator with a wall source at t_0. Summing over the position of the sink leads to a propagator with a wall-sink:

$$S^q_W(t;t_0) = \sum_{\vec{x}} S^q((\vec{x},t);t_0), \tag{4.50}$$

where $q = l, s$ indicates a light/strange quark respectively.

Cosine wall sources are used in the calculation of correlation functions with non-zero momentum. The cosine source is defined by

$$\eta_{\cos}(\vec{x};\vec{p}) = \cos(p_x x)\cos(p_y y)\cos(p_z z) \tag{4.51}$$

on the timeslice at t_0. The components of momentum are given by $p_i = n_i(\pi/L)$ where n_i is an even or odd integer depending on whether periodic or antiperiodic boundary conditions were imposed on the quark field in direction i. The solution vector is thus

$$\psi(\underline{x}, t) = \sum_{\underline{y}} \eta_{\cos}(\vec{x}; \vec{p}) S(\vec{x}, t; \vec{y}, t_0). \tag{4.52}$$

Finally, stochastic sources are introduced. Stochastic sources will be important for evaluating eye-type diagrams in chapter 9. Elements of the source η with colour index a and spinor index α are randomly chosen from a Gaussian distribution D. A set of N random sources

$$\left\{ \eta^{(n)}(x)_{a,\alpha} \in D | n = 1 \ldots N \right\} \tag{4.53}$$

has the property that, in the limit $N \to \infty$

$$\left\langle \eta^{(n)}_{a,\alpha}(x) \eta^{\dagger(n)}_{b,\beta}(y) \right\rangle_n \equiv \frac{1}{N} \sum_{n=1}^{N} \eta^{(n)}_{a,\alpha}(x) \eta^{\dagger(n)}_{b,\beta}(y) \to \delta_{x,y} \delta_{a,b} \delta_{\alpha,\beta}. \tag{4.54}$$

The average over stochastic hits happens automatically when the ensemble average of a correlation function is performed. This means that only one stochastic "hit" is needed per propagator per configuration.

This calculation makes use of stochastic "wall" sources at $t = \tau$, where

$$\begin{array}{rl|l} \eta(x, t|\tau) & \in D & t = \tau \\ & = 0 & t \neq \tau. \end{array} \tag{4.55}$$

Propagators with stochastic wall sources along the timeslice t_0 will be denoted $S^q_R(\vec{x}, t_0; t_0)$, where once again $q = l, s$ labels the flavour of the quark.

4.5.2 Correlation Functions

Once the propagators have been calculated, the correlation functions can be measured. The correlation functions are traces over colour and spinor indices of the products of spin matrices and propagators mentioned previously.

After inserting a complete set of states, a generic correlation function can be written,

$$C(t) \equiv \left\langle O(\vec{0},t)O^{\dagger}(\vec{0},0)\right\rangle = \sum_{n} \langle 0|\, O\, |n\rangle \, \langle n|\, O^{\dagger}(\vec{0},0)\, \left|0(\vec{0},0)\right\rangle e^{-E_n t}. \tag{4.56}$$

At large enough t, excited states with $n > 0$ will decay and only the ground state will remain. For mesons, propagation in t and $T - t$ is identical, and the expected form for the correlation function is

$$C(t) = 2A_0 \cosh((T/2 - t)E_0)e^{-TE_0/2}. \tag{4.57}$$

By fitting the correlation functions as a function of t to the fit form in Eq. (4.57), it is straightforward to extract the meson masses. In order to determine a suitable fitting region where excited states have died away and the remaining signal is that of the ground state, effective mass plots are examined. The effective mass m_{eff} is found by solving

$$\frac{C(t)}{C(t+1)} = \frac{\cosh(m_{\text{eff}}(T/2 - t))}{\cosh(m_{\text{eff}}(T/2 - t - 1))} \tag{4.58}$$

at each time t. A plot of the effective mass should show a plateau in the region where excited states can be neglected.

In this thesis all fits are performed using uncorrelated χ^2 fits. The error on each fit is then determined using the jackknife technique as follows. Consider a data set of N configurations and an observable θ, and let $\hat{\theta}$ denote the value of the observable computed using all N configurations. In the jackknife procedure N subsets are constructed by removing the nth ($n = 1, \ldots, N$) configuration from the original set. The value of the observable θ_n is determined for each subset. The variance is then

$$\sigma^2_{\hat{\theta}} \equiv \frac{N-1}{N} \sum_{n=1}^{N} (\theta_n - \hat{\theta})^2, \tag{4.59}$$

and the square root of the variance estimates the standard deviation on $\hat{\theta}$.

Measurements made on different ensembles can be assumed to be statistically independent, and the contributions from the different ensembles should be kept

separate so as to avoid accidental cancellations. This can be accommodated in the jackknife procedure by embedding the jackknife series of observables in an extended series that includes all the separate ensembles. Let $\{\overline{\theta}^X\}$ denote the jackknife distribution of the observable θ measured on ensemble X. The extended distribution of θ measured on several ensembles labelled $A, B, \cdots$ is

$$\{\overline{\theta}\} = (\{\overline{\theta}^A\}, \{\overline{\theta}^B\}, \ldots). \tag{4.60}$$

The error on the total distribution is then found by combining in quadrature the errors from the different distributions

$$\sigma^2(\{\overline{\theta}\}) = \sigma^2(\{\overline{\theta}^A\}) + \sigma^2(\{\overline{\theta}^B\}) + \ldots. \tag{4.61}$$

This technique, known in the literate as the *super-jackknife* technique, is described in detail in [39, 40].

Chapter 5

Non-Perturbative Renormalisation

In order to obtain physical results for the $K \to \pi\pi$ decay amplitudes, the $\Delta S = 1$ four-quark operators must be renormalised at the same scale and in the same scheme as the Wilson coefficients in the effective Hamiltonian. Since the Wilson coefficients were evaluated in the $\overline{\text{MS}}$-NDR scheme in Chapter 3, this means renormalising the operators in the $\overline{\text{MS}}$-NDR scheme. A non-perturbative treatment for the renormalisation of the four-quark operators is desirable in order to avoid lattice perturbation theory, which frequently converges more slowly than continuum perturbation theory. In order to perform the non-perturbative renormalisation (NPR) of the four-quark operators an intermediate scheme which is independent of the regulator (RI) is chosen so that the renormalisation can be implemented both numerically on the lattice and in continuum perturbation theory. This allows the lattice results to be converted to the $\overline{\text{MS}}$-NDR scheme, which is not directly implementable on the lattice. The numerical renormalisation procedure used is based on the Rome-Southampton method introduced in [41].

This thesis describes two separate calculations of $K \to \pi\pi$ matrix elements, a calculation of only the $\Delta I = 3/2$ channel performed at nearly-physical kinematics on the "IDSDR" ensemble, and a full calculation on the smaller "16^3 Iwasaki" ensemble. The latter calculation includes additional operators and suffers from

difficulties due to operator mixing that are not present in the $\Delta I = 3/2$ calculation. With this in mind, this chapter includes two separate results sections for the NPR; Section 5.1 gives the NPR factors for the $\Delta I = 3/2$ opeartors, calculated on the IDSDR ensemble, while Section 5.2 gives the NPR factors for all seven operators in the chiral basis (defined in Eq. (3.9)), calculated on the 16^3 Iwasaki ensemble.

The successful implementation of the Rome-Southampton renormalisation procedure requires that a window in lattice momentum must exist, such that the renormalisation scale μ must satisfy

$$\Lambda_{\mathrm{QCD}} \ll \mu \ll 1/a. \tag{5.1}$$

The scale μ must be small enough that discretisation effects are suppressed in the numerical renormalisation to the RI scheme, but must also be large enough for the perturbative matching to $\overline{\mathrm{MS}}$ to converge. This window can be extended if a non-perturbative *step-scaling* function is introduced. Such a function allows renormalisation constants computed at a low energy scale to be run non-perturbatively up to a higher scale more suitable for continuum perturbation theory.

In RI schemes, one imposes the renormalisation condition that amputated Green's functions with given off-shell external states at a given momentum point and in a fixed gauge coincide with their tree level value. In practice this renormalisation condition is imposed by tracing the amputated Green's function Λ with a suitable projection operator P, such that

$$\frac{Z_{\mathcal{O}}}{Z_q^2} \left[\mathrm{Tr} P\Lambda\right]\Big|_{q^2=\mu^2} = F \tag{5.2}$$

where

$$F = \lim_{\alpha_s \to 0} \left[P\Lambda\right]\Big|_{q^2=\mu^2} \tag{5.3}$$

The RI-SMOM scheme was introduced in [42] and generalised for the four-quark operator in [43]. The "SMOM" kinematics specifiy that the momentum of the

four-quark operator being renormalised be symmetric so that no exceptional channels are available, i.e. there are no channels where zero momentum is inserted at the operator. This prevents IR chiral symmetry breaking effects. For example, for the renormalisation of the $(27,1)$ operator defined in Eq. (3.12), the Green's function to be calculated is

$$d(p_1)\overline{s}(-p_2) \to \overline{d}(-p_1)u(p_2) \tag{5.4}$$

and the momenta are chosen to satisfy $p_1^2 = p_2^2 = (p_1 - p_2)^2 = \mu^2$.

Since $Q_{(27,1)}$ is multiplicatively renormalisable, the relation between the bare lattice and renormalised operator is of the form:

$$Q_{(27,1)}^{(\mathrm{I_v},\mathrm{I_q})} = Z_{(27,1)}^{(\mathrm{I_v},\mathrm{I_q})}\, Q_{(27,1)}^{(\mathrm{latt})}\,, \tag{5.5}$$

where $\mathrm{I_v}$ labels the choice of the intermediate (one-particle irreducible) vertex renormalisation scheme and $\mathrm{I_q}$ the intermediate scheme for the wave function renormalisation. The index "latt" indicates that the operator on the right-hand side is the bare lattice operator. The overall renormalisation constant is obtained by evaluating a trace of Λ with a projection operator $P^{(\mathrm{I_v})}$

$$Z_{(27,1)}^{(\mathrm{I_v},\mathrm{I_q})} = Z_q^{(\mathrm{I_q})\,2}\, \frac{1}{P_{\alpha\beta,\gamma\delta}^{(\mathrm{I_v})\,ij,kl}\, \Lambda_{\alpha\beta,\gamma\delta}^{(27,1)\,ij,kl}}\,, \tag{5.6}$$

where $Z_q^{(\mathrm{I_q})}$ is the wave function renormalisation constant which will be discussed below. The two choices that are made for the projection operators are labelled by $\mathrm{I_v} = \gamma_\mu$ or $\mathrm{I_v} = \not{q}$ [43]:

$$P_{\alpha\beta,\gamma\delta}^{(\gamma^\mu)\,ij,kl} = \frac{1}{128N(N+1)} \left[(\gamma^\mu)_{\beta\alpha}(\gamma^\mu)_{\delta\gamma} + (\gamma^\mu\gamma^5)_{\beta\alpha}(\gamma^\mu\gamma^5)_{\delta\gamma}\right] \delta^{ij}\delta^{kl} \tag{5.7}$$

$$P_{\alpha\beta,\gamma\delta}^{(\not{q})\,ij,kl} = \frac{1}{32q^2N(N+1)} \left[(\not{q})_{\beta\alpha}(\not{q})_{\delta\gamma} + (\not{q}\gamma^5)_{\beta\alpha}(\not{q}\gamma^5)_{\delta\gamma}\right] \delta^{ij}\delta^{kl}\,, \tag{5.8}$$

where $N = 3$ is the number of colours. These projectors are constructed to give 1 when contracted with the tree-level results for $\Lambda_{\alpha\beta,\gamma\delta}^{(27,1)\,ij,kl}$.

For the wave function renormalisation, schemes defined as RI-SMOM and RI-SMOM$_{\gamma_\mu}$ in ref. [42] are used, which for compactness of notation, are labeled as $\mathrm{I_q} = \not{q}$ and $\mathrm{I_q} = \gamma_\mu$ respectively. The corresponding renormalisation constants are defined as

$$Z_q^{(\not{q})} = \frac{q^\mu}{12q^2}\,\mathrm{Tr}[\Lambda_V^\mu \not{q}] \qquad \text{and} \qquad Z_q^{(\gamma_\mu)} = \frac{1}{48}\,\mathrm{Tr}[\Lambda_V^\mu \gamma^\mu]\,, \tag{5.9}$$

where Λ_V^μ is the amputated Green function of the conserved vector current. This completes the description of the determination of the renormalisation constant for $Q_{(27,1)}$ in the four schemes in which each of $\mathrm{I_q}$ and $\mathrm{I_v}$ are either $\not{q}$ or γ_μ.

In general, operators will mix under renormalisation. The renormalisation constants for the four-quark operators are then defined such that

$$\vec{Q}_R^{\mathrm{I_v},\mathrm{I_q}} = Z^{(\mathrm{I_v},\mathrm{I_q})}\vec{Q}^{\mathrm{latt}}. \tag{5.10}$$

The vector $\vec{Q}$ represents a column vector of $\Delta S = 1$ four-quark operators and $Z^{(\mathrm{I_v},\mathrm{I_q})}$ is a matrix. Operators in an irreducible representation of a given symmetry only mix with operators transforming in the same irreducible representation. Consequently, if a chiral basis is used to describe the operators, the matrix of renormalisation constants Z will be block diagonal.

5.1 Renormalisation Constants for the IDSDR Lattices

The renormalisation of the remaining two $\Delta I = 3/2$ operators is a natural extension of the renormalisation of the $(27, 1)$ operator, outlined in the previous section.

The operators $O_{(8,8)}$ and $O_{(8,8)\mathrm{mx}}$ mix under renormalisation. Two projectors are

now defined for each of the electroweak penguin operators as follows:

$$\left[P^{(\gamma^\mu)}_{(8,8)}\right]^{ij,kl}_{\alpha\beta,\gamma\delta} = \left[(\gamma^\mu)_{\beta\alpha}(\gamma^\mu)_{\delta\gamma} - \left(\gamma^\mu\gamma^5\right)_{\beta\alpha}\left(\gamma^\mu\gamma^5\right)_{\delta\gamma}\right]\delta^{ij}\delta^{kl} \tag{5.11}$$

$$\left[P^{(\gamma^\mu)}_{(8,8)\text{mx}}\right]^{ij,kl}_{\alpha\beta,\gamma\delta} = \left[(\gamma^\mu)_{\beta\alpha}(\gamma^\mu)_{\delta\gamma} - \left(\gamma^\mu\gamma^5\right)_{\beta\alpha}\left(\gamma^\mu\gamma^5\right)_{\delta\gamma}\right]\delta^{il}\delta^{kj} \tag{5.12}$$

$$\left[P^{(\not{q})}_{(8,8)}\right]^{ij,kl}_{\alpha\beta,\gamma\delta} = \frac{1}{q^2}\left[(\not{q})_{\beta\alpha}(\not{q})_{\delta\gamma} - \left(\not{q}\gamma^5\right)_{\beta\alpha}\left(\not{q}\gamma^5\right)_{\delta\gamma}\right]\delta^{ij}\delta^{kl} \tag{5.13}$$

$$\left[P^{(\not{q})}_{(8,8)\text{mx}}\right]^{ij,kl}_{\alpha\beta,\gamma\delta} = \frac{1}{q^2}\left[(\not{q})_{\beta\alpha}(\not{q})_{\delta\gamma} - \left(\not{q}\gamma^5\right)_{\beta\alpha}\left(\not{q}\gamma^5\right)_{\delta\gamma}\right]\delta^{il}\delta^{kj} \tag{5.14}$$

The renormalisation constants for these electroweak penguin (EWP) operators are then determined by solving

$$\frac{1}{Z_q^2}ZM = F \tag{5.15}$$

where M is the matrix constructed with elements

$$M_{ab} \equiv \text{Tr}\left[[P_b]^{ij,kl}_{\alpha\beta,\gamma\delta}\,[\Lambda^a]^{ij,kl}_{\alpha\beta,\gamma\delta}\right] \tag{5.16}$$

where a, b label the $(8,8)$ and $(8,8)_{mx}$ operators.

5.1.1 Step-scaling

In order to minimise discretisation effects in the calculation of the Z-factors on the IDSDR lattices, where a is large ($a^{-1} = 1.364$ GeV on the IDSDR ensemble, see chapter 8) and only one lattice spacing is available, the matching point is chosen to be the low scale $\mu_0 = 1.136$ GeV. Note that the matching point is actually chosen in lattice units, and can only be determined in physical units once the lattice spacing has been calculated. This leads ot the seemingly arbitrary value $\mu_0 = 1.136$ GeV. A step-scaling function[44, 45] is evaluated to convert the results to 3 GeV, where perturbation theory is more convergent than the conventional matching scale of 2 GeV. The use of step-scaling, and in particular its recent generalization to the RI-MOM and RI-SMOM schemes being used in this thesis [43, 46, 47], allows the renormalisation constants evaluated at $\mu = 1.136$ GeV to be related to renormalisation constants at 3 GeV, so that perturbative matching to $\overline{\text{MS}}$ may take

place. The step-scaling approach can also be generalised to operators which mix under renormalisation [48, 49] and this is applied in this calculation.

The renormalisation constants $Z^{(\mathrm{I_v},\mathrm{I_q})}_{(27,1)}(\mu_0)$ and $Z^{(\mathrm{I_v},\mathrm{I_q})}_{ab}(\mu_0)$, $(a,b=(8,8),(8,8)_{\mathrm{mx}})$, are evaluated on two ensembles, each generated with $2+1$ flavours of domain wall fermions and the Iwasaki gauge action. These lattices have dimensions $32^3\times 64\times 16$ and $24^3\times 64\times 16$ and are generated at $\beta=2.25$ and $\beta=2.13$ respectively [50, 51]. Renormalization constants on the Iwasaki ensembles were presented in [48].

The benefit of doing this is that on these finer lattices the renormalisation constants can be run non-perturbatively from $\mu_0=1.136$ GeV to a larger scale $\mu=3$ GeV. Taking $Q_{(27,1)}$ as an example, the step-scaling function on the finer lattices is defined as:

$$\Sigma^{(\mathrm{I_v},\mathrm{I_q})}_{(27,1)}(\mu,\mu_0,a)=\lim_{m\to 0}\left[Z^{(\mathrm{I_v},\mathrm{I_q})}_{(27,1)}(\mu,a,m)\left(Z^{(\mathrm{I_v},\mathrm{I_q})}_{(27,1)}(\mu_0,a,m)\right)^{-1}\right], \tag{5.17}$$

where m is the quark mass. Since we have results at two different lattice spacings on the finer Iwasaki lattices we can perform the continuum extrapolation and define the continuum step-scaling functions as

$$\sigma^{(\mathrm{I_v},\mathrm{I_q})}_{(27,1)}(\mu,\mu_0)=\lim_{a\to 0}\Sigma^{(\mathrm{I_v},\mathrm{I_q})}_{(27,1)}(\mu,\mu_0,a)\,. \tag{5.18}$$

The step-scaling function $\sigma_{(27,1)}(\mu,\mu_0)$ describes the continuum non-perturbative running of the 4 quark operator $Q_{(27,1)}$ in a given scheme. Because it does not depend on the lattice action, it can be used to run the Z factor obtained from the IDSDR lattice at the low scale μ_0 to a higher energy μ where perturbation theory is more convergent. Finally, the operator $Q_{(27,1)}$, renormalised in the intermediate scheme $(\mathrm{I_v},\mathrm{I_q})$ at a perturbative scale μ is related to the IDSDR lattice operator by:

$$Q^{(\mathrm{I_v},\mathrm{I_q})}_{(27,1)}(\mu)=\sigma^{(\mathrm{I_v},\mathrm{I_q})}_{(27,1)}(\mu,\mu_0)\,Z^{(\mathrm{I_v},\mathrm{I_q})}_{(27,1)}(\mu_0)\,Q^{(\mathrm{latt})}_{(27,1)}. \tag{5.19}$$

For the electroweak operators the above equations become 2×2 matrix equations with the constants $Z^{(\mathrm{I_v},\mathrm{I_q})}_{(27,1)}$ replaced by the matrices $Z^{(\mathrm{I_v},\mathrm{I_q})}_{ab}$ and similarly for the

step-scaling factors.

5.1.2 NPR Results

The results for the renormalisation constants in the (γ^μ, γ^μ) and $(\not{q}, \not{q})$ schemes, evaluated at $\mu_0 = 1.136$ GeV are:

$$Z^{(\gamma^\mu,\gamma^\mu)}(\mu_0) = \begin{pmatrix} 0.443\,(1) & 0 & 0 \\ 0 & 0.505\,(1) & -0.114\,(1) \\ 0 & -0.022\,(3) & 0.231\,(2) \end{pmatrix} \tag{5.20}$$

$$Z^{(\not{q},\not{q})}(\mu_0) = \begin{pmatrix} 0.489\,(1) & 0 & 0 \\ 0 & 0.510\,(2) & -0.116\,(1) \\ 0 & -0.077\,(6) & 0.305\,(4) \end{pmatrix}, \tag{5.21}$$

where the quoted errors are statistical only.

The conversion to $\overline{\text{MS}}$-NDR is calculated to one loop in perturbation theory. The renormalisation constants in the $\overline{\text{MS}}$-NDR scheme are related to those in the intermediate RI schemes by the matching matrix R^{I_v,I_q} according to

$$Z^{\overline{\text{MS}}}_{(\text{I}_\text{v},\text{I}_\text{q})} = R^{(\text{I}_\text{v},\text{I}_\text{q})} Z^{(\text{I}_\text{v},\text{I}_\text{q})} \tag{5.22}$$

The matching factors $R^{(\text{I}_\text{v},\text{I}_\text{q})}$ are known at one loop [32]. Using $\alpha_s^{\overline{\text{MS}}}(3\text{ GeV}) = 0.24544$ the SMOM $\to \overline{\text{MS}}$ matching matrices are

$$R^{(\gamma^\mu,\gamma^\mu)}(3\text{ GeV}) = \begin{pmatrix} 1.00414 & 0 & 0 \\ 0 & 1.00084 & -0.00253 \\ 0 & -0.03152 & 1.08781 \end{pmatrix} \tag{5.23}$$

$$R^{(\not{q},\not{q})}(3\text{ GeV}) = \begin{pmatrix} 0.99112 & 0 & 0 \\ 0 & 1.00084 & -0.00253 \\ 0 & -0.01199 & 1.02921 \end{pmatrix} \tag{5.24}$$

The (γ^μ, γ^μ) and $(\not{q}, \not{q})$ schemes are preferred over the $(\gamma^\mu, \not{q})$ and $(\not{q}, \gamma^\mu)$ because they are better approximated by perturbation theory for $\mu \approx 3$ GeV. Retaining the labels (γ^μ, γ^μ) and $(\not{q}, \not{q})$ as a reminder of the intermediate scheme used in the NPR, the final results for the renormalisation constants in the $\overline{\text{MS}}$-NDR scheme at 3 GeV are

$$Z^{\overline{\text{MS}}}_{(\gamma^\mu,\gamma^\mu)}(3\text{ GeV}) = \begin{pmatrix} 0.419(2)(1) & 0 & 0 \\ 0 & 0.479(5)(8) & -0.022(5)(20) \\ 0 & -0.047(13)(11) & 0.552(19)(28) \end{pmatrix} \tag{5.25}$$

$$Z^{\overline{\text{MS}}}_{(\not{q},\not{q})}(3\text{ GeV}) = \begin{pmatrix} 0.424(4)(4) & 0 & 0 \\ 0 & 0.472(6)(8) & -0.020(5)(21) \\ 0 & -0.067(23)(30) & 0.572(28)(20) \end{pmatrix} \tag{5.26}$$

where the first error is statistical and the second error is systematic. The systematic error has been propagated through from the continuum extrapolation of the step-scaling function. A conservative estimate of this error is made, using the difference between the result for the step-scaling function on the finest Iwasaki lattice and the continuum extrapolation.

Following conversion to the $\overline{\text{MS}}$ scheme, the renormalisation constants should no longer depend on the choice of intermediate scheme. The difference in Eq. (5.25) and Eq. (5.26) can be interpreted as a measure of the truncation error in the continuum perturbation theory, as well as giving some indication of the scaling errors on the DSDR lattices.

5.2 Renormalisation Constants for the 16^3 Iwasaki Lattices

The renormalisation factors for all seven of the $\Delta S = 1$ operators in chiral basis defined in Eq. (3.9) were calculated on the 16^3 Iwasaki ensemble in [52]. RI-SMOM kinematics were used, while the choice of operator projector corresponded to the $\not{q}$ scheme. The resulting renormalisation matrix $Z^{\text{RI}}_{ij}(\mu, a)$ can be used to convert

the lattice normalization into that of the RI scheme:

$$Q^{\mathrm{RI}}(\mu)_i = \sum_{j=1}^{7} Z_{ij}^{\mathrm{lat}\to\mathrm{RI}}(\mu, a) Q'_j. \tag{5.27}$$

However, these equalities hold only when the operators appear in physical matrix elements of on-shell states. Since the RI/SMOM renormalisation conditions are being imposed for off-shell, gauge-fixed external quark lines, a larger number of operators should in principal be included, rather than the minimal set of seven independent operators which can represent all gauge invariant matrix elements between physical states of H_W. Therefore, a correspondingly larger set of conditions must also be employed to distinguish among this larger set of operators. This larger set of operators is required if the calculation is to use these RI operators to reproduce all the gauge-fixed, off-shell Green's functions that can be constructed using the original, chiral basis of lattice operators Q'_i.

However, the ultimate goal is to evaluate on-shell, physical matrix elements of these operators. For such matrix elements there are only seven independent operators and the expanded set of operators referred to above can be collapsed back to the seven, four-quark, chiral basis operators Q_i^{RI}. This is the meaning of the 7×7 matrix $Z^{\mathrm{lat}\to\mathrm{RI}}$ matrix given in Tab. 5.1: gauge symmetry and the equations of motion must be imposed to reduce to seven the RI-normalized operators to which the seven lattice operators are equated. In the calculation of $Z^{\mathrm{lat}\to\mathrm{RI}}$ presented in Ref. [52] such extra operators are neglected. For all but one, this might be justified because these operators enter only at two loops or beyond and the perturbative coefficients that we are using in later steps are computed at only one loop. A single operator, given in Eq. 146 of Ref. [20] and Eq. 12 of Ref. [32] does appear at one loop but has also been neglected because it is expected to give a smaller contribution than other two-quark operators with quadratically divergent coefficients whose effects are indeed small. A final imperfection in the results presented in Tab. 5.1 is that the subtraction of a third dimension-four, two-quark operator which contains a total derivative was not performed. However, the effect of subtracting this third operator is expected to be similar to those of the two

Table 5.1: *Z/Z_q^2 in the RI-SMOM($\gamma_\mu \not{q}$) scheme at 2.15 GeV*

	1	2	3	4	5	6	7
1	0.825(7)	0	0	0	0	0	0
2	0	0.882(38)	-0.111(41)	-0.009(12)	0.010(10)	0	0
3	0	-0.029(69)	0.962(92)	0.013(22)	-0.011(25)	0	0
4	0	-0.04(12)	-0.01(13)	0.924(42)	-0.149(35)	0	0
5	0	0.17(18)	0.08(23)	-0.042(55)	0.649(63)	0	0
6	0	0	0	0	0	0.943(8)	-0.154(9)
7	0	0	0	0	0	-0.0636(53)	0.680(11)

operators which were subtracted, effects which were not visible outside of the statistical errors (see *e.g.* Tabs. XIV and XVIII in Ref. [20]).

Results for the inverse of Z/Z_q^2, evaluated at 2.15 GeV at three different unitary mass points are tabulated in tables 40-42 of [52]. Since there is no visible mass dependence, the error-weighted average of the three tables is used in order to reduce the statistical error. The final table of renormalisation constants Z/Z_q^2 is presented in Tab. 5.1. The results of Tab. 5.1 must be converted to the $\overline{\text{MS}}$-NDR scheme. The conversion factor $R^{(\not{q},\gamma_\mu)}$ which relates $Z^{(\not{q},\gamma_\mu)}$ to $Z^{\overline{\text{MS}}}_{(\not{q},\gamma_\mu)}$ is taken from Tab. VIII of Ref. [32] using $\alpha_s(2.15\text{ GeV}) = 0.286758$, giving

$$R^{(\not{q},\gamma_\mu)} = \begin{pmatrix} 0.944 & 0 & 0 & 0 & 0 & 0 & 0 \\ 0 & 0.937 & 0.00725 & 0 & 0 & 0 & 0 \\ 0 & 0.00218 & 0.925 & 0.00169 & -0.00507 & 0 & 0 \\ 0 & 0 & 0 & 0.940 & -0.00296 & 0 & 0 \\ 0 & -0.0380 & -0.0887 & -0.0241 & 1.00 & 0 & 0 \\ 0 & 0 & 0 & 0 & 0 & 0.940 & -0.00296 \\ 0 & 0 & 0 & 0 & 0 & -0.0368 & 1.04 \end{pmatrix}. \tag{5.28}$$

Using $Z_q = 0.8016$, which was evaluated using the $\not{q}$ scheme defined in Eq. (5.9) and the results of Eq. (5.28) the renormalisation constants in the $\overline{\text{MS}}$ at 2.15 GeV are given in Tab. 5.2.

Table 5.2: *Z in the $\overline{MS}$-NDR scheme at 2.15 GeV*

	1	2	3	4	5	6	7
1	0.500	0	0	0	0	0	0
2	0	0.531	-0.0621	-0.00516	0.00594	0	0
3	0	-0.0169	0.571	0.00888	-0.00891	0	0
4	0	-0.0217	-0.00319	0.558	-0.0913	0	0
5	0	0.0878	-0.00266	-0.0418	0.422	0	0
6	0	0	0	0	0	0.570	-0.0944
7	0	0	0	0	0	-0.0649	0.459

Chapter 6

Two Particles in a Finite Volume

The Lüscher quantisation condition gives the two-pion energy spectrum on a lattice in terms of the s-wave phase shift δ and a kinematic function ϕ,

$$\delta(k) + \phi(q) = n\pi, \tag{6.1}$$

where k is related to the centre of mass energy by $E = 2\sqrt{m_\pi^2 + k^2}$ and $q = kL/2\pi$ where L is the length of the lattice. Lüscher's derivation of this formula was based on non-relativistic quantum mechanics [53]. An alternative derivation of the quantisation condition, based on summation formulae which relate sums and integrals and formulated entirely in field theory, was presented in [54] and is described in this chapter.

6.1 Summation Formulae

The derivation begins with the Poisson summation formula,

$$\frac{1}{L^3}\sum_{\vec{k}} g(\vec{k}) = \int \frac{d^3k}{(2\pi)^3} g(\vec{k}) + \sum_{\vec{l}\neq\vec{0}} \int \frac{d^3k}{(2\pi)^3} e^{iL\vec{l}.\vec{k}} g(\vec{k}), \tag{6.2}$$

where the summation on the left-hand side is over all integer values of $\vec{n} = (n_1, n_2, n_3)$, with $\vec{k} = 2\pi\vec{n}/L$, and the summation on the right-hand side is over integer values of $\vec{l} = (l_1, l_2, l_3)$ excluding $l = (0, 0, 0)$. For functions $f(\vec{k})$ whose

Fourier transforms $\tilde{f}(\vec{r})$ are non-singular and are either contained in a finite volume or decrease exponentially as $|r| \to \infty$, the Poisson summation formula allows the sum on the left hand side of Eq. (6.2) to be replaced by an integral,

$$\frac{1}{L^3} \sum_{\vec{k}} f(\vec{k}) = \int \frac{d^3k}{(2\pi)^3} f(\vec{k}). \tag{6.3}$$

Eq. (6.3) is valid up to exponentially small corrections, as the right-most term in Eq. (6.2) decreases at least exponentially as the box size is sent to infinity.

Later we will show that for two-pion correlators with energy below the inelastic threshold, the finite-volume corrections are contained in summations of the form

$$S(\vec{q}) \equiv \frac{1}{L^3} \sum_{\vec{k}} \frac{f(\vec{k})}{q^2 - k^2} \tag{6.4}$$

where it is assumed that $q^2 \equiv |\vec{q}|^2$ is such that there is no term in the sum with $k^2 \equiv |\vec{k}|^2 = q^2$ and that $f(\vec{k})$ has the properties described above. In particular it is important that $f(\vec{k})$ has no singularities for real $\vec{k}$. Eq. (6.3) cannot be applied to Eq. (6.4) because there is a singularity at $k^2 = q^2$. Working in spherical polar coordinates $\vec{k} = (k, \theta, \phi)$, f is expanded in spherical harmonics as follows

$$f(\vec{k}) = \sum_{l=0}^{\infty} \sum_{m=-l}^{l} f_{lm}(k) k^l \sqrt{4\pi} Y_{lm}(\theta, \phi), \tag{6.5}$$

leading to

$$S(\vec{q}) = \sum_{l,m} S_{lm}(q) \text{ where } S_{lm}(q) \equiv \frac{1}{L^3} \sum_{\vec{k}} \frac{f_{lm}(k)}{q^2 - k^2} k^l \sqrt{4\pi} Y_{lm}(\theta, \phi). \tag{6.6}$$

The authors of [54] proceed by subtracting from the summand a function chosen to cancel the pole at $k^2 = q^2$. The subtraction includes a factor $\exp(\alpha(q^2 - k^2))$ in order to avoid introducing an ultraviolet divergence. Once the pole has been cancelled, Eq. (6.3) can be applied. The result, which is valid up to exponentially

small corrections, is

$$\frac{1}{L^3}\sum_{\vec{k}}\frac{f_{lm}(k)-f_{lm}(q)e^{\alpha(q^2-k^2)}}{q^2-k^2}\sqrt{4\pi}k^l Y_{lm}(\theta,\phi) = \int\frac{d^3k}{(2\pi)^3}\frac{f_{lm}(k)-f_{lm}(q)e^{\alpha(q^2-k^2)}}{q^2-k^2}k^l\sqrt{4\pi}Y_{lm}(\theta,\phi). \tag{6.7}$$

It is now possible to find an expression for $S_{lm}(q)$:

$$S_{lm}(q) = \delta_{l,0}\mathcal{P}\int\frac{d^3k}{(2\pi)^3}\frac{f_{00}(k)}{q^2-k^2}\sqrt{4\pi}Y_{00} + f_{lm}(q)\mathcal{Z}_{lm}(q) \tag{6.8}$$

where

$$Z_{lm}(q) = \frac{1}{L^3}\sum_{\vec{k}}\frac{e^{\alpha(q^2-k^2)}}{q^2-k^2}k^l\sqrt{4\pi}Y_{lm}(\theta,\phi) - \delta_{0,l}\mathcal{P}\int\frac{d^3k}{(2\pi)^3}\frac{e^{\alpha(q^2-k^2)}}{q^2-k^2}k^l\sqrt{4\pi}Y_{00}. \tag{6.9}$$

The principal value prescription, $\mathcal{P}$ has been chosen to regularise the integrals in Eq. (6.8). The function $Z_{lm}(q)$ in Eq. (6.9) appears to depend on α. However, in the case of $l = 0$, the sum and integral in Eq. (6.9) both have an ultraviolet divergence which is proportional to $\alpha^{-1/2}$ and these cancel. This is one example of the more general result that $Z_{lm}(q)$ should not depend on the ultraviolet regulator, which has been checked numerically by the authors of [54].

6.2 Derivation of the Quantisation Condition

The two-pion energy spectrum in a finite volume can be established by studying the correlation function $C(t)$. The correlation function is expressed in terms of interpolating operators $\sigma(\vec{x},t)$ which overlap with two-pion states. If the two-pion state is studied in the centre of mass frame, $C(t)$ can be written as

$$C(t) = \langle 0|\,\sigma(t)\sigma^\dagger(\vec{0},0)\,|0\rangle\,, \tag{6.10}$$

where

$$\sigma(t) = \int d^3x\,\sigma(\vec{x},t) \tag{6.11}$$

projects onto zero three-momentum, and the time ordering in Eq. (6.10) is implicit. The two-pion correlator in energy space is

$$\tilde{C}(E) = \int dt\, e^{-iEt} C(t). \tag{6.12}$$

The two-pion energy spectrum in an infinite volume in Minkowski space is described by a branch-cut in the s-plane beginning at $s = 4m^2$. This branch-cut is replaced by a series of poles if the two-pion scattering is restricted to a finite volume where momenta are quantised. Thus the energy spectrum in a finite volume can be determined from the location of these poles.

The two-pion correlator can be expressed in terms of the amputated two-particle irreducible four-particle correlation function K, through the series shown in Fig. 6.1. The two-pion energy E is chosen to lie below the four-pion threshold, $0 < E^2 < 16m^2$, so there are no intermediate states with four or more pions and the finite volume effects in K are exponentially suppressed. The only power-law finite-volume corrections arise through the two-pion loops in Fig. 6.1.

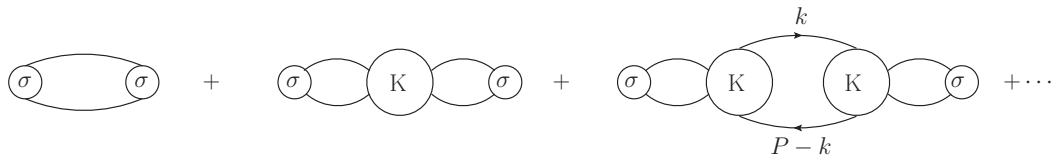

Figure 6.1: *Diagramatic expansion of the two-pion correlator. K is the amputated two-particle irreducible four-particle correlation function and $P = (E, 0)$.*

If the time extent is infinite, the generic loop integration appearing in Fig. 6.1 is of the form

$$I \equiv \frac{1}{L^3} \sum_{\vec{k}} \int \frac{dk_0}{2\pi} \frac{f(k_0, \vec{k})}{(k_0^2 - \omega_k^2 + i\epsilon)((E - k_0)^2 - \omega_k^2 + i\epsilon)} \tag{6.13}$$

where $\omega_k = \sqrt{\vec{k}^2 + m^2}$. A minus sign arising from a factor of i^2 from the propagators has been left out, but will be corrected for later. All remaining energy-momentum dependence arising from the renormalised propagators, the kernels either side of the loop integral, or the matrix element of the operator σ at the ends of the diagram, is contained in the function f. After performing the k_0

integral in Eq. (6.13), the loop summation becomes

$$I = -i\frac{1}{L^3}\sum_{\vec{k}}\left\{\frac{f(\omega_k,\vec{k})}{2\omega_k((E-\omega_k)^2-\omega_k^2)}+\frac{f(E+\omega_k,\vec{k})}{2\omega_k((E+\omega_k)^2-\omega_k^2)}\right\}. \tag{6.14}$$

For $0 < E^2 < 16m^2$ the only singularity in I is the pole in the first term at $E = 2\omega_k$. Eq. (6.3) can be used to replace the second term with an integral since it is free from singularities. The loop summation I can then be expressed as

$$I = I_1 + I_2 \tag{6.15}$$

where

$$I_1 = -i\frac{1}{L^3}\sum_{\vec{k}}\frac{f(\omega_k,\vec{k})}{2\omega_k((E-\omega_k)^2-\omega_k^2)} \tag{6.16}$$

and

$$I_2 = -i\int\frac{d^3k}{(2\pi)^3}\frac{f(E+\omega_k,\vec{k})}{2\omega_k((E+\omega_k)^2-\omega_k^2)}. \tag{6.17}$$

In order to implement the summation formula derived in the previous section, it is convenient to rewrite I_1 as follows:

$$I_1 = -i\frac{1}{L^3}\frac{1}{2E}\sum_{\vec{k}}\frac{f(k)}{q^2-k^2}\frac{E+2\omega_k}{4\omega_k}. \tag{6.18}$$

Direct application of Eq. (6.8) leads to

$$I_1 = -i\frac{1}{2E}\mathcal{P}\int\frac{d^3k}{(2\pi)^3}\frac{f(\vec{k})}{q^2-k^2}\frac{E+2\omega_k}{4\omega_k}-\frac{i}{2E}\sum_{l=0}^{\infty}\sum_{m=-l}^{l}f_{lm}(q)Z_{lm}(q^2). \tag{6.19}$$

The final step in deriving the finite volume correction to I is to rewrite the principal-value integral in terms of the corresponding integral with the Feynman $i\epsilon$ prescription in the propagator and a δ-function term:

$$\begin{aligned} I_1 = -i\frac{1}{2E}\int\frac{d^3k}{(2\pi)^3}\frac{f(\vec{k})}{q^2-k^2+i\epsilon}\frac{E+2\omega_k}{4\omega_k} \\ +\frac{qf_{00}(q)}{8\pi E}-\frac{i}{2E}\sum_{l=0}^{\infty}\sum_{m=-l}^{l}f_{lm}(q)Z_{lm}(q^2). \end{aligned} \tag{6.20}$$

The first line of Eq. (6.20) is exactly the infinite volume expression for I_1 in

Minkowski space, which leads to the final result

$$I = I_\infty + I_{FV} \tag{6.21}$$

$$I_{FV} = \left\{ \frac{q f_{00}(q)}{8\pi E} - \frac{i}{2E} \sum_{l=0}^{\infty} \sum_{m=-l}^{l} f_{lm}(q) Z_{lm}(q^2) \right\} \tag{6.22}$$

An important point to note is that q is a momentum determined by the energy E, and so it can take any positve value. In particular, q is not constrained by the finite volume. This will allow the finite volume corrections to be expressed in terms of physical scattering amplitudes.

Each of the loop summations in Fig. 6.1 can now be evaluated using Eq. (6.21), and the series reorganised. The correlation function $\tilde{C}(E)$ can be written in terms of an infinite volume correlator plus a finite volume correction

$$\tilde{C}(E) = \tilde{C}^\infty(E) + \tilde{C}^{FV}(E). \tag{6.23}$$

If I_∞ were to be kept in each loop in Fig. 6.1 then the infinite volume correlator $\tilde{C}^\infty(E)$ would be recovered. It follows that in order to work out the finite volume corrections, at least one insertion of I_{FV} must be included in the sum. The contributions to $\tilde{C}^{FV}(E)$ are depicted in Fig. 6.2.

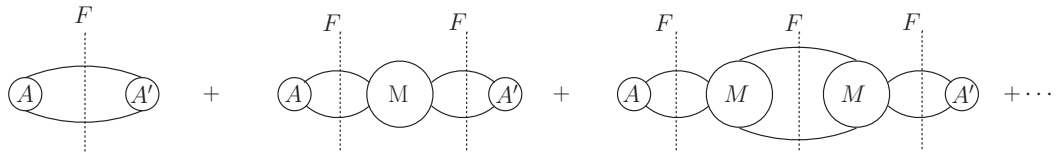

Figure 6.2: *Finite volume corrections to the two-pion correlator.*

An insertion of I_{FV} in Fig. 6.2 is denoted by the dashed line. The initial and final two-pion states, labelled A and A', are given by

$$A = {}_{\text{out}}\langle \pi\pi; E | \, \sigma^\dagger(\vec{0}, 0) \, |0\rangle \, Z_\pi \qquad A' = Z_\pi \, \langle 0 | \, \sigma(0, \vec{0}) \, | \pi\pi; E \rangle \tag{6.24}$$

and contain a geometric series of contributions with any number of insertions K with the intermediate loops containing the infinite volume integral I_∞. M is the

on-shell scattering amplitude, obtained by summing a similar geometric series, and F is a kinematic factor determined by the form of I_{FV}. After adding all the contributions in Fig. 6.2, the finite volume correction to the two-pion correlator is

$$\begin{aligned}\tilde{C}^{FV}(E) &= -A'FA + AF(iM/2)FA + \cdots \\ &= -A'F\frac{1}{1+iMF/2}A.\end{aligned} \tag{6.25}$$

The factor of $1/2$ is included because it is assumed that the two pions are identical. The quantity M can be rewritten in terms of partial waves, where δ_l will denote the phase shift in the l^{th} partial wave, as follows:

$$M_{l_1m_1;l_2;m_2} = \delta_{l_1l_2}\delta_{m_1m_2}\frac{16\pi E}{q}\frac{(\exp[2i\delta_{l_1}(q)]-1)}{2i}. \tag{6.26}$$

The form of F can be found by comparing directly with Eq. (6.22):

$$F_{l_1m_1;l_2;m_2} = \frac{q}{8\pi E}\left(\delta_{l_1l_2}\delta_{m_1m_2} + iF^{FV}_{l_1m_1;l_2;m_2}\right) \tag{6.27}$$

with

$$F^{FV}_{l_1m_1;l_2;m_2} = -\frac{4\pi}{q}\sum_{l=0}^{\infty}\sum_{m=-l}^{l}\frac{\sqrt{4\pi}}{q^l}Z_{lm}(q^2)\int d\Omega Y^*_{l_1,m_1}Y^*_{l,m}Y_{l_2,m_2}. \tag{6.28}$$

The arguments of the spherical harmonics are (θ,ϕ) and the asterixes on the spherical harmonics denote complex conjugation. The factor F will contain poles at energies corresponding to two free pions both having momenta allowed by the finite volume. Rescattering of the final state pions shifts the position of the poles in $\tilde{C}^{FV}(E)$ to energies determined by the condition that $1+iMF/2$ has zero eigenvalue. Equivalently the quantisation condition is

$$\det(1+iMF/2) = 0. \tag{6.29}$$

Eq. (6.29) demonstrates that the finite volume energy shifts depend on interactions only through the infinite volume scattering amplitude M, as was shown by Lüshcher in [53]. To make use of Eq. (6.29) the number of partial waves

contributing to the rescattering is restricted to be s-wave. The s-wave quantisation condition is then simply

$$1 + iMF/2 = 0 \tag{6.30}$$

with

$$M = \frac{16\pi E}{q}\frac{(e^{2i\delta(q)} - 1)}{2i}, \tag{6.31}$$

δ is the s-wave phase shift and

$$F = \frac{q}{8\pi E} - \frac{i}{2E}Z_{00}(q^2). \tag{6.32}$$

The quantisation condition can be rearranged to give

$$\tan[\delta(q)] = -\tan[\phi(q)] \quad \text{where} \quad \tan[\phi(q)] = \frac{q}{4\pi}[Z_{00}(q^2)]^{-1}. \tag{6.33}$$

This is equivalent to the usual form of the quantisation condition given in Eq. (6.1). A method for numerically determining the value of $Z_{00}(q^2)$ in Eq. (6.33) can be found in [55].

6.3 Relation between Finite Volume and Infinite Volume Matrix Elements

The two pion correlation function in a finite volume can be written as

$$\begin{aligned} C_\sigma^V(t) =& \int d^3x \, \langle 0| \, \sigma(\vec{x}, t)\sigma(\vec{0}, 0) \, |0\rangle_V \\ =& V \sum_n |\, \langle 0| \, \sigma(\vec{0}, 0) \, |\pi\pi, n\rangle_V \, |^2 e^{-E_n t} \\ \xrightarrow{V\to\infty}& V \int dE \rho_V(E) |\, \langle 0| \, \sigma(\vec{0}, 0) \, |\pi\pi\rangle_V \, |^2 e^{-Et}, \end{aligned} \tag{6.34}$$

where $\rho_V(E) = dn/dE$ describes the density of states. The corresponding infinite volume correlator is

$$C_\sigma^\infty(t) = \frac{1}{16\pi^2}\int dE \frac{q}{E} |\, \langle 0| \, \sigma(\vec{0}, 0) \, |\pi\pi, E\rangle_\infty \, |^2 e^{-iEt}. \tag{6.35}$$

Comparing Eq. (6.35) with Eq. (6.34),

$$|\pi\pi, E\rangle_\infty \leftrightarrow 4\pi\sqrt{\frac{VE\rho(q)}{q}}\,|0\rangle_V\,. \tag{6.36}$$

Similarly, the relation for a kaon state is

$$|K\rangle_\infty \leftrightarrow \sqrt{2EV}\,|K\rangle_V\,. \tag{6.37}$$

The quantisation condition in Eq. (6.1) allows the density of states in Eq. (6.34) to be evaluated:

$$\rho_V(E) = \frac{dn}{dE} = \frac{E}{4\pi q}\left\{\frac{\partial\delta}{\partial q} + \frac{\partial\phi}{\partial q}\right\}. \tag{6.38}$$

The main result of this chapter, relating the finite volume $K \to \pi\pi$ matrix element with the infinite volume $K \to \pi\pi$ matrix element is found by combining eqs. (6.36),(6.37) and (6.38):

$$|A|^2 = 8\pi V^2 \frac{m_K E^2}{q^2}\left\{\frac{\partial\delta}{\partial q} + \frac{\partial\phi}{\partial q}\right\}|M|^2 \tag{6.39}$$

where

$$A = {}_\infty\langle\pi\pi; E|\, H_W\, |K\rangle_\infty \tag{6.40}$$

and

$$M = {}_V\langle\pi\pi; E|\, H_W\, |K\rangle_V\,. \tag{6.41}$$

6.4 Finite Volume Corrections for Non-Interacting Pions

In this section the relation between finite volume matrix elements and infinite volume amplitudes is worked out for the simpler *free field* case, where the two final-state pions do not interact with each other.

The wavefunction for a single particle plane-wave state in a finite volume is

$$\psi_{\vec{p}}^{FV}(\vec{x}) = \frac{1}{L^{3/2}} e^{i\vec{p}.\vec{x}}. \tag{6.42}$$

In an infinite volume where the state has a relativistic normalisation, the equivalent wave function is

$$\psi_{\vec{p}}^{\infty}(\vec{x}) = \sqrt{2E}e^{i\vec{p}.\vec{x}}. \tag{6.43}$$

Thus for single-particle states, the relation between finite and infinite volume is

$$|p\rangle^{\infty} = \sqrt{2EL^3}\,|p\rangle^{FV}\,. \tag{6.44}$$

For a two-particle state occupied by identical pions, the finite volume wavefunction is

$$\psi_{\vec{p}_1\vec{p}_2}(\vec{x}_1,\vec{x}_2) = \begin{cases} \frac{1}{\sqrt{2}L^3}(e^{i\vec{p}_1.\vec{x}_1}e^{i\vec{p}_2.\vec{x}_2} + e^{i\vec{p}_1.\vec{x}_2}e^{i\vec{p}_2.\vec{x}_1}) & p_1 \neq p_2 \\ \\ \frac{1}{L^3}e^{i\vec{p}_1.(\vec{x}_1+\vec{x}_2)} & p_1 = p_2 \end{cases}. \tag{6.45}$$

The infinite volume wavefunction is

$$\psi_{\vec{p}_1\vec{p}_2}^{\inf}(\vec{x}_1\vec{x}_2) = \frac{1}{\sqrt{2}}\sqrt{2E_1}\sqrt{2E_2}(e^{i\vec{p}_1.\vec{x}_1}e^{i\vec{p}_2.\vec{x}_2} + e^{i\vec{p}_1.\vec{x}_2}e^{i\vec{p}_2.\vec{x}_1}) \tag{6.46}$$

which leads to the relation

$$|p_1,p_2\rangle^{\infty} = \begin{cases} \sqrt{2E_1}\sqrt{2E_2}L^3\,|p_1,p_2\rangle^{FV} & \vec{p}_1 \neq \vec{p}_2 \\ \\ \sqrt{2}\sqrt{2E_1}\sqrt{2E_2}L^3\,|p_1,p_2\rangle^{FV} & \vec{p}_1 = \vec{p}_2 \end{cases}. \tag{6.47}$$

The calculation of $K \to \pi\pi$ matrix elements in an isospin=0 final state will be performed at threshold where $\vec{p}_1 = \vec{p}_2 = 0$, in which case the relation between finite- and infinite-volume $K \to \pi\pi$ matrix elements is

$$\langle\pi(0)\pi(0)|\,\mathcal{L}_W\,|K(0)\rangle_{\infty} = 2(m_K L)^{3/2}\,\langle\pi(0)\pi(0)|\,H_W\,|K(0)\rangle_{FV}\,. \tag{6.48}$$

Chapter 7

Lattice Methods for $K \to \pi\pi$

Two separate calculations of the $K \to \pi\pi$ decay amplitudes are discussed in this thesis. The first calculation focusses on the amplitude A_2, and provides the first calculation of A_2 at nearly physical kinematics. The second calculation is performed with large quark masses on a relatively small lattice volume, allowing large statistics to be collected for the evaluation of A_0. The purpose of this chapter is to discuss the details of the technical aspects of the lattice evaluation of the $K \to \pi\pi$ correlation functions in general. Results from the two calculations will then be presented in Chapters 8 and 9.

An essential ingredient in the evaluation of the $K \to \pi\pi$ matrix elements is the two-pion correlation function. As such, this chapter begins with a discussion of two-pion scattering. Ensuring the two final state pions have non-zero momentum is a fundamental aspect of the evaluation of A_2, and a discussion of how this is achieved is given in Sec. 7.1. In Sec. 7.2, the correlation functions and Wick contractions relevant to the evaluation of the $K^+ \to \pi^+\pi^+$ matrix elements are given. Finally, the details of computing the $K^0 \to \pi\pi$ matrix elements at zero momentum are given in Sec. 7.3.

7.1 Two-Pion Scattering

For physical $K \to \pi\pi$ decays in the centre-of-mass (CM) frame, the final state pions will have non-zero momentum. If periodic boundary conditions are used on the quark fields, the allowed two-pion energies are approximately $2\sqrt{m_\pi^2 + (2\pi n/L)^2}$ where $n = 0, 1, 2, \ldots$. Thus extracting the two-pion state with energy $\simeq m_K$ requires both the careful tuning of the lattice volume and the fitting of the correlation function to an excited state. This entails extracting the next-to-leading exponential in the large time limit, which is difficult to perform with high accuracy.

However, for the $I = 2$ two-pion state a special choice of boundary condition can be applied to the quark fields in order to simulate the two final-state pions at non-zero momentum. This is made possible by the Wigner-Eckart theorem, which relates the $K^+ \to \pi^+\pi^0$ matrix element to the $K^+ \to \pi^+\pi^+$ matrix element according to Eq. (3.10). With anti-periodic boundary conditions in one or more spatial direction on one of the quark fields in each π^+-meson, the allowed pion momenta are $p = (n\pi/L)$, with $n = 1, 2, \ldots$, in each spatial direction where anti-periodic boundary conditions have been applied. The non-zero momentum pions are now the ground state, and so the correlation function can be fitted to the leading exponential.

The Wigner-Eckart theorem is necessary in order to successfully simulate the isospin=2 two-pion final state with the desired momentum. Using different boundary conditions for the up and down quarks breaks isospin, and would allow the final state pions to mix with the $I = 0$ two-pion state. However, the $\pi^+\pi^+$ final state is the only charge-2 state, and is protected from such mixing by charge conservation. The inability to use the Wigner-Eckart relation to circumvent the isospin breaking prevents the same trick from being used for the calculation of the $\Delta I = 1/2$ decay amplitude; this constitutes one of the major technical hurdles in this calculation.

The $\pi^+\pi^+$ correlation function is

$$C_{\pi^+\pi^+}(\vec{p}; t; t_\pi) = \langle 0 | \, O_{\pi^+\pi^+}(\vec{p}, t) O^{\cos\,\dagger}_{\pi^+\pi^+}(\vec{p}, t) \, |0\rangle \,, \tag{7.1}$$

where the interpolating operators are

$$O_{\pi^+\pi^+}(\vec{p},t) = \sum_{\vec{w}\vec{x}\vec{y}\vec{z}} e^{i\vec{p}\cdot\vec{w}} e^{-i\vec{p}\cdot\vec{y}}\, \overline{d}(\vec{w},t)\gamma^5 u(\vec{x},t)\overline{d}(\vec{y},t)\gamma^5 u(\vec{z},t) \tag{7.2a}$$

$$O^{\cos}_{\pi^+\pi^+}(\vec{p},t) = \sum_{\vec{w}\vec{x}\vec{y}\vec{z}} \eta_{\cos}(\vec{w};\vec{p})\eta_{\cos}(\vec{y};\vec{p})\, \overline{d}(\vec{w},t)\gamma^5 u(\vec{x},t)\overline{d}(\vec{y},t)\gamma^5 u(\vec{z},t). \tag{7.2b}$$

The d-quark is generated by imposing antiperiodic boundary conditions in one or more of the spatial directions and using Coulomb gauge-fixed momentum wall sources of the "cosine" type, defined in Eq. (4.51). The $I = 2$ two-pion correlation function at momentum $\vec{p}$ is calculated by evaluating

$$C_{\pi^+\pi^+}(\vec{p},t;t_\pi) = 2(D - C), \tag{7.3}$$

where D and C label two different Wick contractions. These Wick contractions are shown in Fig. 7.1 and the naming convention for the diagrams is taken from [56]. Inserting a complete set of two-pion states in Eq. (7.3), the expected form of the correlation function at large t is

$$\begin{aligned} C_{\pi\pi}(\vec{p};t;t_\pi) &= \langle 0|\, O_{\pi\pi}(\vec{p},t)\,|\pi\pi\rangle\, \langle\pi\pi|\, O^{\cos\,\dagger}_{\pi\pi}(\vec{p},t)\,|0\rangle\, e^{-E_{\pi\pi}t} + C \\ &\equiv Z^e_{\pi\pi}(Z^c_{\pi\pi})^* e^{-E_{\pi\pi}t} + C, \end{aligned} \tag{7.4}$$

where $Z^e_{\pi\pi} = \langle 0|\, O_{\pi\pi}(\vec{p},t)\,|\pi\pi\rangle$, $Z^c_{\pi\pi} = \langle 0|\, O^{\cos}_{\pi\pi}(\vec{p},t)\,|\pi\pi\rangle$, and the labels e and c have been introduced to distinguish between the use of an exponential momentum source or a cosine momentum source. The constant C is included to describe the leading "around-the-world" effect. This constant term arises from a contribution in the corresponding functional integral where each of $O^\dagger_{\pi^+\pi^+}$ and $O_{\pi^+\pi^+}$ annihilate one pion and create another, so that a single pion propagates across the entire lattice. This contribution to the correlation function is independent of t, and although it contains the small factor $e^{-E_\pi T}$, where T is the temporal size of the lattice, it may nevertheless lead to a loss of precision.

When studying the propagation of two π^+ mesons, the same cosine source is used for each d-quark, which introduces cross terms in correlation functions that couple

to two-pion states with non-zero total momentum. For illustration, consider the case $\vec{p} = (\pi/L, 0, 0)$ so that the product of the sources of the two d-quarks is

$$\begin{aligned}\eta_{\cos}(\vec{x}_1, \vec{p})\eta_{\cos}(\vec{x}_2, \vec{p}) &= \cos\left(\frac{\pi}{L}x_1\right)\cos\left(\frac{\pi}{L}x_2\right) \\ &= \frac{1}{4}\left(e^{i\frac{\pi}{L}x_1}e^{i\frac{\pi}{L}x_2} + e^{i\frac{\pi}{L}x_1}e^{-i\frac{\pi}{L}x_2} + e^{-i\frac{\pi}{L}x_1}e^{i\frac{\pi}{L}x_2} + e^{-i\frac{\pi}{L}x_1}e^{-i\frac{\pi}{L}x_2}\right).\end{aligned} \tag{7.5}$$

The two pions are required to have individual momenta $\vec{p}_1 = \frac{\pi}{L}\hat{\mathbf{x}}$ and $\vec{p}_2 = -\frac{\pi}{L}\hat{x}$ (or vice-versa), but the first and last terms on the right hand side of Eq. (7.5) couple to two-pion states with total momentum $2\frac{\pi}{L}$ and $-2\frac{\pi}{L}$ respectively. The unwanted terms in the two-pion correlation functions are eliminated by using different sinks, $\exp(\pm i\pi x_i/L)$, for the two d quarks ensuring that they carry equal and opposite momenta which constrains the final state to have zero total momentum. In the $K \to \pi\pi$ correlation functions, the kaon has zero momentum and the sum over the spatial position of the weak operator then ensures that the two-pion final state also has zero total momentum.

The advantage of using the cosine sources is that it halves the number of inversions which have to be performed for the d-quark. Had the more conventional momentum source,

$$\eta_{\vec{p}}(\vec{x}) = e^{i\vec{p}\cdot\vec{x}}, \tag{7.6}$$

been used, it would have been necessary to perform two separate d-quark inversions with momentum $+\vec{p}$ for one and $-\vec{p}$ for the other. The cosine source eliminates one of these inversions.

It was shown in [57] that it is sufficient to use the antiperiodic boundary conditions only on the valence down anti-quarks in the π^+ mesons, and to use periodic boundary conditions for the sea quarks used in the simulations. Thus it is only necessary to generate one lattice ensemble with periodic boundary conditions imposed on all sea quarks.

The calculation of the two-pion scattering in the $I = 0$ channel differes from the $I = 2$ channel in three key ways. Firstly there are two extra Wick contractions which contribute to the correlation function. These are shown in Fig. 7.1. Secondly,

there is a vacuum contribution which must be subtracted, and finally it is not possible with current techniques to simulate the two pions at non-zero momentum.

Two-pion states with $I = 0, 2$ and third component of isospin $I_z = 0$ are constructed from $|\pi^+\pi^-\rangle$ and $|\pi^0\pi^0\rangle$ states as described in Eqns. (2.2c) and (2.2d). The interpolating operators used to overlap with $|\pi^+\pi^-\rangle$ and $|\pi^0\pi^0\rangle$ states are

$$O_{\pi^+\pi^-}(t) = \sum_{\vec{w}\vec{x}\vec{y}\vec{z}} \overline{d}(\vec{w},t)\gamma^5 u(\vec{x},t)\overline{u}(\vec{y},t)\gamma^5 d(\vec{z},t) \tag{7.7a}$$

$$O_{\pi^0\pi^0}(t) = \frac{1}{\sqrt{2}} \sum_{\vec{w}\vec{x}\vec{y}\vec{z}} \left\{\overline{u}(\vec{w},t)\gamma^5 u(\vec{x},t) - \overline{d}(\vec{w},t)\gamma^5 d(\vec{x},t)\right\} \times \left\{\overline{u}(\vec{y},t)\gamma^5 u(\vec{z},t) - \overline{d}(\vec{y},t)\gamma^5 d(\vec{z},t)\right\}. \tag{7.7b}$$

At zero momentum, the $|\pi^+\pi^-\rangle$ state is identical to the $|\pi^-\pi^+\rangle$ state, and the two-pion correlation functions with $I_z = 0$ are calculated by evaluating

$$C_0^{\pi\pi}(t,t_\pi) \equiv \langle O_0^{\pi\pi}(t) O_0^{\pi\pi}(t_\pi)^\dagger\rangle = \tfrac{1}{3}\left\{4\left\langle O_{\pi^+\pi^-}(t) O^\dagger_{\pi^+\pi^-}(t_\pi)\right\rangle + 4\left\langle O_{\pi^+\pi^-}(t) O^\dagger_{\pi^0\pi^0}(t_\pi)\right\rangle + \left\langle O_{\pi^0\pi^0}(t) O^\dagger_{\pi^0\pi^0}(t_\pi)\right\rangle\right\} \tag{7.8a}$$

$$= 2D(t,t_\pi) + C(t,t_\pi) - 6R(t,t_\pi) + 3V(t,t_\pi) \tag{7.8b}$$

$$C_2^{\pi\pi}(t,t_\pi) \equiv \langle O_2^{\pi\pi}(t) O_2^{\pi\pi}(t_\pi)^\dagger\rangle = \tfrac{1}{3}\left\{2\left\langle O_{\pi^+\pi^-}(t) O^\dagger_{\pi^+\pi^-}(t_\pi)\right\rangle + 2\left\langle O_{\pi^+\pi^-}(t) O^\dagger_{\pi^0\pi^0}(t_\pi)\right\rangle + 4\left\langle O_{\pi^0\pi^0}(t) O^\dagger_{\pi^0\pi^0}(t_\pi)\right\rangle\right\} \tag{7.8c}$$

$$= 2\big(D(t,t') - C(t,t')\big) \tag{7.8d}$$

where D, C, R and V refer to the four different wick contractions which contribute to the two pion scattering [56]. For convenience, the minus sign arising from the number of fermion loops is not included in the definition of these contractions. The vacuum contraction, labelled V, should be accompanied by a vacuum subtraction. These contractions can be calculated in terms of the light quark propagator

$S^l(t_{\rm snk}, t_{\rm src})$ for a Coulomb gauge fixed wall source located at the time $t_{\rm src}$ and a similar wall sink located at $t_{\rm snk}$. The resulting complete vacuum amplitude, including the vacuum subtraction, is given by

$$\begin{aligned} V(t,t') &= \Big\{ \Big\langle \mathrm{Tr}[S^l(t',t')S^l(t',t')^\dagger]\mathrm{Tr}[S^l(t,t)S^l(t,t)^\dagger] \Big\rangle \\ &\quad - \Big\langle \mathrm{Tr}[S^l(t',t')S^l(t',t')^\dagger] \Big\rangle \Big\langle \mathrm{Tr}[S^l(t,t)S^l(t,t)^\dagger] \Big\rangle \Big\}, \end{aligned} \tag{7.9}$$

where the indicated traces are taken over spin and colour and the hermiticity properties of the domain wall propagator have been used to eliminate factors of γ^5. In order to improve statistics, the results from sources on each of the N_t time slices can be explicitly averaged (N_t is the temporal extent of the lattice), as follows

$$\begin{aligned} V(t) &= \frac{1}{N_t} \sum_{t'=0}^{N_t-1} V(t,t') \\ &= \Big\{ \Big\langle \mathrm{Tr}[S^l(t',t')S^l(t',t')^\dagger]\mathrm{Tr}[S^l(t+t',t+t')S^l(t+t',t+t')^\dagger] \Big\rangle \\ &\quad - \Big\langle \mathrm{Tr}[S^l(t',t')S^l(t',t')^\dagger] \Big\rangle \Big\langle \mathrm{Tr}[S^l(t+t',t+t')S^l(t+t',t+t')^\dagger] \Big\rangle \Big\}. \end{aligned} \tag{7.10}$$

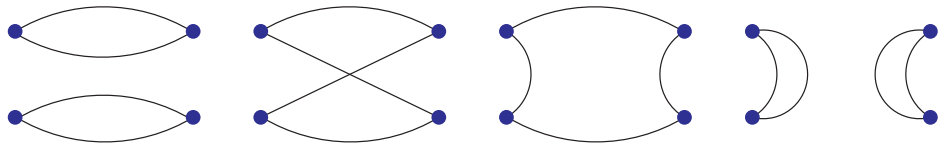

Figure 7.1: *The four diagrams which contribute to $\pi-\pi$ scattering*

Inserting a complete sets of two-pion states in Eqns. (7.8b) and (7.8d) the expected form of the two-pion correlation function at large t is

$$C_I^{\pi\pi}(t,0) = |Z_{\pi\pi,I}|^2 \left\{ \exp(-E_I^{\pi\pi} t) + \exp(-E_I^{\pi\pi}(T-t)) + A_I \right\}, \tag{7.11}$$

where $Z_{\pi\pi,I} = \langle 0| O_I^{\pi\pi} |\pi\pi\rangle$, and A_I describes the leading around-the-world contribution.

7.2 Expressions for $K^+ \to \pi^+\pi^+$ Correlation Functions

This section introduces the correlation functions and Wick contractions that must be computed in order to evaluate the $K^+ \to \pi^+\pi^+$ matrix elements at non-zero momentum. Discussion of the zero momentum calculation of the $K^0 \to \pi\pi$ matrix elements, with particular emphasis on the evaluation of A_0, are postponed until the next section. The main motivation for dividing the chapter in this way is the appearance of both disconnected and divergent diagrams in the $I = 0$ channel. In the case of the $I = 2$ final state no disconnected diagrams appear, there are no divergent eye diagrams, and isospin conservation requires that four valence quark propagators must join the kaon and weak operator with the operators creating the two final-state pions.

In addition to the two-pion correlation function discussed in Sec. 7.1, the correlation functions which were computed for this calculation of $K^+ \to \pi^+\pi^+$ are

$$C_\pi(t, t_\pi) = \langle 0| O_{\pi^+}(t) O^\dagger_{\pi^+}(t) |0\rangle \tag{7.12a}$$

$$C_K(t; t_K) = \langle 0| O_K(t) O^\dagger_K(t) |0\rangle \tag{7.12b}$$

$$C_{K\pi\pi}(\vec{p}; t_\pi; t_{op}; t_K) = \langle 0| O^{\cos}_{\pi\pi}(\vec{p}, t_\pi) Q_i(\vec{x}_{op}, t_{op}) O^\dagger_K(t_K) |0\rangle \tag{7.12c}$$

where the interpolating operators are

$$O_{\pi^+}(t) = \sum_{\vec{x},\vec{y}} \overline{d}(\vec{x}, t)\gamma^5 u(\vec{y}, t) \tag{7.13a}$$

$$O_K(t) = \sum_{\vec{x},\vec{y}} \overline{s}(\vec{x}, t)\gamma^5 u(\vec{y}, t) \tag{7.13b}$$

and $Q_i(\vec{x}_{op}, t_{op})$ is one of the operators defined in Eq. (3.12). Equation (7.12c) results in six Wick contractions, labelled $D^+_{L\chi,1}$, $D^+_{L\chi,2}$, $D^{\tilde{+}}_{LR,1}$ and $D^{\tilde{+}}_{LR,2}$, where $1, 2$ label the topology of the Wick contractions, $\chi = L, R$ depending on whether the operator is LL or LR, and the $\sim$ indicates that the operator is colour mixed. The

superscript + reminds the reader that these contractions are for $K^+ \to \pi^+\pi^+$. Full expressions for all six Wick contractions can be found in A.1. Quark-flow diagrams depicting the traces over spinor indices are presented in Fig. 7.2, where $\gamma_\chi = \gamma_L$ if the weak operator is in the (27,1) representation. Alternatively $\gamma_\chi = \gamma_R$ if the weak operator is in an (8,8) representation. The diagrams in Fig. 7.2 do not carry a minus sign for odd numbers of fermion traces. This minus sign is included explicitly in Eq. (7.14). The $K \to \pi\pi$ correlation function for each of the three operators in the $\Delta I = 3/2$ channel of the decay can then be written in terms of the diagrams $D^+_{L\chi,i}$, $\tilde{D^+_{LR,i}}$ (which are implicit functions of $\vec{p}$, t_π, t_{op} and t_K) as follows:

$$\begin{aligned} C^{(27,1)}_{K\to\pi\pi}(\vec{p};t_\pi;t_{op};t_K) &= 2(D^+_{LL,1} - D^+_{LL,2}) \\ C^{(8,8)}_{K\to\pi\pi}(\vec{p};t_\pi;t_{op};t_K) &= 2(D^+_{LR,1} - D^+_{LR,2}) \\ C^{(8,8)\mathrm{mx}}_{K\to\pi\pi}(\vec{p};t_\pi;t_{op};t_K) &= 2(\tilde{D^+_{LR,1}} - \tilde{D^+_{LR,2}}). \end{aligned} \tag{7.14}$$

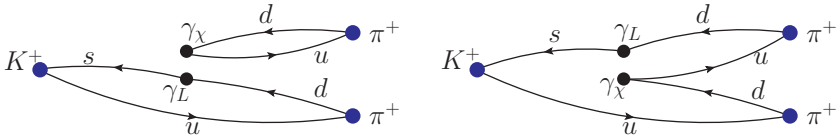

Figure 7.2: *$K^+ \to \pi^+\pi^+$ quark flow diagrams. The solid lines depict traces over spinor indices. The left-hand image is labelled $D^+_{L,\chi,1}$ and the right-hand image is labelled $D^+_{L,\chi,2}$.*

The pion and kaon masses and $K \to \pi\pi$ matrix elements can all be extracted from the correlation functions in Eq. (7.12). This is achieved by inserting complete sets of states between the operators as described in Eq. (4.56), with the result

$$\begin{aligned} C_\pi(t,t_\pi) &= |\langle 0|\, O_\pi(t)\,|\pi\rangle\,|^2(e^{-m_\pi t} + e^{-m_\pi(T-t)}) \\ &\equiv |Z_\pi|^2(e^{-m_\pi t} + e^{-m_\pi(T-t)}) \qquad (7.15a) \\ C_K(t;t_K) &= |\langle 0|\, O_K(t)\,|\pi\rangle\,|^2(e^{-m_K t} + e^{-m_K(T-t)}) \\ &\equiv |Z_K|^2(e^{-m_K t} + e^{-m_K(T-t)}) \qquad (7.15b) \\ C_{K\pi\pi}(\vec{p};t_\pi;t_{op};t_K) &= Z^c_{\pi\pi} Z_K \mathcal{M} e^{-m_K(t_K-t)} e^{-E_{\pi\pi}(t-t_\pi)} \qquad (7.15c) \end{aligned}$$

where $\mathcal{M}_i = \langle\pi\pi|\, Q_i(\vec{x}_{op},t_{op})\,|K\rangle$ and $Z^c_{\pi\pi}$ was defined in Sec. 7.1.

An analysis of these correlation functions, computed on an ensemble of large

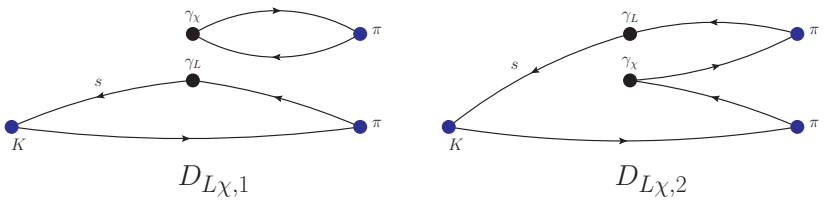

Figure 7.3: *Diagrams representing the eight $K^0 \to \pi\pi$ contractions of type*1*, where $\chi = L$ or R, and $\gamma_{L,R} = \gamma_\mu(1 \pm \gamma_5)$. The blue dot indicates a γ_5 matrix, which is present in each operator creating or destroying a pseudoscalar meson.*

$32^3 \times 64 \times 32$ lattices at almost physical kinematics is described in Chapter 8.

7.3 Wick Contractions for $K^0 \to \pi\pi$ Decays

In this section we describe some of the techniques used to evaluate the $K^0 \to \pi\pi$ matrix elements on the lattice. The calculation of A_0 requires evaluating the $K^0 \to \pi^+\pi^-$ and $K^0 \to \pi^0\pi^0$ matrix elements of all ten operators listed in Eq. (3.2). Particular emphasis must be placed on collecting large statistics. The $I = 0$ two-pion final state implies the presence of disconnected graphs in the correlation functions and makes the calculation very difficult. For these graphs, the noise does not decrease with increasing time separation between the source and sink, while the signal does. Therefore, substantial statistics are needed to get a clear signal. This difficulty is compounded by the presence of diagrams which diverge as $1/a^2$ as the continuum limit is approached (a is the lattice spacing). While these divergent amplitudes must vanish for a physical, on-shell decay they substantially degrade the signal to noise ratio even for an energy-conserving calculation such as the one presented in Chapter 9. Studying the properties of the $1/a^2$ terms and learning how to successfully subtract them is one of the important objectives of this calculation. Domain wall fermions are used in this calculation in order to preserve chiral symmetry, which is necessary to control operator mixing.

There are 48 different contractions which contribute to the matrix elements $\langle \pi\pi | Q_i | K^0 \rangle$. These are illustrated in Figs. 7.3-7.6.

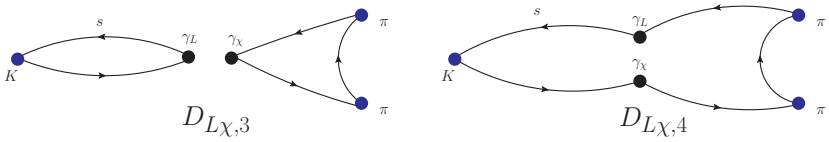

Figure 7.4: *Diagrams for the type2 $K^0 \to \pi\pi$ contractions.*

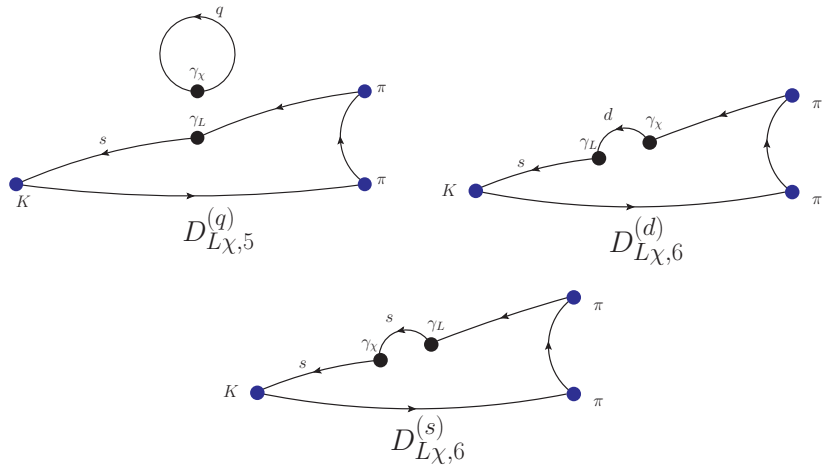

Figure 7.5: *Diagrams for the type3 $K^0 \to \pi\pi$ contractions.*

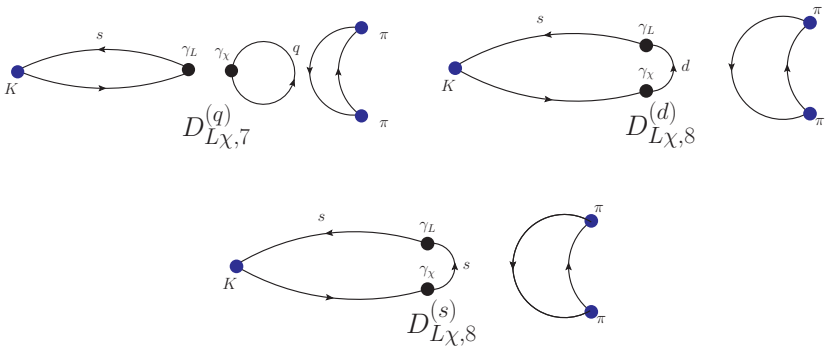

Figure 7.6: *Diagrams for the type4 $K^0 \to \pi\pi$ contractions.*

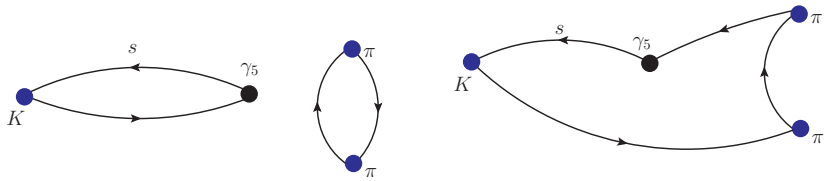

(a) mix3 (b) mix4

Figure 7.7: *Divergent diagrams*

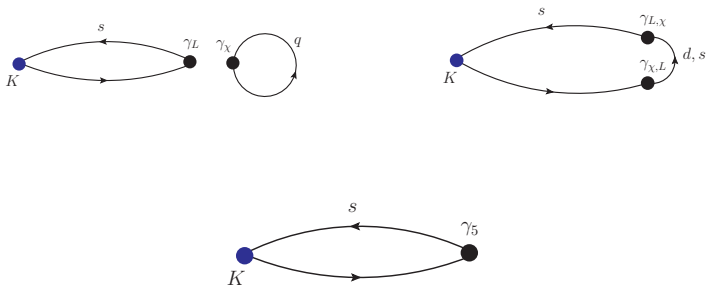

Figure 7.8: *Examples of $K \to |0\rangle$ contractions.*

These contractions are labeled in the figures and grouped into four categories labeled as *type*1, *type*2, *type*3, and *type*4 according to their topology. The labels are of the form $D_{L\chi,n}$ or $D^{(q)}_{L\chi,n}$, where n describes one of eight specific topologies, $\chi = L, R$ depending on whether the operator is LL or LR and the superscript (q) is sometimes included to specify which flavour of quark appears in certain diagrams. If the operator is colour diagonal, the quark-flows in Figs. 7.3-7.6 are traces over both spin and colour. If the operator is not colour-diagonal then the diagram is described as mixed. In this case separate traces over spin and colour appear in the expressions for the diagrams. The mixed diagrams are denoted by $\tilde{D}_{L\chi,n}$, $\tilde{D}^{(q)}_{L\chi,n}$ in place of $D_{L\chi,n}$ or $D^{(q)}_{L\chi,n}$. Once we have calculated all of these contractions, the correlation functions $\left\langle O_I^{\pi\pi}(t_\pi) Q_i(t_{\rm op}) K^0(t_K) \right\rangle$ are then obtained as combinations of these contractions. In order to simplify the following formulae, we use the amplitude $A_{I,i}(t_\pi, t, t_K)$ to represent three point function $\langle O_I^{\pi\pi}(t_\pi) Q_i(t_{\rm op}) K(t_K) \rangle$.

Using this notation, the $I = 2$ amplitudes can be written,

$$A_{2,1}(t_\pi, t_{\rm op}, t_K) = \sqrt{\frac{2}{3}}\{D_{LL,1} - D_{LL,2}\} \tag{7.16a}$$

$$A_{2,2}(t_\pi, t_{\rm op}, t_K) = \sqrt{\frac{2}{3}}\{\tilde{D}_{LL,1} - \tilde{D}_{LL,2}\} \tag{7.16b}$$

$$A_{2,3}(t_\pi, t_{\rm op}, t_K) = 0 \tag{7.16c}$$

$$A_{2,4}(t_\pi, t_{\rm op}, t_K) = 0 \tag{7.16d}$$

$$A_{2,5}(t_\pi, t_{\rm op}, t_K) = 0 \tag{7.16e}$$

$$A_{2,6}(t_\pi, t_{\rm op}, t_K) = 0 \tag{7.16f}$$

$$A_{2,7}(t_\pi, t_{\rm op}, t_K) = \sqrt{\frac{3}{2}}\{D_{LR,1} - D_{LR,2}\} \tag{7.16g}$$

$$A_{2,8}(t_\pi, t_{\rm op}, t_K) = \sqrt{\frac{3}{2}}\{\tilde{D}_{LR,1} - \tilde{D}_{LR.2}\} \tag{7.16h}$$

$$A_{2,9}(t_\pi, t_{\rm op}, t_K) = \sqrt{\frac{3}{2}}\{D_{LL,1} - D_{LL,2}\} \tag{7.16i}$$

$$A_{2,10}(t_\pi, t_{\rm op}, t_K) = \sqrt{\frac{3}{2}}\{\tilde{D}_{LL,1} - \tilde{D}_{LL,2}\} \tag{7.16j}$$

and in the I=0 case,

$$A_{0,1} = -\frac{1}{\sqrt{3}}\{D_{LL,1} + 2D_{LL,2} - 3D_{LL,3} - 3D^{(d)}_{LL,5} + 3D^{(d)}_{LL,7}\} \tag{7.17a}$$

$$A_{0,2} = \frac{1}{\sqrt{3}}\{2D_{LL,1} + D_{LL,2} - 3D_{LL,4} - 3D^{(d)}_{LL,6} + 3D^{(d)}_{LL,8}\} \tag{7.17b}$$

$$\begin{aligned} A_{0,3} = -\sqrt{3}\{&D_{LL,2} - 2D_{LL,3} + D_{LL,4} - 2D^{(d)}_{LL,5} - D^{(s)}_{LL,5} \\ &+ D^{(d)}_{LL,6} + D^{(s)}_{LL,6} + 2D^{(d)}_{LL,7} + D^{(s)}_{LL,7} - D^{(d)}_{LL,8} - D^{(s)}_{LL,8}\} \end{aligned} \tag{7.17c}$$

$$\begin{aligned} A_{0,4} = \sqrt{3}\{&D_{LL,1} + D_{LL,3} - 2D_{LL,4} + D^{(d)}_{LL,5} + D^{(s)}_{LL,5} \\ &- 2D^{(d)}_{LL,6} - D^{(s)}_{LL,6} - D^{(d)}_{LL,7} - D^{(s)}_{LL,7} + 2D^{(d)}_{LL,8} + D^{(s)}_{LL,8}\} \end{aligned} \tag{7.17d}$$

$$\begin{aligned} A_{0,5} = -\sqrt{3}\{&D_{LR,2} - 2D_{LR.3} + D_{LR,4} - 2D^{(d)}_{LR,5} - D^{(s)}_{LR,5} + D^{(d)}_{LR,6} \\ &+ D^{(s)}_{LR,6} + 2D^{(d)}_{LR,7} + D^{(s)}_{LR,7} - D^{(d)}_{LR,8} - D^{(s)}_{LR,8}\} \end{aligned} \tag{7.17e}$$

$$\begin{aligned} A_{0,6} = -\sqrt{3}\{&\tilde{D}_{LR,2} - 2\tilde{D}_{LR.3} + \tilde{D}_{LR,4} - 2\tilde{D}^{(d)}_{LR,5} - \tilde{D}^{(s)}_{LR,5} + \tilde{D}^{(d)}_{LR,6} \\ &+ \tilde{D}^{(s)}_{LR,6} + 2\tilde{D}^{(d)}_{LR,7} + \tilde{D}^{(s)}_{LR,7} - \tilde{D}^{(d)}_{LR,8} - \tilde{D}^{(s)}_{LR,8}\} \end{aligned} \tag{7.17f}$$

$$\begin{aligned} A_{0,7} = -\frac{\sqrt{3}}{2}\{&D_{LR,1} + D_{LR,2} - D_{LR,3} - D_{LR,4} - D^{(d)}_{LR,5} + D^{(s)}_{LR,5} - D^{(d)}_{LR,6} \\ &- D^{(s)}_{LR,6} + D^{(d)}_{LR,7} - D^{(s)}_{LR,7} + D^{(d)}_{LR,8} + D^{(s)}_{LR,8}\} \end{aligned} \tag{7.17g}$$

$$\begin{aligned} A_{0,8} = -\frac{\sqrt{3}}{2}\{&\tilde{D}_{LR,1} + \tilde{D}_{LR,2} - \tilde{D}_{LR,3} - \tilde{D}_{LR,4} - \tilde{D}^{(d)}_{LR,5} + \tilde{D}^{(s)}_{LR,5} - \tilde{D}^{(d)}_{LR,6} \\ &- \tilde{D}^{(s)}_{LR,6} + \tilde{D}^{(d)}_{LR,7} - \tilde{D}^{(s)}_{LR,7} + \tilde{D}^{(d)}_{LR,8} + \tilde{D}^{(s)}_{LR,8}\} \end{aligned} \tag{7.17h}$$

$$A_{0,9} = -\frac{\sqrt{3}}{2}\{D_{LL,1} + D_{LL,2} - D_{LL,3} - D_{LL,4} - D^{(d)}_{LL,5} + D^{(s)}_{LL,5} - D^{(d)}_{LL,6} - D^{(s)}_{LL,6} + D^{(d)}_{LL,7} - D^{(s)}_{LL,7} + D^{(d)}_{LL,8} + D^{(s)}_{LL,8}\} \tag{7.17i}$$

$$A_{0,10} = -\frac{\sqrt{3}}{2}\{D_{LL,1} + D_{LL,2} - D_{LL,3} - D_{LL,4} - D^{(d)}_{LL,5} - D^{(s)}_{LL,5} - D^{(d)}_{LL,6} + D^{(s)}_{LL,6} + D^{(d)}_{LL,7} + D^{(s)}_{LL,7} + D^{(d)}_{LL,8} - D^{(s)}_{LL,8}\}. \tag{7.17j}$$

The contractions identified in Figs. 7.3 - 7.6 do not carry the minus sign required when there is an odd number of fermion loops. Instead, the signs are included explicitly in Eqns. (7.16) and (7.17). A line represents a light quark propagator unless it is explicitly labeled. In general, up and down quarks and particular flavors of pion are not distinguished in Figs. 7.3 - 7.6. The exception is that occasionally down-quarks are labelled explicitly when two diagrams differ only by an insertion of a d/s quark and we wish to distinguish between them. These specific contractions of strange and light quark propagators are combined in Eqns. (7.16) and (7.17) to give the $I = 2$ and $I = 0$ amplitudes directly. Using Fierz symmetry, it can be shown that there are 12 identities among these contractions:

$$\begin{aligned}
D_{LL,1} &= -\tilde{D}_{LL,2}, \quad D^{(d)}_{LL,5} = -\tilde{D}^{(d)}_{LL,6}, \quad D^{(d)}_{LL,7} = -\tilde{D}^{(d)}_{LL,8} \\
D_{LL,2} &= -\tilde{D}_{LL,1}, \quad D^{(d)}_{LL,6} = -\tilde{D}^{(d)}_{LL,5}, \quad D^{(d)}_{LL,8} = -\tilde{D}^{(d)}_{LL,7} \\
D_{LL,3} &= -\tilde{D}_{LL,4}, \quad D^{(s)}_{LL,5} = -\tilde{D}^{(s)}_{LL,6}, \quad D^{(s)}_{LL,7} = -\tilde{D}^{(s)}_{LL,8} \\
D_{LL,4} &= -\tilde{D}_{LL,3}, \quad D^{(s)}_{LL,6} = -\tilde{D}^{(s)}_{LL,5}, \quad D^{(s)}_{LL,8} = -\tilde{D}^{(s)}_{LL,7}
\end{aligned} \tag{7.18}$$

A consequence of these identities is that Eq. (7.17) is consistent with only seven of

the ten operators Q_i being linearly independent and with the three usual relations:

$$Q_{10} - Q_9 = Q_4 - Q_3 \tag{7.19a}$$

$$Q_4 - Q_3 = Q_2 - Q_1 \tag{7.19b}$$

$$2Q_9 = 3Q_1 - Q_3. \tag{7.19c}$$

The loop contractions of *type*3 and *type*4 are calculated using the Gaussian, stochastic wall sources described in Sec. 9.1.

In order to make the approach more explicit, some examples are included. First consider the two contractions of *type*1 identified as $D_{LL,1}$ and $\tilde{D}_{LL,1}$, both depicted by the left-most diagram in Fig. 7.3:

$$\begin{aligned} D_{LL,1} &= \Big\langle \mathrm{Tr}\left\{\gamma_\mu(1-\gamma_5)S^l(\vec{x}_{op},t_{op};t_\pi)S^l(\vec{x}_{op},t_{op};t_\pi)^\dagger\right\} \times \\ &\qquad \mathrm{Tr}\Big\{\gamma^\mu(1-\gamma_5)S^l(\vec{x}_{op},t_{op};t_\pi)\gamma^5 S^l(t_\pi;t_K)S^s(\vec{x}_{op},t_{op};t_K)^\dagger\Big\}\Big\rangle \end{aligned} \tag{7.20}$$

$$\begin{aligned} \tilde{D}_{LL,1} &= \Big\langle \mathrm{Tr}_c\Big[\mathrm{Tr}_s\Big\{\gamma_\mu(1-\gamma_5)S^l(\vec{x}_{op},t_{op};t_\pi)\ S^l(\vec{x}_{op},t_{op};t_\pi)^\dagger\Big\} \\ &\qquad \times \mathrm{Tr}_s\Big\{\gamma^\mu(1-\gamma_5)S^l(\vec{x}_{op},t_{op};t_\pi)\gamma_5 S^l(t_\pi;t_K)S^s(\vec{x}_{op},t_{op};t_K)^\dagger\Big\}\Big]\Big\rangle, \end{aligned} \tag{7.21}$$

where t_K is the time of the kaon wall source, t_π the time at which the two pions are absorbed and $x_{op} = (\vec{x}_{op}, t_{op})$ the location of the weak operator. The angle-brackets $\langle\cdots\rangle$ denote an average over configurations. The wall-source propagators were defined in Eq. (4.49). Each propagator is a 12×12 spin-colour matrix. The hermitian conjugation operation, †, operates on these 12×12 matrices. Traces over spinor indices are denoted Tr_s, traces over colour indices are denoted Tr_c, and traces over both spinor and colour indices are denoted Tr. The γ^5 hermiticity of the quark propagators is used to realise the combination of quark propagators given in Eqns. (A.5) and (7.21), allowing both contractions to be constructed from light and strange propagators computed using Coulomb gauge fixed wall sources located only at the times t_π and t_K. The spatial location, $\vec{x}_{op}$, of the weak operator is summed over to project onto zero spatial momentum and improve statistics.

As a third example, which illustrates the use of stochastic wall sources, consider contraction $D^{(l)}_{LR,5}$ shown in Fig. 7.5. Using the notation introduced above, this contraction is given by

$$\begin{aligned} D^{(l)}_{LR,5} = \Big\langle \mathrm{Tr}\left\{\gamma_\mu(1+\gamma_5) S^l_R(\vec{x}_{\mathrm{op}}, t_{\mathrm{op}}; t_{\mathrm{op}})\right\} \eta(x_{\mathrm{op}})^* \times \\ \mathrm{Tr}\Big\{\gamma^\mu(1-\gamma_5) S^l(\vec{x}_{\mathrm{op}}, t_{op}; t_\pi) S^l(t_\pi; t_\pi)^\dagger S^l(t_\pi, t_K) S^s(\vec{x}_{\mathrm{op}}, t_{op}; t_K)^\dagger\Big\}\Big\rangle . \end{aligned} \tag{7.22}$$

Here $\eta(x)$ is the value of the complex, Gaussian random wall source at the space-time position x, while $S^l_R(x_{\mathrm{sink}}, t_{\mathrm{src}})$ is the propagator whose source is $\eta(x)\delta(x_0 - t_{\mathrm{src}})$. The Dirac delta function $\delta(x_0 - t_{\mathrm{src}})$ restricts the source to the time plane $t = t_{\mathrm{src}}$. In the usual way, the average over the random source $\eta(\vec{x})$ which accompanies the configuration average, will set to zero all terms in which the source and sink positions for the propagator $S^l_R(x_{\mathrm{op}}, t_{\mathrm{op}})$ in Eq. (7.22) differ, giving us the contraction implied by the closed loop in the top left panel of Fig. 7.5. By using N_t separate propagators each with a random source non-zero on only one of the N_t time slices, the results obtained better statistical accuracy than would result from a single random source spread over all times.

All of the remaining expressions for the $K \to \pi\pi$ contractions are collected in section A.2 of the appendix.

7.3.1 Divergent Diagrams

An important objective of this calculation is to learn how to accurately evaluate the quark loop integration that is present in *type*3 and *type*4 graphs and which contains a $1/a^2$, quadratically divergent component. As can be recognised from the structure of the diagrams, these divergent terms can be interpreted as arising from the mixing between the dimension-six operators Q_i (for all i but 7 and 8) and a dimension-3 "mass" operator of the form $\overline{s}\gamma_5 d$. Such divergent terms are expected and do not represent a breakdown of the standard effective Hamiltonian written in Eq. (3.1). In fact, given the good chiral symmetry of domain wall fermions all other operators with dimension less than six which might potentially mix with those in Eq. (3.1) will vanish if the equations of motion are imposed. Therefore these

operators cannot contribute to the Green's functions evaluated in Eqns. (7.16) and (7.17) where the operators in H_W are separated in space-time from those operators creating the K meson and destroying the π mesons, a circumstance in which the equations of motion can be applied.

The problematic operator $\overline{s}\gamma_5 d$ is not explictly removed from the effective Hamiltonian because, again using the equations of motion, $\overline{s}\gamma_5 d$ can be written as the divergence of an axial current and hence will vanish in the physical case where the weak operator H_W carries no four-momentum and is evaluated between on-shell states. While we can explicitly sum the effective Hamiltonian density $\mathcal{H}_W$ over space to ensure H_W carries no spatial momentum, to ensure that no energy is transferred we must arrange that the kaon mass and two-pion energy are equal. We may achieve this condition, at least approximately, but there will be contributions from heavier states, which are normally exponentially suppressed, but which will violate energy conservation and hence will be enhanced by this divergent $\overline{s}\gamma_5 d$ term.

Since $\overline{s}\gamma_5 d$ will not contribute to the physical, energy-conserving $K \to \pi\pi$ amplitude, there is no theoretical requirement that it be removed. The coefficient of this $\overline{s}\gamma_5 d$ piece is both regulator dependent and irrelevant. The contribution of these terms in a lattice calculation of $K \to \pi\pi$ decay amplitudes will ultimately vanish as the equality of the initial and final energies is made more precise and as increased time separations are achieved. However, the unphysical effects of this $\overline{s}\gamma_5 d$ mixing are much more easily suppressed by reducing the size of this irrelevant term than by dramatically increasing the lattice size and collecting the substantially increased statistics required to work at large time separations. Furthermore, the condition imposed in Eq. (7.23) automatically subtracts the vacuum contribution from the type4 diagrams, so there is no need to make an explicit vacuum subtraction in the type4 diagrams once this $\overline{s}\gamma_5 d$ piece has been subtracted.

A direct way to remove this $1/a^2$ enhancement is to explicitly subtract an $\alpha_i \overline{s}\gamma_5 d$ term from each of the relevant operators Q_i where the coefficient α_i can be fixed by imposing the condition:

$$\langle 0|Q_i - \alpha_i \overline{s}\gamma_5 d|K\rangle = 0. \tag{7.23}$$

The $K \to$ vacuum matrix elements, $\langle 0|Q_i|K\rangle$ and $\langle 0|\overline{s}\gamma_5 d|K\rangle$ are constructed from the Wick contractions depicted in the top and bottom lines of Fig. 7.8 respectively. Of course, the arbitrary condition in Eq. (7.23) will leave a finite, regulator-dependent $\overline{s}\gamma_5 d$ piece behind in the subtracted operator $Q_i - \alpha_i \overline{s}\gamma_5 d$. However, this unphysical piece will not contribute to the energy-conserving amplitude being evaluated. Since it is no longer $1/a^2$-enhanced its effects on our calculation will be similar to those of the many other energy non-conserving terms which we must suppress by choosing equal energy K and $\pi\pi$ states and using sufficient large time separation to suppress the contributions of excited states.

Following Eq. (7.23) we will choose the coefficient α_i from the ratio

$$\alpha_i = \frac{\langle 0|Q_i|K^0\rangle}{\langle 0|\overline{s}\gamma_5 d|K^0\rangle}. \tag{7.24}$$

(Note, with this definition the coefficient α_i is proportional to the difference of the strange and light quark masses.) Thus, we will improve the accuracy when calculating graphs of *type*3 and *type*4 by including an explicit subtraction term for those operators Q_i where mixing with $\overline{s}\gamma_5 d$ is permitted by the symmetries (all but Q_7 and Q_8):

$$\begin{aligned}\left\langle O_0^{\pi\pi}(t_\pi) Q_i(t_{\rm op}) K^0(t_K)\right\rangle_{sub} = &\left\langle O_0^{\pi\pi}(t_\pi) Q_i(t_{\rm op}) K^0(t_K)\right\rangle \\ &- \alpha_i \left\langle O_0^{\pi\pi}(t_\pi) \overline{s}\gamma_5 d(t_{\rm op}) K^0(t_K)\right\rangle .\end{aligned} \tag{7.25}$$

We should recognise that there is a second, divergent, parity-even operator $\overline{s}d$ which mixes with our operators Q_i. However, we choose to neglect this effect because parity symmetry prevents it from contributing to either the $K \to \pi\pi$ or $K \to |0\rangle$ correlation functions being evaluated here.

The correlator $\left\langle O_0^{\pi\pi}(t_\pi)\overline{s}\gamma_5 d(t_{\rm op}) K^0(t_K)\right\rangle$ includes two contractions, one connected and one disconnected as shown in Fig. 7.7. These terms, which arise from the mixing of the operators Q_i with $\overline{s}\gamma_5 d$, are labeled $mix3$ and $mix4$. To better visualize the contributions from different types of contractions, we can write the

right hand side of Eq. (7.25) symbolically as

$$\begin{aligned} & type1 + type2 + type3 + type4 - \alpha \cdot (mix3 + mix4) \\ = \quad & type1 + type2 + sub3 + sub4, \end{aligned} \tag{7.26}$$

where $sub3 = type3 - \alpha \cdot mix3$ and $sub4 = type4 - \alpha \cdot mix4$. Note, here and in later discussions we refer to the term being subtracted as "mix" and the final difference as the subtracted amplitude "sub".

This completes the technical background to the $K^0 \to \pi\pi$ calculation. Details of a full analysis performed on an ensemble of $16^3 \times 32$ lattices with heavy pion masses can be found in Chapter 9.

Chapter 8

Evaluation of $K \to \pi\pi$ decay amplitudes on DSDR lattices

This chapter details the calculation of the $\Delta I = 3/2$ $K \to \pi\pi$ decay amplitude with nearly-physical kinematics. The results presented in this chapter are the first realistic ab-initio calculation of the decay amplitdue A_2, and form the main results of this thesis. The analysis of this chapter is perfomed on a single ensemble of $2+1$ flavour domain wall fermions with the DSDR-Iwasaki (IDSDR) gauge action at $\beta = 1.75$ and a lattice size of $32^3 \times 64 \times 32$. The residual mass is $am_{\text{res}} = 0.001843(8)$ [58]. The ensemble was generated with a simulated strange-quark mass of $am_h = 0.045$ and light-quark mass of $am_l = 0.001$, with corresponding unitary pion mass of approximately 170 MeV. The inverse lattice spacing has been determined to be $a^{-1} = 1.364(9)$ GeV [58], using the Ω baryon mass to set the scale and the masses of the pion and kaon to determine the physical quark masses.

The lattice spacing and two physical quark masses m_{ud} and m_s were obtained using a combined analysis of the IDSDR ensemble described above, along with a second IDSDR ensemble generated with $am_l = 0.0042$ also at $\beta = 1.75$ and the $32^3 \times 64 \times 16$ and $24^3 \times 64 \times 16$ domain wall fermion configurations with the Iwasaki gauge action at $\beta = 2.25$ and $\beta = 2.13$ respectively. The two Iwasaki ensembles were introduced in Chapter 5, and the properties of all the ensembles

used in this chapter are summarised in Table 9.1. This involves a combined fit of the pion and kaon masses and decay constants and the mass of the Ω-baryon as functions of the quark masses and lattice spacing. Three different ansätze were used for the quark-mass dependence in order to estimate the systematic error on the chiral extrapolations. Two of these are obtained from next-to-leading order (NLO) partially-quenched chiral perturbation theory with and without finite-volume corrections, and the third assumes a simple linear mass dependence (labelled *analytic* in the following). Following the analysis [51] of the two Iwasaki lattices, the extrapolation to the continuum limit is made along a family of scaling trajectories (lines of constant physics) that are defined by constant values of m_π, m_K and m_Ω; i.e. by imposing the condition that these masses have no lattice cutoff dependence on the scaling trajectory. The leading dependence on a of the remaining quantities is expected to be $O(a^2)$ and the fits assume such a quadratic dependence. Note that the coefficients of the a^2 terms are not constrained to be equal for the two different lattice actions. From the combined chiral and continuum fits the lattice spacings and physical quark masses required for the pion, kaon and Ω masses to match their physical values are determined, obtaining for the IDSDR ensembles an inverse-lattice spacing of $a^{-1} = 1.364(9)\,\text{GeV}$ and dimensionless physical quark masses of $\tilde{m}_l = 0.00178(3)$ and $\tilde{m}_s = 0.0490(6)$, which correspond to 3.09 ± 0.11 and $84.1 \pm 2.0\,\text{MeV}$ respectively when expressed in physical units in the $\overline{\text{MS}}$ scheme at 3 GeV. Here $\tilde{m} = m + m_{\text{res}}$ and the quoted errors contain both statistical and systematic contributions estimated using the procedures developed in ref. [51]. Note that the value for $\tilde{m}_l$ that would correspond to a physical pion mass is actually smaller than m_{res}, indicating that the chiral symmetry must be improved before physical pion masses can be simulated.

In order to correctly propagate the correlations between the data used in the determination of the lattice spacing with that of the present calculation of the $K \to \pi\pi$ matrix elements the super-jackknife method is used.

Measurements are made on a total of 146 gauge configurations, each separated by 8 molecular dynamics time units. With the aim of reducing the correlations between successive measurements, the gauge fields are shifted by 16 lattice spacings in the

Table 8.1: *Ensemble details. The main analysis of this chapter is performed using the IDSDR enemble with $m_l = 0.001$. The additional ensembles listed in this table are used in the determination of the IDSDR lattice spacing and physical quark masses.*

Lattice	β	am_h	am_l	number of trajectories
IDSDR ($32^3 \times 64$)	1.75	0.045	0.001	146
	1.75	0.045	0.0042	148
Iwasaki ($32^3 \times 64$)	2.25	0.03	0.004	300
	2.25	0.03	0.006	312
	2.25	0.03	0.008	252
Iwasaki ($24^3 \times 64$)	2.13	0.04	0.005	202
	2.13	0.04	0.01	178

time direction relative to the previous configuration prior to measuring the quark propagators.

The d-quark propagators are computed with antiperiodic boundary conditions in either 0 or 2 spatial directions, corresponding to pions with ground-state momenta $|\vec{p}| = 0$ and $|\vec{p}| = \sqrt{2}\pi/L$. This choice is motivated by the expectation that, with the simulated quark masses, $|\vec{p}| = \sqrt{2}\pi/L$ corresponds to on-shell kinematics, i.e. that the energy of the two-pion state is (almost) equal to m_K. Gauge fixed wall sources are used for the case $p = 0$, while cosine wall sources are used when the d-quark has non-zero momentum. The u and s quarks are generated with periodic spatial boundary conditions and Coulomb gauge-fixed wall sources.

Quark propagators with periodic and antiperiodic boundary conditions in the time direction were computed on each configuration with a source at $t = 0$. They were then combined so as to effectively double the time extent of the lattice. Meson correlation functions formed using the sum of the propagators with periodic and antiperiodic boundary conditions can be interpreted as containing forward propagating mesons originating at time $t = 0$, whereas those calculated with the difference can be interpreted as containing backward propagating mesons originating from a source at $t = 64$. The purpose of this procedure is to suppress the around the world effects. The leading around the world effects in two-pion and $K \to \pi\pi$ correlation functions have been described in previous chapters. Strange-quark propagators with periodic + antiperiodic combinations were generated with sources at $t_K = 20$, 24, 28, 32, 36, 40 and 44 in order to calculate

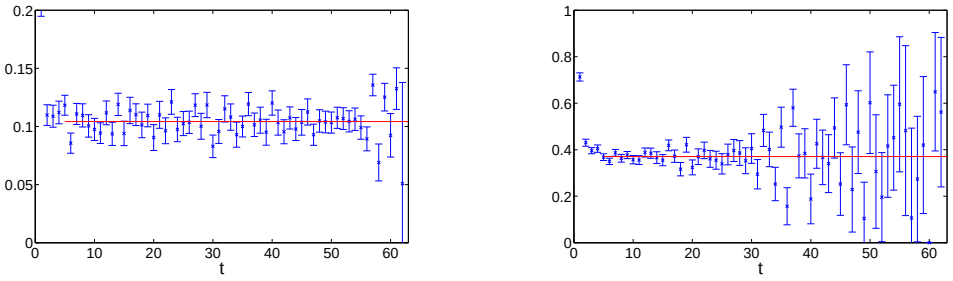

(a) Effective mass plot for the pion

(b) Effective mass plot for the kaon

Figure 8.1: *Effective mass plots for the pion and kaon. Results for m_π and m_K obtained from the fits of the correlation functions to Eqns. (7.15a,7.15b) are shown as the horizontal lines in each plot.*

$K \to \pi\pi$ correlation functions with kaon sources at these times, while the two-pion sources remained at either $t = 0$ or $t = 64$. Thus it was possible to achieve time separations between the kaon and two pions of 20, 24, 28 and 32 lattice time units in two different ways which increased the statistics. These separations were chosen so that the signals from the kaon and two pions did not decay into noise before reaching the four-quark operator Q_i.

8.1 Analysis

Results from the analysis of the correlation functions described in Chapter 7, computed on the IDSDR lattices, are presented in this section. While the results presented in Eq. (8.11) towards the end of this section contain estimates of the uncertainties, detailed discussion of the determination of the systematic errors is postponed until Sec. 8.3.

The pion and kaon two-point correlation functions at zero momentum are fit to the form given in Eqns. (7.15a) and (7.15b), with $T = 128$ being the total effective time extent of the lattice.

For both the pion and kaon, results for m_π, m_K, Z_π, and Z_K are obtained by fitting between $t = 5$ and $t = 63$. The masses extracted from these fits are superimposed on the effective mass plots in Figs. 8.1(a) and 8.1(b), and the numerical results are given in Tab. 8.2.

Table 8.2: *Results for meson masses and energies. The subscripts 0, 2 denote $p = 0$ and $p = \sqrt{2}\pi/L$ respectively, where $p = |\vec{p}|$.*

units	m_π	m_K	$E_{\pi,2}$	$E_{\pi\pi,0}$	$E_{\pi\pi,2}$	$m_K - E_{\pi\pi,2}$
lattice	0.10421(22)	0.37066(68)	0.17386(91)	0.21002(43)	0.3560(23)	0.0146(23)
MeV	142.11(94)	505.5(3.4)	237.1(1.8)	286.4(1.9)	485.5(4.2)	20.0(3.1)

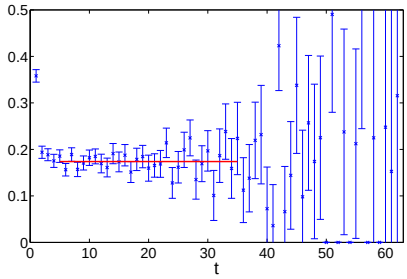

Figure 8.2: *Effective energy plot for a pion with momentum $p = \sqrt{2}\pi/L$. The horizontal line corresponds to value of E_π obtained from a fit to Eq. (8.1).*

The pions in the final state for $K \to \pi\pi$ decays have momentum $|\vec{p}| = \sqrt{2}\,\pi/L$ and in Fig. 8.2 the effective energy for a pion with this momentum is plotted. Since the correlation functions become noisier when the pion has a non-zero momentum, the fit is over the time interval $t = [5, 35]$ where the contribution from the backward propagating pion can be ignored. The fit form is

$$C_\pi(t, p = \sqrt{2}\pi/L) = |Z_\pi(p = \sqrt{2}\pi/L)|^2 e^{-E_\pi t}\,, \tag{8.1}$$

where $p = |\vec{p}|$ and E_π is the corresponding energy. The value $E_{\pi,2} = 0.17386(91)$ obtained from the fit (see Tab. 8.2) is nicely consistent with the (continuum) dispersion relation for a pion with mass 0.10421(22). The subscript 2 in $E_{\pi,2}$ indicates that the momentum of the pion is $\sqrt{2}\pi/L$, i.e. that anti-periodic boundary conditions have been imposed on the d quark in two directions.

The expected behaviour of the two-pion correlation functions is described in Eq. (7.4). The effects of pions propagating around the world are expected to be small after doubling the effective time extent of the lattice. An effective technique to reduce the statistical errors in the fit to the two-pion correlation function is to calculate the quotient of two-pion and single-pion correlators and fit the ratio to the

form

$$\frac{C_{\pi\pi}(t)}{(C_\pi(t))^2} \simeq R^2 e^{-\Delta E\, t}\,, \tag{8.2}$$

where $\Delta E = (E_{\pi\pi} - 2E_\pi)$ and $R^2 = \frac{|Z_{\pi\pi,e}|^2}{2^{n_{\rm tw}}|Z_\pi|^4}$. The energy difference ΔE is not equal to zero because of the repulsive interaction between the two pions with isospin 2 in a finite volume. The two-pion energy $E_{\pi\pi}$ is then given by $E_{\pi\pi} = \Delta E + 2E_\pi$, and $Z_{\pi\pi,e}$ is found from

$$Z_{\pi\pi,e} = (2^{\frac{n_{\rm tw}}{2}}) Z_\pi^2 R\,. \tag{8.3}$$

Eq. (8.2) can be used for values of t which are sufficiently large to neglect excited states and sufficiently smaller than $T/2$ so that the backward propagating states (and the around-the-world effects) can also be neglected. In practice, in order to improve the statistical precision, the correlation functions are *folded*, averaging the equivalent results at t and $T - t$. The ratio in Eq. (8.2) is calculated for $p = 0$, in which case Z_π and E_π are just the normalisation factor and pion mass found from the fit to Eq. (7.15a) and for $p = \sqrt{2}\pi/L$ in which case Z_π and E_π are taken from the fit to Eq. (8.1). The fit regions for the quotients are $t = [5, 48]$ for $p = 0$ and $[5, 22]$ for $p = \sqrt{2}\pi/L$. Plots of the quotients at the two values of p are shown in Fig. 8.3. The results for all the meson masses and energies are presented in Tab. 8.2. The difference between the kaon mass and two-pion energy, $m_K - E_{\pi\pi}$, is also calculated to demonstrate that the kinematics are close to being energy conserving.

The momentum k_π of each pion in the two-pion state is defined from the two-pion energy using the dispersion relation $E_{\pi\pi} = 2\sqrt{m_\pi^2 + k_\pi^2}$. The interactions between the two pions lead to k_π being different from 0 or $\sqrt{2}\pi/L$.

In the calculation of the $K \to \pi\pi$ matrix elements, the two-pion source is placed at time $t_{\pi\pi} = 0$ (or equivalently at 64) and the position of the kaon source t_K is varied using the different s-quark sources described in the previous section. In total, the analysis is performed for four separations δ_t between the kaon and two-pions sources, $\delta_t = 20, 24, 28$ and 32. The operators of the weak Hamiltonian are inserted between $t_{\pi\pi}$ and t_K. The symmetries of lattice QCD (including translation

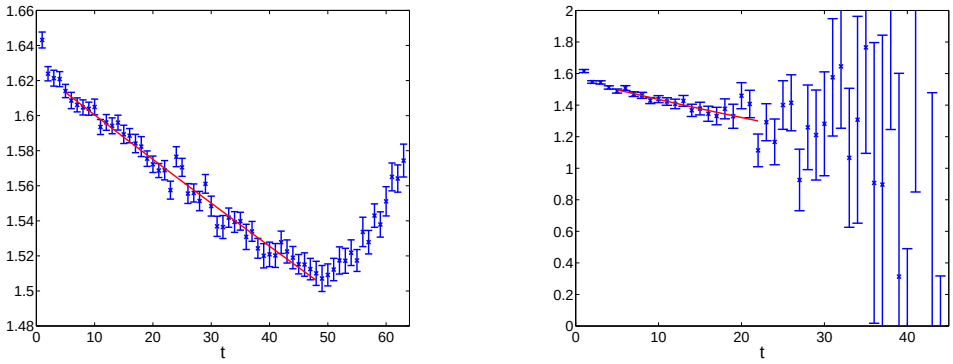

(a) $C_{\pi\pi}(t)/C_\pi^2(t), p = 0$ (b) $C_{\pi\pi}(t)/C_\pi^2(t), p = \sqrt{2}\pi/L$

Figure 8.3: *The ratios $C_{\pi\pi}(t)/(C_\pi(t))^2$ defined in Eq. (8.2) at $p = 0$ (left-hand plot) and at $p = \sqrt{2}\pi/L$ (right-hand plot). The minimum seen in the left-hand panel around $t = 52$ results from the different large-time behavior of the numerator and denominator. While the denominator decreases exponentially as t increases from 0 to 64, the numerator contains a small t-independent constant (caused by one backward propagating pion) which lessens its decrease at large time. If examined for $0 \leq t \leq 128$ the ratio shown in the left-hand panel is symmetrical about the point $t = 64$.*

invariance and time-reversal) allow the translation of the results into $K \to \pi\pi$ matrix elements.

For each of the three operators Q_i in Eq. (3.12), where i labels the operator, the corresponding $K \to \pi\pi$ matrix element $\mathcal{M}_i \equiv \langle \pi^+\pi^+ \,|\, Q_i \,|K^+\rangle$ is extracted by calculating the ratios

$$R(t_Q) \equiv \frac{C^i_{K\pi\pi}(t)}{C_K(t_K - t)C_{\pi\pi}(t)} = \frac{\mathcal{M}_i}{Z_K Z_{\pi\pi,e}} \tag{8.4}$$

and fitting to a constant in time t. The quantity $C^i_{K\pi\pi}$ is the $K \to \pi\pi$ correlator with the operator Q_i inserted at t and the kaon and two-pion interpolating operators placed at fixed times t_K and 0 respectively. Z_K and $Z_{\pi\pi,e}$ are determined from the kaon and two-pion correlation functions using Eqns. (7.15b) and (8.2). For illustration, the left-hand side of Eq. (8.4) is plotted in Fig. 8.4 for each of the three operators for the choice $\delta_t = 24$. The two-pion source is shown at $t = 0$ on this plot, and the kaon source is located at $t_K = 24$. The x-axis is labelled t_Q and illustrates the insertion of the weak-operator. The figure demonstrates that sufficiently far from the kaon and two-pion sources the data is indeed consistent with the expected

Table 8.3: *The two-pion energy $E_{\pi\pi}$, k_π, q_π and s-wave phase shift*

p	$E_{\pi\pi}$ (MeV)	k_π (MeV)	q_π	δ (degrees)
0	286.4(1.9)	17.63(36)	0.0659(13)	-0.311(18)
$\sqrt{2}\pi/L$	485.5(4.2)	196.8(2.2)	0.7350(72)	-7.96(2.07)

constant behavior. The matrix elements are determined by fitting the data between $t = 5$ and $t = t_K - 5$, where t denotes the time distance from the two-pion source. The results for $\mathcal{M}_i/(Z_K Z_{\pi\pi,e})$ obtained from the fits are indicated on the plot together with their errors. Additional plots showing the quotient $R(t_Q)$ for separations $\delta_t = 20, 28$ and 32 are included in Appendix B.

The finite-volume matrix elements computed in the lattice simulations $\mathcal{M}_i$ are related to the corresponding infinite-volume ones $\mathcal{A}_i$ by the Lellouch-Lüscher factor given in Eq. (6.39),

$$\mathcal{A}_i = \left[\frac{\sqrt{2^{n_{\rm tw}}}}{2\pi q_\pi}\sqrt{\frac{\partial\phi}{\partial q_\pi} + \frac{\partial\delta}{\partial q_\pi}}\right] \frac{2}{\sqrt{2^{n_{\rm tw}}}} L^{3/2}\sqrt{m_K} E_{\pi\pi}\mathcal{M}_i\,, \tag{8.5}$$

where the quantity in square brackets (denoted by LL in Tab. 8.4) contains the effects of the Lellouch-Lüscher factor beyond the free-field normalisation. δ is the s-wave phase shift, q_π is a dimensionless quantity related to the pion momentum k_π by $q_\pi = k_\pi L/2\pi$ and ϕ is a kinematic function defined in [59]. Once $E_{\pi\pi}$ has been measured and q_π determined, δ can be calculated using the Lüscher quantisation condition [53]:

$$n\pi = \delta(k_\pi) + \phi(q_\pi). \tag{8.6}$$

Results for $E_{\pi\pi}$, k_π, q_π and δ are presented in Tab. 8.3.

Since $\partial\phi/\partial q_\pi$ can be calculated analytically the only unknown in Eq. (8.5) is $\partial\delta/\partial q_\pi$. The results for the phase shift are plotted against k_π and compared with experimental results [60, 61] in Fig. 8.5; the results show good agreement. Near $p = 0$, δ is assumed to be linear in k_π in order to calculate $\partial\delta/\partial q_\pi$ (see Fig. 8.5). For $p = \sqrt{2}\pi/L$ the phenomenological curve [62] shown in Fig. 8.5 is used to calculate the derivative of the phase shift at the corresponding value of q_π. The derivative of the phase shift is found to be a small term in comparison with $\partial\phi/\partial q_\pi$.

Table 8.4: *Contributions to Lellouch-Lüscher factor. The second and third columns provide numerical values for two of the quantities entering the Lellouch-Lüscher factor given within the square brackets in Eq. (8.5), while the fourth column gives the value of the complete factor.*

p	$\partial\phi/\partial q_\pi$	$\partial\delta/\partial q_\pi$	LL
0	0.2413(90)	-0.0824(32)	0.9632(14)
$\sqrt{2}\pi/L$	5.014(21)	-0.2911(23)	0.9411(71)

Results for $\partial\phi/\partial q_\pi$ and $\partial\delta/\partial q_\pi$ are presented in Tab. 8.4.

The physical decay amplitude A_2 is given in terms of the matrix elements $\mathcal{A}_i$ by

$$A_2^{\delta t} = a^{-3}\frac{\sqrt{3}}{2}\frac{G_F}{\sqrt{2}}V_{ud}V_{us}^*\sum_{i,j}C_i(\mu)Z_{ij}(\mu a)\mathcal{A}_j^{\delta t}\,, \tag{8.7}$$

where the label δt has been added to indicate the $K-\pi\pi$ separation being used and the labels i and j run over the three operators in Eq. (3.12). C_i are the Wilson coefficients, which have been calculated in the $\overline{\text{MS}}$-NDR scheme. The Z_{ij} are the renormalisation constants which relate the bare weak operators defined in the lattice theory (where the lattice spacing a acts as a cut-off) to those in the $\overline{\text{MS}}$-NDR scheme at scale μ. The $(27,1)$ operator renormalises multiplicatively, whereas the $(8,8)$ and $(8,8)_{\text{mix}}$ operators mix under renormalisation. The calculation of the Z_{ij} is described in detail in Chapter 5 and involves a non-perturbative calculation of the renormalisation constants in RI-SMOM schemes, step-scaling to run the results to $\mu = 3\,\text{GeV}$ and matching perturbatively to the $\overline{\text{MS}}$-NDR scheme. As explained in Chapter 5, four possible choices for the intermediate RI-SMOM schemes are considered. The results presented in Tab. 8.5 are calculated using the renormalisation constants with the intermediate scheme $(\text{I}_\text{v},\text{I}_\text{q}) = (\not{q},\not{q})$ (see Chapter 5).

Results for $\text{Re}A_2$ and $\text{Im}A_2$ for the four different separations δt are shown in Tab. 8.5 for the (almost) physical choice $p = \sqrt{2}\pi/L$. Our final result for A_2 is an error weighted average (EWA) over the four separations, defined by

$$A_2^{\text{EWA}} = \frac{\sum_{\delta t}A_2^{\delta t}/(e_{\delta t})^2}{\sum_{\delta t}1/(e_{\delta t})^2}\,, \tag{8.8}$$

where $e_{\delta t}$ is the statistical error in the evaluation of $A_2^{\delta t}$.

Table 8.5: *Final results for A_2. The errors on each $A_2^{\delta t}$ and the first error in the EWA(b) (error weighted average) are the statistical errors only. In the EWA(b) result the second error is that due from the statistical uncertainty in the renormalisation constants given in Eq.* (5.26).

δt	ReA_2(units of 10^{-8} GeV)	ImA_2(units of 10^{-13} GeV)
20	1.411(56)	-6.59(19)
24	1.346(64)	-6.67(22)
28	1.427(73)	-6.28(25)
32	1.295(94)	-6.56(33)
EWA(a)	1.381(38)	-6.54(15)
EWA(b)	1.381(44)(12)	-6.54(19)(42)

The errors in the results labelled by EWA(a) in Tab. 8.5 are due to the statistical fluctuations on the $\mathcal{A}_i$ calculated using Eq. (8.5). In the row marked EWA(b) the first error combines the uncertainty due to these fluctuations with the statistical uncertainty in the value of the lattice spacing and the second error is Δ_Z, which arises from the statistical uncertainty in the evaluation of the renormalisation constants Z_{ij}. This is calculated using:

$$\Delta_Z^2 = \left[C_{(27,1)}\,\delta Z_{(27,1)}\,\mathcal{A}_{(27,1)}\right]^2 + \sum_{i,j}\Big[\,C_i\,\delta Z_{ij}\,\mathcal{A}_j\,\Big]^2\,, \tag{8.9}$$

where i, j run over $(8,8)$ and $(8,8)_{\rm mix}$ and the δZ are the statistical uncertainties in the corresponding renormalisation constants given by the first error in Eq. (5.26). The presence of the four terms in the sum over i and j reflects the mixing of $Q_{(8,8)}$ and $Q_{(8,8)_{\rm mix}}$ under renormalisation. $\mathcal{A}_{(27,1)}$, $\mathcal{A}_{(8,8)}$ and $\mathcal{A}_{(8,8)_{\rm mix}}$ on the right-hand side of Eq. (8.9) are obtained from the corresponding bare matrix elements using Eq. (8.5). The numerical results presented here were obtained by using the statistical errors $e_{\delta t}$ in the evaluation of A_2 so that for example:

$$\mathcal{A}_{(27,1)} = \frac{\sum_{\delta t}\mathcal{A}_{(27,1)}^{\delta t}/(e_{\delta t})^2}{\sum_{\delta t}1/(e_{\delta t})^2}\,, \tag{8.10}$$

and similarly for the remaining operators. We have checked that performing the error weighted average on each operator using the statistical error corresponding to the operator makes only a negligible difference to the estimate of the final errors.

Using the procedures described above along with the Wilson coefficients given in Tab. 3.2, the final results for the complex amplitude A_2 are:

$$\mathrm{Re}A_2 = 1.381(46)_{\mathrm{stat}}(258)_{\mathrm{syst}}\,10^{-8}\,\mathrm{GeV}, \quad \mathrm{Im}A_2 = -6.54(46)_{\mathrm{stat}}(120)_{\,\mathrm{syst}}10^{-13}\,\mathrm{GeV}\,. \tag{8.11}$$

The result for $\mathrm{Re}A_2$ agrees well with the experimental value of $1.479(4) \times 10^{-8}\,\mathrm{GeV}$ obtained from K^+ decays and $1.573(57) \times 10^{-8}\,\mathrm{GeV}$ obtained from K_S decays (the small difference arises from the unequal u and d quark masses and from electromagnetism, two small effects not included in our calculation). $\mathrm{Im}A_2$ is unknown so that the result in Eq. (8.11) provides its first direct determination (updating the value quoted in [6]).

A detailed discussion of the determination of the systematic errors will be presented in the following sections. As explained earlier, the statistical error was obtained by analysing configurations each separated by 8 molecular dynamics time units, and the gauge fields were shifted by 16 lattice spacings in the time direction prior to successive measurements. In order to check that shifting the gauge fields is sufficient to overcome potential autocorrelations, the entire analysis has been repeated, including the determination of the physical quark masses and lattice spacings, by binning all quantities over four successive measurements (32 molecular dynamics time units). This is a natural choice as it matches the periodicity of the quark propagator measurements. The effects of the binning are completely negligible. For illustration Tab. 8.6 shows a comparison of the results for A_2 obtained with and without the binning.

8.2 Reweighting the light sea quarks

The technique of reweighting was introduced in Chapter 4.4.1. In this section the light quark mass is reweighted in order to investigate the effects of its partial quenching.

The reweighting is performed in 30 increments from the simulated mass $am_l^{\mathrm{sea}} = 0.001$ down to a value of $am_l^{\mathrm{sea}} = 0.0001$ which corresponds to the valence

Table 8.6: *Final results for ReA_2 in units of 10^{-8} GeV and ImA_2 in units of 10^{-13} GeV. The table shows a comparison between the results obtained as in Tab. 8.5 (146 bins each with a single configurations) and those with bin-size 4 (36 bins each with 4 configurations). The error on EWA(a) was defined in Tab. 8.5.*

	ReA_2		ImA_2	
δt	146 bins	36 bins	146 bins	36 bins
20	1.411(56)	1.418(52)	-6.59(19)	-6.55(16)
24	1.345(64)	1.344(57)	-6.67(22)	-6.60(20)
28	1.427(73)	1.411(83)	-6.28(25)	-6.23(29)
32	1.295(94)	1.28(10)	-6.56(33)	-6.58(31)
EWA(a)	1.381(38)	1.386(34)	-6.54(15)	-6.52(14)

Table 8.7: *A_2 before and after reweighting. The quoted errors correspond to the statistical fluctuations in the correlation functions only. The statistical uncertainties in the determination of the lattice spacing and non-perturbative renormalisation have been omitted here.*

	$am_l = 0.001$	$am_l = 0.0001$ (reweighted)
ReA_2	$1.381(38) \times 10^{-8}$ GeV	$1.367(65) \times 10^{-8}$ GeV
ImA_2	$-6.54(15) \times 10^{-13}$ GeV	$-6.91(23) \times 10^{-13}$ GeV

light-quark mass and the results are shown in Fig. 8.6. For a more accurate indication of the relative decrease of the masses from 0.001 to 0.0001, note that $am_l + am_{\rm res}$ decreases from 0.0028 to 0.0019. The rightmost point in Fig. 8.6(a) shows the result for ReA_2 before reweighting, while the remaining points show the results after reweighting to the mass indicated on the x-axis, ending with $am_l^{\rm sea} = 0.0001$ for the leftmost point. Similarly Fig. 8.6(b) shows the effects of reweighting on ImA_2. The final results after reweighting are shown in Tab. 8.7 where they are compared with the results before reweighting. In this table, for illustration of the effects of reweighting, only the statistical error from the correlation functions themselves is included; the statistical errors from the determination of the lattice spacing and renormalisation are not included, nor are any of the systematic errors.

Examining the figures, it can be seen that, as expected, the statistical errors on ReA_2 and ImA_2 grow. Table 8.7 shows that, within errors, the real part of A_2 does not change after reweighting. By contrast, the imaginary part of A_2 decreases by 5.7%. After including all of the statistical and systematic errors, the reweighted

Table 8.8: *Systematic error budget for ReA_2 and ImA_2.*

	$\mathrm{Re}A_2$	$\mathrm{Im}A_2$
lattice artefacts	15%	15%
finite-volume corrections	6.0%	6.5%
partial quenching	3.5%	1.7%
renormalisation	1.8%	5.6%
unphysical kinematics	0.4%	0.8%
derivative of the phase shift	0.97%	0.97%
Wilson coefficients	6.6%	6.6%
Total	18%	19%

result for for the complex amplitude A_2 is:

$$\mathrm{Re}A_2 = 1.367(70)_{\mathrm{stat}}(246)_{\mathrm{syst}}\,10^{-8}\,\mathrm{GeV}, \quad \mathrm{Im}A_2 = -6.91(51)_{\mathrm{stat}}(131)_{\mathrm{syst}}10^{-13}\,\mathrm{GeV}\,. \tag{8.12}$$

The results of Eq. (8.12) should be compared with Eq. (8.11), and it is clear that the differences due to reweighting are well within the total error. The conclusion is that partial quenching has a negligible effect on the final answer for the decay amplitudes.

8.3 Error Budget

The sources of systematic error in the calculation of $\mathrm{Re}A_2$ and $\mathrm{Im}A_2$ include those from lattice artefacts, finite-volume effects, partial quenching, the uncertainty in the non-perturbative renormalisation, the unphysical kinematics used in the calculation, the determination of the derivative of the phase shift and the Wilson coefficients. A brief discussion of each of the sources of systematic error is included in this section. Each contribution to the total systematic error can be found in Tab. 8.8.

8.3.1 Estimating the Error due to Lattice Artefacts

The calculation of the complex $K \to \pi\pi$ amplitude was performed at a single, rather large, value of the lattice spacing, $a^{-1} = 1.364(9)\,\mathrm{GeV}$. This value of the lattice spacing was obtained in Ref. [58] by using the mass of the Ω-baryon to set the scale and the masses of the pion and kaon to determine the physical quark

Table 8.9: *Values of the inverse lattice spacing obtained using different physical quantities to set the scale. The value* $r_0 = 2.433(50)(18)(13)\,\mathrm{GeV}^{-1} = 0.4795(99)(35)(26)\,fm$*, taken from a detailed analysis in [58], is used for the Sommer scale. The two columns of results correspond to the use of finite-volume SU(2) chiral perturbation theory or the analytic ansatz for the light-quark mass dependence.*

Quantity	ChPTFV	Analytic
m_Ω	1.364(8) GeV	1.362(11) GeV
f_π	1.410(27) GeV	1.386(19) GeV
f_K	1.413(29) GeV	1.392(28) GeV
r_0	1.357(4) GeV	1.362(7) GeV

masses. With the IDSDR action, all other computed physical quantities have errors of $O(a^2)$, but without a simulation at a second lattice spacing it is not possible to determine these lattice artefacts directly. In this section an indirect estimate of the $O(a^2)$ effects, which represent the largest single contribution to the systematic uncertainty, is described.

Two related methods are used to estimate the artefacts. In the first of these, quantities other than m_Ω are used to set the scale and the corresponding variation is ascribed to the artefacts. The results are presented in Tab. 8.9. The difference between the largest and smallest entry in the table is about 4%. Recalling that the $K \to \pi\pi$ matrix elements are of dimension 3, the corresponding uncertainty in the amplitudes is estimated to be 10-15%. On the other hand, it could be argued that the physical value of r_0 is not very well known, and that a more suitable criteria is to impose that the same value of r_0 is obtained on both the Iwasaki and IDSDR lattices. This fixes the ratio of lattice spacings on the two ensembles. Combining this ratio with the well determined lattice spacing on the Iwasaki ensembles from m_Ω leads to the IDSDR value $a^{-1} = 1.363(22)\,\mathrm{GeV}$, closer to those obtained from m_Ω and the decay constants. Although this may suggest that the 10-15% estimate is conservative, because of the indirect nature of these estimates, it is better to be conservative when quoting the uncertainties.

As a second approach the scale is set from m_Ω and the matrix element $M^{\Delta S=2} = \langle \bar{K}^0 | (\bar{s}\gamma^\mu(1-\gamma^5)d)\,(\bar{s}\gamma^\mu(1-\gamma^5)d) | K^0 \rangle$ is studied on both the Iwasaki and IDSDR lattices. This matrix element gives the dominant contribution to the

indirect CP-violation parameter ϵ and is in the same representation of the chiral symmetry as $Q_{(27,1)}$. The next step is to perform a global chiral and continuum fit using the form

$$M^{\Delta S=2} = c_0(1 + c_a^{\mathrm{I,IDSDR}}\, a^2) + c_l\tilde{m}_l + c_h(\tilde{m}_h - \tilde{m}_{h_0}) + c_x\tilde{m}_x + c_y(\tilde{m}_y - \tilde{m}_{h_0})\,, \quad (8.13)$$

where $\tilde{m}_l$ and $\tilde{m}_x$ are the sea and valence light-quark masses, $\tilde{m}_h$ and $\tilde{m}_y$ the corresponding strange-quark masses and $\tilde{m}_{h_0}$ is the physical bare strange quark mass. The coefficient c_a depends on the action as indicated. By performing the global fits, c_a^{IDSDR} can be determined and the size of the lattice artefacts can be determined. Using all of the available data the artefacts are found to be 12% in the SU(2) chiral limit and 18% at the physical quark masses. If the data are restricted to pions with masses less than 350 MeV, the artefacts are found to be 10% in the chiral limit and 14% for physical quark masses.

Based on these calculations, the uncertainty due to the lattice artefacts is estimated as being 15%, which will be combined with the remaining uncertainties in quadrature. This estimate of the discretization error includes possible artefacts in the conversion of the renormalisation constants from the IDSDR to the Iwasaki lattices. Comparing this error with the other errors in Tab. 8.8, it is clear that lattice artefacts are the dominant source of systematic error. However, they will be reliably reduced when the calculations are repeated at a second lattice spacing.

8.3.2 Finite-Volume Corrections

In order to estimate the systematic error due to the finite volume of the lattice, SU(3) finite-volume chiral perturbation theory is used, in which the loop-integrals in Feynman diagrams are replaced by discrete sums over the allowed momenta. Expressions for the $\Delta I = 3/2$ $K \to \pi\pi$ matrix elements, $\mathcal{M}_{(27,1)} = \langle \pi^+\pi^-|Q_{(27,1)}|K^0\rangle$ and $\mathcal{M}_{(8,8)} = \langle \pi^+\pi^-|Q_{(8,8)}|K^0\rangle$ are known to next-to-leading order in $SU(3)$ chiral perturbation theory. Since in chiral perturbation theory to leading order there is a single $\Delta I = 3/2$ operator constructed from the Goldstone boson fields which transforms as the (8,8)

representation, the estimates derived below are the same for $Q_{(8,8)}$ and $Q_{(8,8)_{\rm mix}}$. There is also a single operator at lowest order which transforms as the (27,1) representation. We will be considering the leading order terms (labelled by "LO") and leading (one-loop) logarithmic terms (labelled by "log"). The LO expressions are well known and can be found in [64] and [65]. For $\mathcal{M}^{\rm log}_{(27,1)}$ we use Eq. (C5) in [64], (where we have added logarithmic terms from $(m_K^2 - m_\pi^2)_{\text{1-loop}}$ by hand as necessitated by Eq. (25) of [64] and corrected a factor of $1/f^2$ in equation (A2)), and for $\mathcal{M}^{\rm log}_{(8,8)}$ we use Eq. (E3) in [65].

We denote the finite-volume corrections to the logarithmic terms in $\mathcal{M}_{(27,1)}$ and $\mathcal{M}_{(8,8)}$ by $\Delta\mathcal{M}^{\rm log}_{(27,1)}$ and $\Delta\mathcal{M}^{\rm log}_{(8,8)}$ respectively. We estimate the relative size of these corrections, by using the pion and kaon masses in our lattice calculation finding,

$$\frac{\Delta\mathcal{M}^{\rm log}_{(27,1)}}{\mathcal{M}^{\rm LO}_{(27,1)}} = 0.0597 \qquad \text{and} \qquad \frac{\Delta\mathcal{M}^{\rm log}_{(8,8)}}{\mathcal{M}^{\rm LO}_{(8,8)}} = 0.0649 \tag{8.14}$$

if we normalise to the leading order expressions of the matrix elements, and

$$\frac{\Delta\mathcal{M}^{\rm log}_{(27,1)}}{\left|\mathcal{M}^{\rm LO}_{(27,1)} + \mathcal{M}^{\rm log}_{(27,1)}\right|} = 0.0352 \qquad \text{and} \qquad \frac{\Delta\mathcal{M}^{\rm log}_{(8,8)}}{\left|\mathcal{M}^{\rm LO}_{(8,8)} + \mathcal{M}^{\rm log}_{(8,8)}\right|} = 0.0438 \tag{8.15}$$

if we normalise to the leading order plus leading logarithmic expressions. More details can be found in [5].

Evidently the leading logarithmic terms make significant corrections to the leading order terms. To have confidence that the chiral perturbation theory is converging we should check the size of the next-to-leading-order terms, but as these have unknown coefficients we are unable to make a numerical estimate. We therefore make a conservative estimate by taking the larger relative finite-volume correction of Eq. (8.14) and conclude that the (27,1) operator carries a 6.0% finite-volume correction and that the (8,8) operator carries a 6.5% finite-volume correction. Since $\mathrm{Re}A_2$ is dominated by the (27,1) operator and $\mathrm{Im}A_2$ is dominated by the $(8,8)_{\rm mix}$ operator, these are the percentage errors due to finite-volume effects we assign to $\mathrm{Re}A_2$ and $\mathrm{Im}A_2$ respectively.

Table 8.10: *The amplitude A_2, computed on the Iwasaki ensembles, after extrapolation to physical kaon and pion masses. The two pions in the final state are at rest (up to finite-volume effects) and energy is not conserved in these amplitudes (see text).*

	$m_l = 0.004$	$m_l = 0.006$	$m_l = 0.008$
$\mathrm{Re(A_2)}\times 10^8$ GeV	0.697(44)	0.748(41)	0.719(38)
$\mathrm{Im(A_2)} \times 10^{13}$ GeV	-14.73(37)	-14.99(35)	-15.23(34)

8.3.3 Partial Quenching

The calculations described in this chapter were designed to have almost physical kinematics, i.e. the kaon and pions have masses which are close to their physical values. This is achieved however, by the sea and valence quark masses being different; the sea-quark masses are $m_l^{\mathrm{sea}} = 0.001$ and $m_h^{\mathrm{sea}} = 0.045$ and the valence masses are $m_l^{\mathrm{valence}} = 0.0001$ and $m_h^{\mathrm{valence}} = 0.049$. The dependence on the sea-quark mass is not expected to be very significant, and this was demonstrated in Sec. 8.2. This section collects the results of a previous investigation of the sea-quark mass dependence performed with 32^3 Iwasaki lattice [5].

Sea-quark mass dependence on the 32^3 Iwasaki lattices

$K \to \pi\pi$ correlation functions were also computed on the $32^3 \times 64$, $L_s = 16$ Iwasaki lattices ($a^{-1} = 2.285(29)$ GeV) with three different light sea-quark masses $m_l^{\mathrm{sea}} = 0.004, 0.006, 0.008$ [5, 66]. For each of the sea-quark masses, the correlation functions were calculated using several valence masses: $m^{\mathrm{valence}} = 0.002, 0.004, 0.006, 0.008, 0.025, 0.03$. Periodic boundary conditions were used, so the pions have zero momentum, resulting in a decay which does not conserve energy. For each of the three sea-quark masses, a chiral extrapolation was performed over the valence masses to determine the $K \to \pi\pi$ amplitudes corresponding to physical kaon and pion masses (for the strange quark in the kaon this was an interpolation). The results are summarised in Tab. 8.10.

From the table it can be seen that any dependence on the light sea-quark mass is small, and generally within the statistical uncertainties. The standard deviation of the results obtained with the different sea light-quark masses is used as an estimate

of the uncertainty; 3.5% for Re(A_2) and 1.7% for Im(A_2). Although the kinematics are different from those for the physical decay on the IDSDR lattice, this result is still taken to be an estimate of the error due to partial quenching. The range of sea-quark masses on the Iwasaki lattices and the long length of the extrapolation suggest that this may be a conservative estimate. No attempt is made to estimate the error due to the partial quenching of the strange quark, but note that the deviation from unitarity in the strange-quark mass is relatively small ($m_h^{\text{sea}} = 0.045$ compared to $m_s^{\text{valence}} = 0.049$) .

8.3.4 Uncertainties due to the Renormalisation

Two main sources of systematic error from the calculation of the renormalisation constants are discussed in this section. The first is designed to take into account lattice artefacts of higher order than $\mathcal{O}(a^2)$ in the continuum extrapolation of the step-scaling function using the Iwasaki lattices, as described in Sec. 5.1.1, and corresponds to the second error in Eq. (5.25). This systematic error is estimated in the same way that the statistical NPR error on A_2 is calculated, i.e. Eq. (8.9) is used, but in this case δZ denotes the systematic errors on the Z-factors. The resulting error is displayed in Tab. 8.11 and is labelled NPR-sys. This is found to be a 1.1% effect for ReA_2 and a 5.0% effect for ImA_2 (see the second row of the table).

The second source of systematic error in the renormalisation constants is due to the truncation error in the perturbative matching to the $\overline{\text{MS}}$ scheme and to $\mathcal{O}(a^2)$ scaling errors since only one lattice spacing is available and the Z-factors in the different schemes need not approach the continuum limit along the same scaling trajectory. Following conversion to the $\overline{\text{MS}}$ scheme, the four intermediate NPR schemes described in Chapter 5 should give equivalent answers. An estimate of the resulting systematic error is made by considering the spread in results when A_2 is calculated in the RI-SMOM(γ_μ, γ_μ) scheme and in the RI-SMOM($\not{q}, \not{q}$) scheme.

The results for A_2 in the RI-SMOM(γ_μ, γ_μ) and RI-SMOM($\not{q}, \not{q}$) schemes are presented in Tab. 8.11. A spread of 1.4% is observed for ReA_2 and a 2.5% spread is observed for ImA_2. Combining the two sources of error in quadrature, the result is

Table 8.11: *ReA_2 and ImA_2 calculated in the two different schemes.*

	$\mathrm{Re}A_2$ $\times 10^8$ GeV	$\mathrm{Im}A_2$ $\times 10^{13}$ GeV
RI-SMOM($\not{q}, \not{q}$)	$1.381(46)_{\mathrm{stat}}(15)_{(\mathrm{NPR\text{-}sys})}$	$-6.54(46)_{\mathrm{stat}}(33)_{(\mathrm{NPR\text{-}sys})}$
RI-SMOM(γ_μ, γ_μ)	$1.362(44)_{\mathrm{stat}}(03)_{(\mathrm{NPR\text{-}sys})}$	$-6.35(34)_{\mathrm{stat}}(42)_{(\mathrm{NPR\text{-}sys})}$

a 1.8% error for $\mathrm{Re}A_2$ and a 5.6% error for $\mathrm{Im}A_2$.

8.3.5 Uncertainties due to the Unphysical Kinematics

When choosing the parameters of the simulation, including the quark masses, the coupling constant and even the volume, the aim was to obtain physical kaon and pion masses and $E_{\pi\pi} = m_K$. Once the simulation has been performed, it is natural to find that this is not quite the case (see Tab. 8.2) and in this section an attempt is made to estimate the systematic error that these non-physical kinematics contribute to the calculation.

In addition to the results from the current simulation, a large collection of $K \to \pi\pi$ amplitudes has been calculated on quenched lattices with a variety of light and strange quark masses and pion momenta. The observed dependence of the amplitudes with the quark masses is used to estimate the uncertainty due to the unphysical kinematics. A total of 60 values for the $K \to \pi\pi$ amplitudes has been collected on the quenched lattices, obtained with all combinations of $am_l = 0.0023$, 0.0047, 0.0071, $am_s = 0.046$, 0.062, 0.078, 0.094, 0.110 and with $n = 0$, 1, 2 and 3, where n is the number of spatial directions in which antiperiodic boundary conditions are imposed. The allowed momentum of a each pion with antiperiodic boundary conditions in n directions is $\sqrt{n}\pi/L$, so n parameterises the pion momenta.

The procedure for estimating the systematic error due to non-physical kinematics uses these quenched amplitudes, extrapolating the results in am_l and interpolating them in am_s and n, first to physical kinematics, and then to the kinematics simulated on the IDSDR lattices. This procedure is described in detail in [5], and is very similar to the extrapolation procedure described in Sec. 8.3.3 when computing the error due to partial quenching. The difference here is that it is now possible to

interpolate to the correct pion-momenta. This is achieved by fitting the two-pion energy as a function of n, and interpolating to find n^{phys}, the value of n which corresponds to the desired two-pion energy. This in turn allows the decay amplitude to be interpolated and evaluated at n^{phys}.

After extrapolation to physical kinematics, the results from the quenched lattices are:

$$\text{Re}A_2 = 2.25 \times 10^{-8}\,\text{GeV}, \quad \text{Im}A_2 = -13.45 \times 10^{-13}\,\text{GeV}\,, \tag{8.16}$$

while the extrapolation to m_π, m_K and $E_{\pi\pi}$ simulated in this chapter gives

$$\text{Re}A_2 = 2.26 \times 10^{-8}\,\text{GeV}, \quad \text{Im}A_2 = -13.56 \times 10^{-13}\,\text{GeV}\,. \tag{8.17}$$

The percentage differences between the two extrapolations is taken as a measure of the systematic error due to simulating at non-physical kinematics, with results of 0.4% for ReA_2 and 0.8% for ImA_2.

8.3.6 Uncertainty in the Derivative of the Phase Shift

The derivative of the s-wave phase shift $\partial\delta/\delta k$ appearing in the Lellouch-Lüscher factor was found by evaluating the derivative of the phenomenological curve at the momentum simulated in our lattice calculation. This was discussed in Sec. 8.1 and illustrated in Fig. 8.5. Alternatively the slope of the straight line between the phase shift at 17.63 MeV and 196.8 MeV could have been used to make a crude estimate of the derivative of the phase shift. (c.f. the results of Tab 8.3). The systematic error is estimated to be 0.97%, which is found by calculating the percentage difference between the final results as obtained by the two different approaches. Since the derivative of the phase-shift only contributes a small fraction to the Lellouch-Lüscher factor (see Tab. 8.4) it is not surprising that the corresponding error is negligible. The derivative of the phase-shift can also be calculated directly using the method proposed in [67].

Table 8.12: ReA_2 *and* ImA_2 *as calculated with LO Wilson coefficients and NLO Wilson coefficients. The errors quoted here represent the total statistical uncertainty.*

	LO	NLO
ReA_2	$1.289(42)\times10^{-8}$ GeV	$1.381(46)\times10^{-8}$ GeV
ImA_2	$-6.11(36)\times10^{-13}$ GeV	$-6.54(46)\times10^{-13}$ GeV

8.3.7 Uncertainties in the evaluation of the Wilson coefficients

The Wilson coefficients, which are calculated in perturbation theory and hence are not part of the lattice computations, are a necessary ingredient in the determination of the amplitude A_2. The values presented in Tab. 3.2 were calculated at next-to-leading order (NLO) following the procedure outlined in Chapter 3. In this section as estimate is made of the systematic error due to the truncation of perturbation theory. To this end the LO Wilson coefficeints, given in Tab. 3.3, are used instead of the NLO values and the effect this has on the final results for ReA_2 and ImA_2 are measured.

Table. 8.12 shows how the decay amplitude varies when the LO Wilson coefficients are used instead of the NLO Wilson coefficients. The error in A_2 due to the truncation in the perturbative calculation of the Wilson coefficients is very conservatively estimated by taking the difference between the NLO result and the LO result, and calculating this as a percentage of the LO result. The resulting estimate of the systematic error is 7.1% for ReA_2 and 8.1% for ImA_2.

8.4 Results

The main result of this thesis is the final value for the complex amplitude A_2,

$$\mathrm{Re}A_2 = 1.381(46)_{\mathrm{stat}}(258)_{\mathrm{syst}}\,10^{-8}\,\mathrm{GeV}, \quad \mathrm{Im}A_2 = -6.54(46)_{\mathrm{stat}}(120)_{\,\mathrm{syst}}10^{-13}\,\mathrm{GeV}\,. \tag{8.18}$$

This result was obtained with nearly-physical kinematics and a full consideration of all sources of systematic error.

In the remainder of this chapter the results are presented for each of the three

matrix elements which contribute to A_2 (Sec. 8.4.1) and the value of the unknown quantity $\mathrm{Im}\, A_0$ is also deduced by combining the result obtained for $\mathrm{Im}A_2$ with the experimental values of ϵ'/ϵ and other quantities (Sec. 8.4.3).

8.4.1 Results for the matrix elements

Equation (8.11) contains the final results for A_2 within the Standard Model. In order to facilitate detailed comparisons with results from future computations and to enable these results to be used in extensions of the Standard Model for which the Wilson coefficient functions are different, results for the $K \to \pi\pi$ matrix elements are now presented. The results are presented for operators renormalised in the $\overline{\mathrm{MS}}$-NDR scheme at a renormalisation scale of 3 GeV.

$K^+ \to \pi^+\pi^+$ matrix elements

The amplitude A_2 is given in terms of the $K^+ \to \pi^+\pi^+$ matrix elements of the operators defined in Eq. (3.12) by

$$A_2 = \frac{G_F}{\sqrt{2}} V_{ud} V_{us}^* \frac{\sqrt{3}}{2} \sum_i C_i(3\ \mathrm{GeV}) \mathcal{A}_i^{\overline{\mathrm{MS}}\text{-NDR}}(3\ \mathrm{GeV})\,, \tag{8.19}$$

where $\mathcal{A}_i^{\overline{\mathrm{MS}}\text{-NDR}} = \langle\, \pi^+\pi^+ \,|\, Q_i \,|K^+\rangle$ and the label i runs over (27,1), (8,8) and $(8,8)_{\mathrm{mix}}$. The $\mathcal{A}_i$ take the values

$$\mathcal{A}_{(27,1)}^{\overline{\mathrm{MS}}\text{-NDR}}(3\ \mathrm{GeV}) = 0.03071(97)\ \mathrm{GeV}^3 \tag{8.20a}$$

$$\mathcal{A}_{(8,8)}^{\overline{\mathrm{MS}}\text{-NDR}}(3\ \mathrm{GeV}) = 0.583(33)\ \mathrm{GeV}^3 \tag{8.20b}$$

$$\mathcal{A}_{(8,8)_{\mathrm{mix}}}^{\overline{\mathrm{MS}}\text{-NDR}}(3\ \mathrm{GeV}) = 2.64(15)\ \mathrm{GeV}^3\,. \tag{8.20c}$$

Alternatively A_2 may be expressed in terms of the matrix elements for the physical $K^+ \to \pi^+\pi^0$ decay. In this case

$$A_2 = \frac{G_F}{\sqrt{2}} V_{ud} V_{us}^* \frac{1}{\sqrt{3}} \sum_i C_i(3 \text{ GeV}) \mathcal{A}_i'^{\overline{\text{MS}}\text{-NDR}}(3 \text{ GeV}). \tag{8.21}$$

where the two-pion final state is symmetrised ($\frac{1}{\sqrt{2}} (\langle \pi^+(\vec{p})\pi^0(-\vec{p})| + \langle \pi^+(-\vec{p})\pi^0(\vec{p})|$). The results are

$$\mathcal{A}_{(27,1)}'^{\overline{\text{MS}}\text{-NDR}}(3 \text{ GeV}) = 0.0461(14) \text{ GeV}^3 \tag{8.22a}$$

$$\mathcal{A}_{(8,8)}'^{\overline{\text{MS}}\text{-NDR}}(3 \text{ GeV}) = 0.874(49) \text{ GeV}^3 \tag{8.22b}$$

$$\mathcal{A}_{(8,8)_{\text{mix}}}'^{\overline{\text{MS}}\text{-NDR}}(3 \text{ GeV}) = 3.96(23) \text{ GeV}^3 . \tag{8.22c}$$

8.4.2 Contributions to A_2 from the Matrix Elements

The separate contributions to A_2 in Eq. (8.11) from the matrix elements of the three different operators are now given:

$$\begin{array}{l|ll} (27,1) & \text{ReA}_2 = (1.398 \pm 0.044)\, 10^{-8} \text{ GeV}; & \text{ImA}_2 = (1.55 \pm 0.36)\, 10^{-13} \text{ GeV} \\ (8,8) & \text{ReA}_2 = (4.29 \pm 0.24)\, 10^{-11} \text{ GeV}; & \text{ImA}_2 = (4.47 \pm 0.25)\, 10^{-14} \text{ GeV} \\ (8,8)_{\text{mx}} & \text{ReA}_2 = (-2.14 \pm 0.12)\, 10^{-10} \text{ GeV}; & \text{ImA}_2 = (-8.14 \pm 0.47)\, 10^{-13} \text{ GeV} . \end{array} \tag{8.23}$$

Since the $(8,8)$ and $(8,8)_{\text{mx}}$ operators mix under renormalisation, these exact figures are only valid at the renormalisation scale 3 GeV. Nevertheless, they demonstrate that the largest contribution to $\text{Re}A_2$ is from the $(27,1)$ operator while the largest contribution to $\text{Im}A_2$ is from the $(8,8)_{\text{mx}}$ operator Q_8.

8.4.3 Prediction for Im A_0

Having calculated A_2, and recalling that ReA_0 is known from experiment, the unknown quantity Im A_0 may be determined by combining the lattice result for ImA_2/ReA_2 from Tab. 8.5 with the experimental values of Re (ϵ'/ϵ) defined in Eq. (2.22), ϵ and $\omega \equiv$ ReA_2/ReA_0.

The numerical values which are used for these quantities are given in Tab. 8.13. The systematic error on ImA_2/ReA_2 is found by combining in quadrature the systematic error on ReA_2 and ImA_2 with the error due to lattice artefacts excluded. A single estimate of 5% systematic error on ImA_2/ReA_2 due to lattice artefacts is then added in quadrature. This estimate is based on the Symanzik theory of improvement which implies that the artefacts are proportional to a^2 and in the absence of any knowledge of the constant of proportionality, the spread of the derived values of the lattice spacing in Tab 8.9 below is used as a guide. The result and error for ImA_0/ReA_0 are very insensitive to the estimate of the artefacts in ImA_2/ReA_2.

Rearranging Eq. (2.22), the imaginary part of A_0 is found within the Standard Model to be

$$\mathrm{Im}A_0 = -5.34(62)_{\mathrm{stat}}(68)_{\mathrm{syst}} \times 10^{-11} \text{ GeV}. \tag{8.24}$$

The error on ImA_0 is obtained by combining the errors on the quantities in Tab. 8.13 in quadrature. In Eq. (8.25) below we compare the relative contribution to ImA_0/ReA_0 from ImA_2/ReA_2 and the term containing the experimentally known contributions:

$$\frac{\mathrm{Im}A_0}{\mathrm{Re}A_0} = \frac{\mathrm{Im}A_2}{\mathrm{Re}A_2} - \frac{\sqrt{2}\,|\epsilon|}{\omega}\frac{\epsilon'}{\epsilon}$$

$$-1.61(19)_{\mathrm{stat}}(20)_{\mathrm{syst}} \times 10^{-4} = -4.42(31)_{\mathrm{stat}}(89)_{\mathrm{syst}} \times 10^{-5} - 1.16(18) \times 10^{-4}\,. \tag{8.25}$$

After studying Eq. (8.25) it is apparent that the contribution of ImA_2/ReA_2 to ImA_0/ReA_0 is significant at approximately 25%. A direct calculation of Im(A_0) will be presented in Chapter 9. However, the unphysical kinematics that are used in

Table 8.13: *Experimental values of the components of Eq.* (2.22) *used in the determination of* $\mathrm{Im}\,A_0$*, together with the result for* $\mathrm{Im}A_2/\mathrm{Re}A_2$ *from this chapter.*

ϵ'/ϵ	$(1.65 \pm 0.26) \times 10^{-3}$
ω	0.04454(12)
$\lvert\epsilon\rvert$	$(2.228 \pm 0.011) \times 10^{-3}$
$\mathrm{Re}A_0$	$3.3201(18) \times 10^{-7}$ GeV
$\mathrm{Im}A_2/\mathrm{Re}A_2$ (lattice)	$-4.42(31)_{\mathrm{stat}}(89)_{\mathrm{syst}} \times 10^{-5}$

Chapter 9 mean that it is unfortunately not meaningful to compare this determination of $\mathrm{Im}A_0$ with the result of the direct calculation given in Eq. (9.15).

The ratio $\mathrm{Im}A_0/\mathrm{Re}A_0$ features in the parametrisation of the effect of direct CP-violation in $K_L \to \pi\pi$ on ϵ, customarily denoted by κ_ϵ [68]. If the result for $\mathrm{Im}A_0/\mathrm{Re}A_0$ given in Eq. (8.25) is used as input, the result is $(\kappa_\epsilon)_{\mathrm{abs}} = 0.924 \pm 0.006$. The subscript "abs" denotes that at present only the absorptive long-distance contribution (Im Γ_{12}) is included [69] (the error is now dominated by the experimental uncertainty in ϵ'/ϵ). The analogous contribution from the dispersive part (Im M_{12}) [69] is yet to be determined in lattice QCD, but progress towards being able to do this described in [70].

Using the lattice result for $\mathrm{Im}A_2$ in Eq. (8.11) and taking the experimental value given above for $\mathrm{Re}A_2$ from K^+ decays gives the electroweak penguin (EWP) contribution to ϵ'/ϵ, $\mathrm{Re}(\epsilon'/\epsilon)_{\mathrm{EWP}} = -(6.25 \pm 0.44_{\mathrm{stat}} \pm 1.19_{\mathrm{syst}}) \times 10^{-4}$ (the experimental value for the complete $\mathrm{Re}(\epsilon'/\epsilon)$ is $1.65(26) \times 10^{-3}$ [3]). Even though this contribution has been labelled EWP, and indeed it is dominated by the matrix element of the EWP operator $Q_{(8,8)_{\mathrm{mix}}}$, the result contains contributions from all three components to $\mathrm{Im}A_2$ in Eq. (8.23). The contribution from the two EWP operators $Q_{(8,8)}$ and $Q_{(8,8)_{\mathrm{mix}}}$ is $-(7.34 \pm 0.52_{\mathrm{stat}} \pm 1.39_{\mathrm{syst}}) \times 10^{-4}$.

This chapter ends with a brief comparison of an earlier result obtained using finite-energy sum rules [71], where the contribution to ϵ'/ϵ from the operator $Q_{(8,8)_{\mathrm{mix}}}$ (renormalised at 2 GeV) was found to be $-(11.0 \pm 3.6) \times 10^{-4}$.

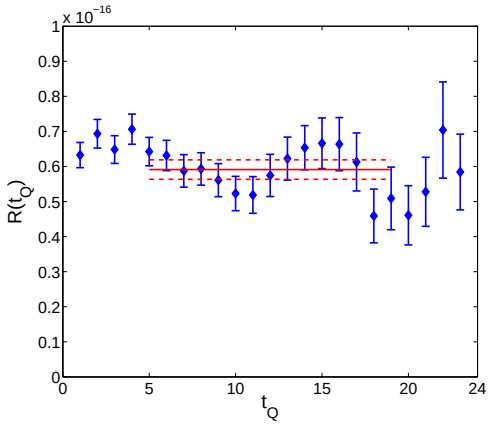

(a) $(27, 1)$ operator

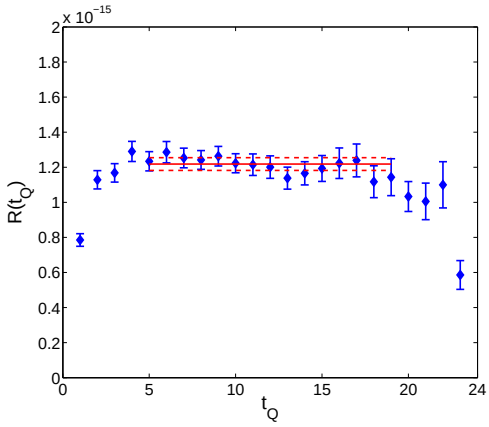

(b) $(8, 8)$ operator

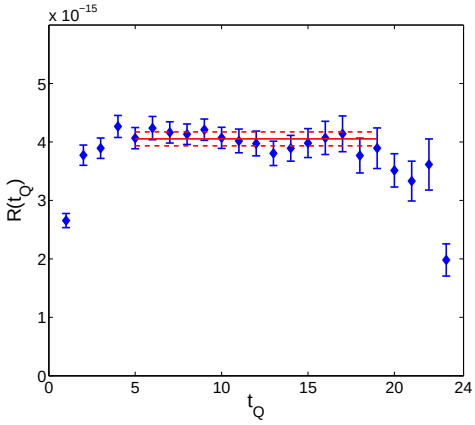

(c) $(8, 8)$mix operator

Figure 8.4: *The ratios defined in Eq. (8.4) for* $p = \sqrt{2}\pi/L$*. The two-pion source is at* $t = 0$ *while the kaon source is at* $t_K = 24$*. The dashed line shows the error on the fit*

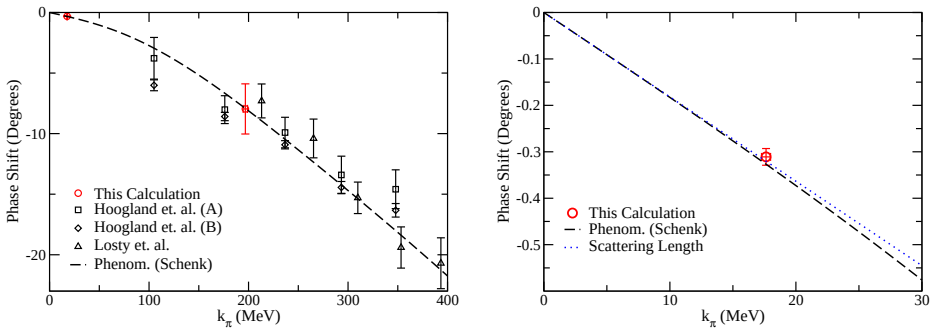

Figure 8.5: *Plots of the $I = 2$ two-pion s-wave phase shift against momentum k_π. The resutls of our calculation at $p = 0$ and $p = \sqrt{2}\pi/L$ are denoted by the red circles, and the dashed curve is the phenomenological representation from ref.[62]. The left-hand plot is a comparison of the calculated phase shift with experimental results [60, 61, 62]. The right-hand plot is a zoom into the small-k_π region, demonstrating the approximate linear behaviour of the phenomenological curve in the region of $p = 0$. The scattering length used in the straight (dotted) line is calculated using chiral perturbation theory [63].*

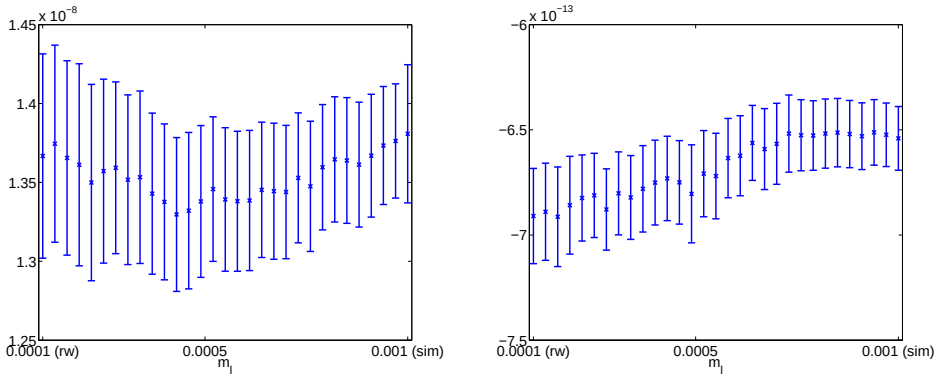

(a) Reweighting ReA_2 (b) Reweighting ImA_2

Figure 8.6: *Reweighting A_2 from $m_l^{\rm sea} = 0.001$ to $m_l^{\rm sea} = 0.0001$.*

Chapter 9

Evaluation of $K \to \pi\pi$ decay amplitudes on Iwasaki lattices

The main objective of this chapter is to calculate the $\Delta I = 1/2$ decay amplitude A_0. Recognising the difficulty of this problem, this calculation is performed on a lattice which is relatively small compared to the one used in the previous chapter, and a somewhat heavy pion mass ($m_\pi \approx 421\,\mathrm{MeV}$) is chosen so that large statistics can more easily be collected. The calculation is performed at threshold, where the kaon mass is approximately equal to the two-pion energy and the two final state pions are at rest. A complete evaluation of the $K \to \pi\pi$ matrix elements in the $I = 0$ channel has never been done before, and the results presented in this chapter represent a major breakthrough. A calculation of the $\Delta I = 3/2$ decay amplitude is included for comparison and completeness.

Although physical kinematics are not employed in this calculation, the final results for the complex amplitudes A_0 and A_2 are otherwise physical. The matrix elements are renormalised at 2.15 GeV in the $\overline{\mathrm{MS}}$ scheme using the techniques described in Chapter 5. Specifically, the renormalisation constants which are used can be found in Tab. 5.2.

Because of the unphysical, threshold kinematics and focus on controlling the statistical errors associated with the disconnected diagrams, no attempt is made to

Table 9.1: *Ensemble details. The analysis of this chapter is performed using a single Iwasaki enemble with* $\beta = 2.13$.

Lattice	β	am_h	am_l	number of trajectories
Iwasaki ($16^3 \times 32$)	2.13	0.032	0.01	800

estimate the size of possible systematic errors. The quoted errors on the results are statistical only. Similarly the systematic and statistical errors associated with the Rome-Southampton renormalisation factors have not been included. Both these sources of error could be made substantially smaller than the statistical errors when required.

9.1 Computational Details

This calculation uses the Iwasaki gauge action with $\beta = 2.13$ and 2+1 flavours of domain wall fermions (DWF). While the computational costs of DWF are much greater than those of Wilson or staggered fermions, as has been shown in earlier papers [72, 73, 20, 21], accurate chiral symmetry at short distances is critical to avoid extensive operator mixing, which would make the lattice treatment of $\Delta S = 1$ processes much more difficult.

The analysis of this chapter is performed on a single lattice ensemble with space-time volume $16^3 \times 32$, a fifth-dimensional extent of $L_s = 16$ and light and strange quark masses of $am_l = 0.01$, $am_s = 0.032$, respectively. This ensemble is similar to the $am_l = 0.01$ ensemble reported in Ref. [74] except for the use of the improved RHMC-II algorithm of Ref. [50] and a more physical value for the strange quark mass. The inverse lattice spacing for these input parameters was determined to be 1.73(3) GeV resulting in a lattice volume of $(1.83\text{ fm})^3$ and the residual mass is $am_{\text{res}} = 0.00308(4)$ [50]. The total number of configurations analysed is 800, each separated by 10 molecular dynamics time units. The Dirac operator is computed with anti-periodic boundary conditions in the time direction, and periodic boundary conditions in the space directions. The propagators are calculated using a Coulomb gauge fixed wall source (used for meson propagators) and a random wall source (used to calculate the loops in the *type*3 and *type*4 graphs shown in Figs. 7.5

and 7.6). The large statistics that are needed for a successful calculation are obtained by placing propagator sources on each of the 32 time slices in the lattice volume. These propagators are then used to create two-pion sources on every timeslice. The two-pion correlation functions are averaged over the common separations between the two-pion source and two-pion sink. This was made explicit in Eq. (7.10) for the type-V diagram in Sec. 7.1. Similarly in the case of $K \to \pi\pi$ correlation functions, the kaon source is created on all time slices, the time separation between the kaon and two pions is fixed and labelled Δ, and the correlation functions are averaged over all common separations between the kaon source and insertion of the weak operator at fixed Δ. For each time slice and source type, twelve inversions are required corresponding to the possible 3 colour and 4 spin choices for the source. Thus, a total of 768 inversions are performed for each quark mass on a given configuration. As will be shown below, this large number of inversions, performed on 800 configurations, provides the substantial statistics needed to resolve the real part of the $I = 0$ amplitude A_0 with 25% accuracy.

In order to obtain energy-conserving $K^0 \to \pi\pi$ decay amplitudes, the mass of the valence strange quark in the kaon is assigned a value different from that appearing in the fermion determinant used to generate the ensembles, *i.e.* the strange quark is partially quenched. Since the mass of the dynamical strange quark is expected to have a small effect on amplitudes of the sort considered here [50, 66], this use of partial quenching is appropriate for the purposes of this calculation. Valence strange quark masses are chosen to be $am_s = 0.066$, 0.099 and 0.165, which are labeled s0, s1 and s2 respectively.

9.2 Analysis

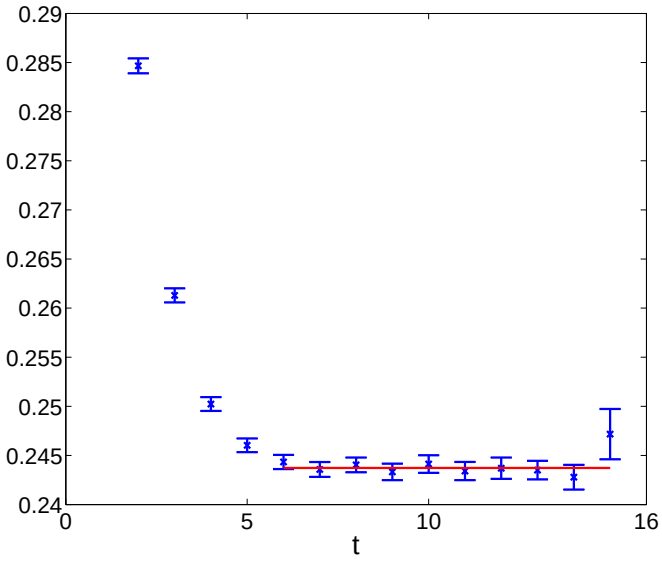

Figure 9.1: *Pion effective mass plot. The fitted mass is superimposed on the data.*

The simulated pion and kaon masses are measured by fitting the data to

$$C_K(t) \equiv \frac{1}{32}\sum_{t'=0}^{31}\left\langle O_K(t+t')O_K^\dagger(t')\right\rangle = Z_K^2\left(e^{-m_K t}+e^{-m_K(T-t)}\right) \quad (9.1)$$

$$C_\pi(t) \equiv \frac{1}{32}\sum_{t'=0}^{31}\left\langle O_\pi(t+t')O_\pi^\dagger(t')\right\rangle = Z_K^2\left(e^{-m_K t}+e^{-m_K(T-t)}\right) \quad (9.2)$$

where the average over different source positions for the propagators has been made explicit. This fit form is easy to understand based on Eq. (4.57). The results of the fits are shown in tables 9.2-9.3, and the corresponding effective mass plots are presented Figs. 9.1-9.2. Fit regions for all the fits in this chapter are shown in table 9.4. The simulated kaon masses can be used to interpolate to energy-conserving decay kinematics for both the $I = 2$ and $I = 0$ channels.

The two-pion correlation functions for isospin I and $I_z = 0$, defined in Eq. (7.8), are fit with the functional form

$$\frac{1}{32}\sum_{t'=0}^{31} C_I^{\pi\pi}(t+t',t') = Z_{\pi\pi,I}^2\left(e^{-E_I^{\pi\pi}t}+e^{-E_I^{\pi\pi}(T-t)}+A\right). \quad (9.3)$$

In this equation, the correlation function has been computed with two-pion sources on every time slice and averaged over common separations between source and sink.

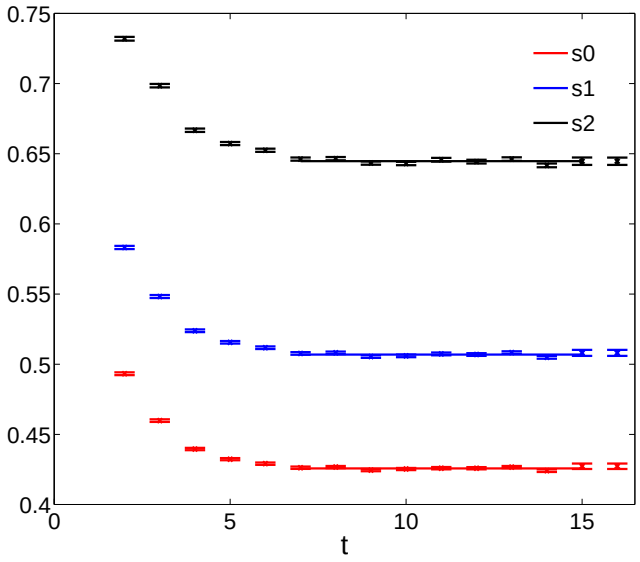

Figure 9.2: *Kaon effective masses, with fitted masses superimposed on the data. The legend indicates if valence strange-quark mass is* $am_s = 0.066$ *(s0),*$am_s = 0.099$ *(s1) or* $am_s = 0.165$ *(s2).*

The fitted energies are summarized in Tab. 9.2. In order to see clearly the effect of the disconnected graph, the calculation is also performed for the $I = 0$ channel without the disconnected graphs. This result is given in Tab. 9.2 with a label with an additional prime ($\prime$) symbol. The resulting effective mass plots for each case are shown in the right panel of Fig. 9.3. For comparison, a plot of twice the fitted pion mass is also shown. This figure clearly demonstrates that the two-pion interaction is attractive in the $I = 0$ channel with the finite volume, $I = 0$ $\pi - \pi$ energy $E_0^{\pi\pi}$ lower than $2m_\pi$. In contrast, the $I = 2$ channel is repulsive with $E_2^{\pi\pi}$ larger than $2m_\pi$. The fitted parameters $Z^2_{\pi\pi,I}$ and $E_I^{\pi\pi}$ will be used to extract weak matrix elements from the $K^0 \to \pi\pi$ correlation functions discussed below in which these same operators $O_I^{\pi\pi}(t)$ are used to construct the two-pion states.

Table 9.2: *Mass of pion and energies of the two-pion states. Here the subscript* $I = 0$ *or 2 on the* $\pi-\pi$ *energy,* $E_I^{\pi\pi}$*, labels the isospin of the state and* $E_0^{\pi\pi\prime}$ *represents the isospin zero, two-pion energy obtained when the disconnected graph V is ignored. The error in MeV is dominated by the lattice spacing.*

	m_π	$E_0^{\pi\pi}$	$E_0^{\pi\pi\prime}$	$E_2^{\pi\pi}$
lattice units	0.24373(47)	0.443(13)	0.4393(41)	0.5066(11)
MeV	422(30)	766(38)	760(31)	876(30)

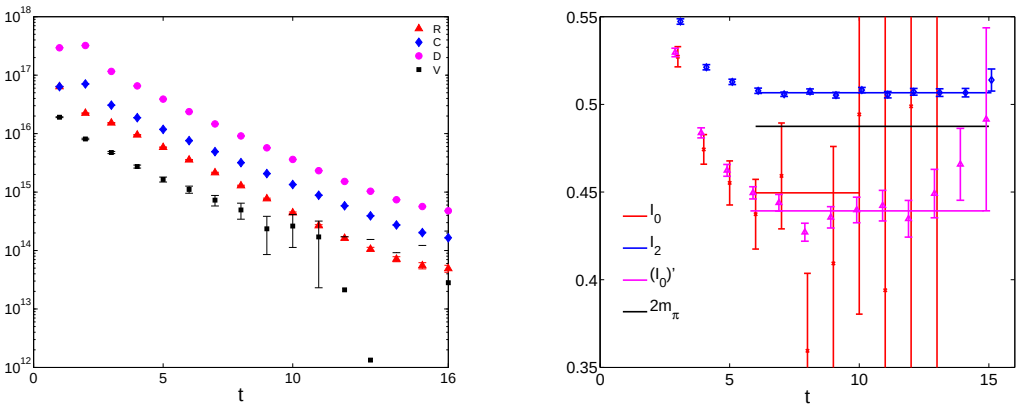

Figure 9.3: *Left: Results for the four types of contractions, direct D, C, R and V represented by the graphs in Fig. 7.1. Right: Effective mass plots for correlation functions for states with isospin two (I_2), isospin zero (I_0), isospin zero without the disconnected graph ($(I_0)'$) and twice the fitted pion mass ($2m_\pi$).*

Table 9.3: *Masses of the kaons.The superscript (s0), (s1) or (s2) on the kaon mass distinguishes our three choices of valence strange quark mass, $m_s = 0.066$, 0.099 and 0.165 respectively. The error in MeV is entirely dominated by the error on the lattice spacing.*

	$m_K^{(s0)}$	$m_K^{(s1)}$	$m_K^{(s2)}$
lattice units	0.42571(44)	0.50688(46)	0.64470(51)
MeV	736(30)	877(30)	1115(30)

9.2.1 $K^0 \to \pi\pi$ $\Delta I = 3/2$ amplitude

As Eq. (7.16) and the first column of Eq. (7.18) show, the $\Delta I = 3/2$ $K^0 \to \pi\pi$ decay amplitude includes only *type*1 contractions and four of the correlation functions are related:

$$A_{2,10} = A_{2,9} = \frac{3}{2}A_{2,1} = \frac{3}{2}A_{2,2}. \tag{9.4}$$

Table 9.4: *Fit regions on the Iwasaki lattices.*

pseudoscalar meson	fit region
kaon	7-15
pion	6-15
two-pion, $I0$	5-9
two-pion, $(I0)'$	6-15
two-pion, $I2$	6-15
$K \to \pi\pi$, $\Delta = 12$	5-7
$K \to \pi\pi$, $\Delta = 16$	5-11

Table 9.5: *Results for the lattice $\Delta I = 3/2$, $K \to \pi\pi$ transition amplitudes obtained from fitting the 3-point correlation functions to the functional form given in Eq.* (9.6) *for the six operators with $\Delta I = 3/2$ components. The second column gives the lattice matrix elements $M_i^{3/2,\mathrm{lat}}(\times 10^{-2})$ while the third and fourth column give their contributions to the real and imaginary parts of A_2. These results are for $\Delta = 12$ and $am_s = 0.099$.*

i	$M_i^{3/2,\mathrm{lat}}(\times 10^{-2})$	ReA_2(GeV)	ImA_2(GeV)
1	0.4892(16)	-1.724(9)e-08	0
2	$= M_1$	6.613(36)e-08	0
7	6.080(18)	2.677(15)e-11	4.498(25)e-14
8	21.26(6)	-2.148(12)e-10	-1.042(57)e-12
9	$=1.5M_1$	-4.974(27)e-15	5.133(28)e-13
10	$=1.5M_1$	6.055(33)e-12	-1.433(7)e-13
Total	-	4.871(31)e-08	-5.502(40)e-13

Therefore, it is sufficient to calculate $A_{2,1}$, $A_{2,7}$ and $A_{2,8}$ only. The corresponding three correlation functions, $C_{2,i}(\Delta, t)$ for $i = 1$, 7 and 8, with the choice of $m_K^{(1)}$ for the kaon mass, are shown in Fig. 9.4. The calculation of propagators with sources on each of the 32 time slices is exploited to compute $C_{2,i}(\Delta, t)$ from an average over all 32 source positions:

$$C_{2,i}(\Delta, t) = \frac{1}{32} \sum_{t'=0}^{31} A_{2,i}(t_\pi = t' + \Delta, t_{\mathrm{op}} = t + t', t_K = t'). \tag{9.5}$$

In Figs. 9.4(a)-9.4(c), $C_{2,i}(\Delta, t)$ for $0 < t < \Delta$ are plotted at fixed $\Delta = 12$ or 16. Tables 9.2 and 9.3 show that $m_K^{(s1)}$ is almost equal to the energy of $I = 2$, two-pion state, so the 3-point correlation function $C_{2,i}(\Delta, t)$ should be approximately independent of t in the central region where the time coordinate of the operator is far from both the kaon and the two-pion sources, $0 \ll t \ll \Delta$.

The correlators $C_{2,i}(\Delta, t)$ are fit using a single free parameter $M_i^{3/2,\mathrm{lat}}$:

$$C_{2,i}(\Delta, t) \quad = \quad M_i^{3/2,\mathrm{lat}} Z_{\pi\pi} Z_K e^{-E_{\pi\pi}\Delta} e^{-(m_K - E_{\pi\pi})t}, \tag{9.6}$$

where Z_K, m_K and $Z_{\pi\pi}$, $E_{\pi\pi}$ are determined from the fits in Eqns. (9.1) and (9.3). The fit regions for $C_{2,i}(\Delta, t)$ are $5 - 7$ for $\Delta = 12$ and $5 - 11$ for $\Delta = 16$. The fitted results for the matrix elements $M_i^{3/2,\mathrm{lat}}$ with $\Delta = 12$ and $am_s = 0.099$ are listed in Tab. 9.5 in lattice units.

Fits to the $K \to \pi\pi$, $I = 2$ correlators, $C_{2,i}(\Delta, t)$ for $i = 1, 7, 8$ and $\Delta = 12$ and 16 are compared in Figs 9.4(a)-9.4(c). In each plot the data are multiplied by a factor of $e^{E_{\pi\pi}\Delta}$, so that the results for $\Delta = 12$ and $\Delta = 16$ may be compared.

Figure 9.4 shows that for the operators Q_7 and Q_8 the larger separation, $\Delta = 16$, between the kaon source and two-pion sink gives a much shorter plateau region than the case $\Delta = 12$. This behavior is inconsistent with the usual expectation that it is the contributions from excited states of the kaon and pion, contributions which should be suppressed for larger Δ, that cause the poor plateau. An alternative, consistent explanation attributes the shortened plateau region seen for $\Delta = 16$ to the 'around-the-world' effect. This is the contribution to the correlation function in which the two-pion interpolating operator at the sink annihilates one pion and creates another (instead of annihilating two pions as in the $K \to \pi\pi$ contribution we are seeking) and the process at the weak operator is $K\pi \to \pi$ (instead of $K \to \pi\pi$). While one pion travels from the weak operator to the $\pi - \pi$ sink the second is created at the sink and travels forward in time, passing through the periodic boundary to reach the weak operator together with the kaon. The corresponding dominant path is shown in Fig. 9.10. The time dependence of the leading around-the-world behavior can be estimated as

$$\sim M_i^{3/2,\mathrm{lat}} Z_\pi^2 Z_K e^{-m_\pi T} e^{-(E_{K\pi} - m_\pi)t} \tag{9.7}$$

which is Δ independent but suppressed by the factor $\exp(-m_\pi T)$, where Z_π is the analogue of Z_K for the case of single pion production and $T = 32$ is the temporal extent of the lattice. In contrast, the physical contribution in Eq. (9.6) is suppressed by $\exp(-E_{\pi\pi}\Delta)$. Thus, the second, standard term falls with increasing Δ and the two factors are of similar size when $\Delta = T/2$. The expectation is that there will be a large contamination from such around-the-world effects in the $\Delta = 16$ case, consistent with Fig. 9.4.

The conclusion is that it is important to increase the lattice extent in the time direction both to suppress this around-the-world effect and to permit the use of a larger source-sink separation giving a longer plateau. Around-the-world effects will

Table 9.6: *The calculated quantities which appear in the Lellouch-Lüscher factor F for $I = 2$. The corresponding factor for the case of non-interacting particles is $F_{\text{free}} = 31.42$. The difference reflects the final two-pion scattering in a box.*

k	$q\frac{\partial\phi(q)}{\partial q}$	$k\frac{\partial\delta(k)}{\partial k}$	F
0.0690(13)	0.221(10)	-0.0849(43)	26.01(18)

be discussed again in the next section for the $\Delta I = 1/2$ kaon decay.

A good approximation to the infinite volume decay amplitude can be obtained by including the Lellouch-Lüscher factor, which was discussed in Chapter 6. The letter

$$F = \sqrt{8\pi \left(\frac{E_{\pi\pi}^2 m_K}{k^3}\right) \left\{ k\frac{\partial\delta_2(k)}{\partial k} + q\frac{\partial\phi(q)}{\partial q} \right\}}$$

will be used when quoting the results. Here k is defined through $E_{\pi\pi} = 2\sqrt{m_\pi^2 + k^2}$, $q = kL/2\pi$ and $\delta_2(k)$ is the s-wave, $I = 2$, $\pi - \pi$ scattering phase shift for pion relative momentum k. The $I = 2$ phase shift $\delta_2(k)$ is determined from the measured two-pion energy $E_{\pi\pi} = 0.5066(11)$ given in Tab. 9.2 and the finite volume quantization condition given in Eq. (6.1),

$$\phi(q) + \delta_2(p) = n\pi. \tag{9.8}$$

For this threshold case the integer n is set to zero which gives $\delta_2(k) = -0.0849(43)$. At small momentum k, the phase shift $\delta_2(k)$ is assumed to be a linear homogenous function of k. This allows the derivative of the phase shift to be evaluated by writing $\delta_2(k) = k\partial\delta_2(k)/\partial k$.

In the limit of non-interacting pions, the factor F becomes $F_{\text{free}}^2 = 2(2m_\pi)^2 m_K L^3$, which reflects the different normalization of states in a box and plane wave states in infinite volume. Results for F in this $I = 2$ case and the quantities used to determine it are given in Tab. 9.6. Applying the finite volume correction F gives a finite-volume corrected amplitude for a $\Delta I = 3/2$, $K \to \pi\pi$ decay that is slightly above threshold by the amount $E_2^{\pi\pi} - 2m_\pi = 33(1)$ MeV.

Table 9.7: *The complex, $K^0 \to \pi\pi$, $\Delta I = 3/2$ decay amplitudes in units of GeV.*

m_K	ReA_2	ImA_2
$m_K^{(s0)}$	4.234(23)($\times 10^{-8}$) GeV	-0.6386(39) ($\times 10^{-12}$)
$m_K^{(s1)}$	4.871(26)($\times 10^{-8}$) GeV	-0.6268(39) ($\times 10^{-12}$)
$m_K^{(s2)}$	5.935(33)($\times 10^{-8}$) GeV	-0.6087(39) ($\times 10^{-12}$)

The final expression for the $K^0 \to \pi\pi$ decay amplitudes is,

$$A_{2/0} = F\frac{G_F}{\sqrt{2}}V_{ud}V_{us}\sum_{i=1}^{10}\sum_{j=1}^{7}\left[\Big(z_i(\mu)+\tau y_i(\mu)\Big)Z_{ij}^{\text{lat}\to\overline{\text{MS}}}M_j^{\frac{3}{2}/\frac{1}{2},\text{lat}}\right], \tag{9.9}$$

where the matrix of renormalisation constants, Z_{ij} is given in Tab. 5.2 and the Wilson coefficients are given in Tab. 3.1. The results for the complex $\Delta I = 3/2$ decay amplitude A_2 are summarized in Tab. 9.7, including those for the other two, energy-non-conserving choices of kaon mass. Since $m_K^{(s1)}$ differs from the isospin-2 $\pi - \pi$ energy by only 0.2 percent, this case is quoted as the energy-conserving kaon decay amplitude. Therefore, in physical units, the energy-conserving $\Delta I = 3/2$, $K^0 \to \pi\pi$ complex, threshold decay amplitude for $m_K = 877$ MeV and $m_\pi = 422$ MeV is given by:

$$\text{Re}A_2 = 4.871(26)\times 10^{-8}\text{GeV} \tag{9.10}$$

$$\text{Im}A_2 = -0.6268(39)\times 10^{-12}\text{GeV}. \tag{9.11}$$

This result for ReA_2 can be compared with the experimental value of $1.479(3)\times 10^{-8}$ GeV given in Eq. (2.8). The larger result found in this calculation is likely explained by the unphysically heavy kaon and pions.

9.2.2 $K^0 \to \pi\pi$ $\Delta I = 1/2$ amplitude

Following the prescription given by Eq. (7.17), the $\Delta I = 1/2$ $K \to \pi\pi$ correlation functions,

$$C_{0,i}(\Delta, t) = \frac{1}{32}\sum_{t'=0}^{31} A_{0,i}(t_\pi = t' + \Delta, t_{\text{op}} = t + t', t_K = t'), \tag{9.12}$$

have been calculated for each of the ten effective weak operators. In the calculation each of these ten operators are treated as independent and the identities shown in Eq. (7.19) are then verified.

The calculation is also performed without the disconnected, *type*4 diagrams of Fig. 7.6, and these results are labeled with an additional prime symbol, as was the case for the two-pion correlation function without the disconnected V diagrams. Figures 9.5(a)- 9.7(d) show the resulting correlation functions for the operators Q_1 to Q_{10}, in the case of the lightest kaon $m_K^{(s0)}$ and a separation between the kaon and pions of $\Delta = 16$. Each figure compares the full calculation with the calculation where disconnected diagrams are not included. Tables 9.2 and 9.3 show that the mass of this kaon is very close to the energy of the I=0 two-pion state. Therefore, the plots are expected to show a reasonably flat plateau when the operator is far from both the source and sink.

Given this good agreement between the energies of the kaon and two-pion states, the unphysical, dimension three operator, $\overline{s}\gamma^5 d$ which mixes with the $(8,1)$ operators in Eq. (3.2) and is itself a total divergence, might be expected to also give a negligible contribution to such an energy and momentum conserving matrix element. However, as can be seen from Figs. 9.8(a) and 9.9(a), the matrix element of this term is large and the explicit subtraction described in Sec. 7.3 is necessary.

This difficulty is created by the combination of two phenomena. First the mixing coefficient which multiplies the $\overline{s}\gamma^5 d$ operator when it appears in our weak $(8,1)$ operators is large, of order $(m_s - m_l)/a^2$. Second, in this lattice calculation the necessary energy conserving kinematics (needed to ensure that this total divergence does not contribute) is only approximately valid. The required equality of the spatial momenta of the kaon and $\pi - \pi$ states is assured by our summing the location of the weak vertex over a complete temporal hyperplane. On the other hand, the equality of the energies of the initial and final states results only if we have adjusted the kaon mass to approximately that of the two-pion state and chosen the time extents sufficiently large that other states with different energies have been suppressed. However, as can be seen in Figs. 9.8(a) and 9.9(a) the

subtraction term $mix3$ shows strong dependence on the time at which it is evaluated. This implies that there are important contributions coming from initial and final states which have significantly different energies. One or both of these states is then not the intended K or $\pi - \pi$ state but instead an unwanted contribution which has been insufficiently suppressed by the time separations between source, weak operator and sink.

Thus, instead of relying on large time extents and energy conserving kinematics to suppress this unphysical, $O(1/a^2)$ term, it must explicitly be removed. As explained in Sec. 7.3 this can be done by including an explicit subtraction which is fixed by the requirement that the kaon to vacuum matrix element of the complete subtracted operator vanishes as in Eq. (7.23). Thus, the divergent coefficient of this mixing term is determined from the ratio $\alpha_i = \langle 0|Q_i|K\rangle / \langle 0|\overline{s}\gamma^5 d|K\rangle$ and then perform the explicit subtraction of the resulting terms, labeled $\alpha_i \cdot mix3$ and $\alpha_i \cdot mix4$ in Figs. 9.8 and 9.9. Imposing the condition that the kaon to vacuum matrix element of the complete subtracted operator vanishes also has the effect of removing the unwanted vacuum contribution to the $type4$ diagrams.

Of course, the finite part of such a subtraction is not determined from first principles and our choice, specified by Eq. (7.23) is arbitrary. Thus, we must rely on our identification of a plateau and the approximate energy conservation of our kinematics to make the arbitrary part of this subtraction small, along with the other errors associated with evaluating the decay matrix element of interest between initial and final states with slightly different energies.

The very visible time dependence in Figs. 9.8(a) and 9.9(a) for both the original matrix elements and the subtraction terms is now examined in greater detail. As discussed above one might expect these divergent subtraction terms to contribute to excited state matrix elements in which the energies of the initial and final states are very different. Typical terms should be exponentially suppressed as the separation between the weak operator and the source or sink is increased, with the time behavior $\exp\{-(m_K^* - m_K)t\}$ or $\exp\{-(E_{\pi\pi}^* - E_{\pi\pi})(\Delta - t)\}$, which ever is larger. (The $*$ denotes an excited state.) However, by carefully examining the time

behavior of the $mix3$ amplitude, we find that the time dependence, at least in the vicinity of the central region, is less rapid than might be expected from such excited states suggesting that it is probably not due primarily to contamination from excited states.

The most likely explanation is that the dominant, energy-nonconserving matrix elements which cause the significant time dependence in Figs. 9.8(a) and 9.9(a) arise from the around-the-world effects identified and discussed in the previous $\Delta I = 3/2$ section. In fact, for the reasons just discussed associated with divergent operator mixing, such around-the-world effects are a more serious problem in the $\Delta I = 1/2$ case. The dominant around-the-world graphs are shown in Fig. 9.11. An estimate of the time dependence of these graphs gives,

$$\begin{aligned} &\left\langle K^0\pi|Q_i|\pi\right\rangle Z_\pi Z_K Z_\pi e^{-m_\pi T} e^{-(E_{K\pi}-m_\pi)t} \\ &+ \left\langle 0|Q_i|K^0\pi\pi\right\rangle Z_\pi Z_K Z_\pi e^{-m_K((T-\Delta)+(\Delta-t))}\,, \end{aligned} \tag{9.13}$$

where the first term comes from the graphs in Figs. 9.11(a), 9.11(b), while the second term comes from Fig. 9.11(c). (Recall that $t = t_{\rm op} - t_K$ and $\Delta = t_\pi - t_K$). Notice that these two terms involve amplitudes which are far from energy conserving and therefore contain large divergent contributions from mixing with the operator $\overline{s}\gamma_5 d$ which will be removed only when combined with the corresponding around-the-world paths occuring in the $mix3$ contraction.

Thus the conclusion is that it is these around-the-world matrix elements which are the reason for the observed large divergent subtraction in the $type3$ graph. The largest divergent contribution is thus not the subtraction for the matrix element this calculation aims to evaluate, $\left\langle \pi\pi|Q_i|K^0\right\rangle$; rather, it is the divergent subtraction for the matrix elements $\left\langle K^0\pi|Q_i|\pi\right\rangle$ and $\left\langle 0|Q_i|K^0\pi\pi\right\rangle$ which arise from the around-the-world paths which are not sufficiently suppressed by the small lattice size. Two important lessons can be learned from this analysis. First, it is important to perform an explicit subtraction of the divergent mixing with the operator $\overline{s}\gamma_5 d$. While this term will not contribute to the energy conserving matrix element of interest, in a Euclidean space lattice calculation there are in general, other,

unwanted, energy non-conserving terms which may be uncomfortably large if this subtraction is not performed. Second it would be wise to work on a lattice with a much larger size T in time direction in order to suppress further the around-the-world terms which give such a large contribution in the present calculation. Using the average of propagators computed with periodic plus anti-periodic boundary conditions to effectively double the length in the time direction would be a good solution.

It should be emphasised that these divergent, around-the-world contributions do not pose a fundamental difficulty. The largest part of these amplitudes are removed by the corresponding subtraction terms constructed from the operator $\overline{s}\gamma_5 d$. The remaining finite contributions from this and other around-the-world terms are suppressed by the factor $\exp(-m_\pi T)$ or $\exp(-m_k(T-\Delta))$. The results suggest that the separation of $\Delta = 16$ gives a relatively longer plateau region, and so this is the $K - \pi\pi$ time separation that is used in the analysis below.

The lattice matrix elements are determined by fitting the $I = 1/2$ correlators $C_0^i(\Delta, t)$ given in Eq. (9.12) using the fitting form:

$$C_{0,i}(\Delta, t) \quad = \quad M_i^{1/2,\mathrm{lat}} Z_{\pi\pi} Z_K e^{-E_{\pi\pi}\Delta} e^{-(m_K - E_{\pi\pi})t}. \tag{9.14}$$

The fitted results for the weak, $\Delta I = 1/2$ matrix elements of all ten operators for $\Delta = 16$ are summarized in Tab. 9.8-9.10. To see the effects of the disconnected graph clearly, a second fit is performed to the amplitude from which the disconnected, *type*4 graphs have been omitted and the calculated results are shown with an additional $\prime$ label, as in the earlier two-pion scattering section.

The calculation of the $\Delta I = 1/2$ decay amplitude A_0 from the lattice matrix elements $M_i^{1/2,\mathrm{lat}}$ given in Tab. 9.8-9.10 is very similar to the $\Delta I = 3/2$ case: the values of $M_i^{1/2,\mathrm{lat}}$ are simply substituted in Eq. (9.9). However, the attractive character of the $I = 0$, $\pi - \pi$ interaction and resulting negative value of p^2 makes the Lellouch-Lüscher treatment of finite volume corrections inapplicable. For the repulsive $I = 2$ case, it was possible to apply this treatment to obtain the decay amplitude for a two-pion final state which was slightly above threshold

Table 9.8: *Fitted results for the weak, $\Delta I = 1/2$ kaon decay matrix elements using the kaon mass $m_K^{(s0)}$. The column $M_i^{\rm lat}$ shows the complete result from each operator. The column $M_i'^{\rm lat}$ shows the result when the disconnected graphs are omitted while the 4th and 5th columns show the contributions of each operator the real and imaginary parts of the physical decay amplitude A_0. These results are obtained using a source-sink separation $\Delta = 16$, and a fit range $5 \le t \le 11$.*

i	$M_i^{1/2,\rm lat}$	ReA_0(GeV)	ImA_0(GeV)
1	-0.0015(15)	$(7.6\pm6.4)\times10^{-8}$	0
2	0.00148(59)	$(2.86\pm0.97)\times10^{-7}$	0
3	-0.0003(41)	$(2.0\pm13.6)\times10^{-10}$	$(1.1\pm7.6)\times10^{-12}$
4	0.0027(32)	$(4.2\pm4.4)\times10^{-09}$	$(1.4\pm1.4)\times10^{-11}$
5	-0.0032(37)	$(\ 3.1\pm5.3)\times10^{-10}$	$(1.6\pm2.8)\times10^{-12}$
6	-0.0076(47)	$(-5.6\pm3.3)\times10^{-09}$	$(-3.3\pm2.0)\times10^{-11}$
7	0.0106(14)	$(5.2\pm1.2)\times10^{-11}$	$(8.8\pm2.0)\times10^{-14}$
8	0.0348(27)	$(-3.66\pm0.28)\times10^{-10}$	$(-1.78\pm0.14)\times10^{-12}$
9	-0.0021(11)	$(1.94\pm0.93)\times10^{-14}$	$(-2.00\pm0.96)\times10^{-12}$
10	0.0009(12)	$(1.2\pm1.1)\times10^{-11}$	$(-2.7\pm2.7)\times10^{-13}$
Total	-	$(3.60\pm0.78)\times10^{-7}$	$(-2.1\pm2.1)\times10^{-11}$
i	$M_i'^{1/2,\rm lat}$	ReA_0'(GeV)	ImA_0'(GeV)
1	-0.00107(36)	$(6.1\pm1.5)\times10^{-8}$	0
2	0.00187(15)	$(3.70\pm0.24)\times10^{-7}$	0
3	0.00029(95)	$(0.1\pm3.2)\times10^{-10}$	$(5.6\pm178)\times10^{-14}$
4	0.00324(76)	$(5.5\pm1.1)\times10^{-9}$	$(1.80\pm0.34)\times10^{-11}$
5	-0.00664(84)	$(5.7\pm1.2)\times10^{-10}$	$(3.0\pm6.4)\times10^{-12}$
6	-0.01911(92)	$(-1.376\pm0.067)\times10^{-8}$	$(-8.27\pm0.40)\times10^{-11}$
7	0.01483(41)	$(7.71\pm0.31)\times10^{-11}$	$(1.296\pm0.053)\times10^{-13}$
8	0.04613(99)	$(-4.85\pm0.11)\times10^{-10}$	$(-2.359\pm0.052)\times10^{-12}$
9	-0.00175(28)	$(1.76\pm0.23)\times10^{-14}$	$(-1.81\pm0.24)\times10^{-12}$
10	0.00121(28)	$(1.55\pm0.27)\times10^{-11}$	$(3.67\pm0.63)\times10^{-13}$
Total	-	$(4.23\pm0.20)\times10^{-7}$	$(-6.60\pm0.43)\times10^{-11}$

Table 9.9: *Fitted results for the weak, $\Delta I = 1/2$ kaon decay matrix elements using the kaon mass $m_K^{(s1)}$. The column $M_i^{\rm lat}$ shows the complete result from each operator. The column $M_i'^{\rm lat}$ shows the result when the disconnected graphs are omitted while the 4th and 5th columns show the contributions of each operator the real and imaginary parts of the physical decay amplitude A_0. These results are obtained using a source-sink separation $\Delta = 16$, and a fit range $5 \leq t \leq 11$.*

i	$M_i^{1/2,\rm lat}$	ReA_0(GeV)	ImA_0(GeV)
1	-0.0015(15)	(9.8±8.4)×10^{-8}	0
2	0.00148(59)	(3.5±1.3)×10^{-7}	0
3	-0.0003(41)	(0.7±1.7)×10^{-10}	(3.7±9.6)×10^{-12}
4	0.0027(32)	(3.8±5.5)×10^{-09}	(1.2±1.8)×10^{-11}
5	-0.0032(37)	(5.9±6.8)×10^{-10}	(3.1±3.5)×10^{-12}
6	-0.0076(47)	(-9.3±4.2)×10^{-09}	(-5.6±2.6)×10^{-11}
7	0.0106(14)	(5.9±1.4)×10^{-11}	(9.9±2.4)×10^{-14}
8	0.0348(27)	(-4.07±0.36)×10^{-10}	(-1.97±0.17)×10^{-12}
9	-0.0021(11)	(2.0±1.2)×10^{-14}	(-2.1±1.2)×10^{-12}
10	0.0009(12)	(2.0±1.3)×10^{-11}	(-4.7±3.2)×10^{-13}
Total	-	(4.5±1.0) ×10^{-7}	(-4.1 ± 2.6) ×10^{-11}
i	$M_i'^{1/2,\rm lat}$	ReA_0'(GeV)	ImA_0'(GeV)
1	-0.00107(36)	(7.0±1.8) ×10^{-8}	0
2	0.00187(15)	(4.27±0.29) ×10^{-7}	0
3	0.00029(95)	(-2.0±3.8) ×10^{-10}	(-1.1±2.1) ×10^{-14}
4	0.00324(76)	(7.1±1.2) ×10^{-9}	(2.34±0.41) ×10^{-11}
5	-0.00664(84)	(6.1±1.5) ×10^{-10}	(3.22±0.76) ×10^{-12}
6	-0.01911(92)	(-1.510±0.074) ×10^{-8}	(-9.49±0.44) ×10^{-11}
7	0.01483(41)	(8.14±0.37) ×10^{-11}	(1.367±0.062) ×10^{-13}
8	0.04613(99)	(-5.19±0.12) ×10^{-10}	(-2.517±0.056) ×10^{-12}
9	-0.00175(28)	(2.24±0.28) ×10^{-14}	(-2.31±0.29) ×10^{-12}
10	0.00121(28)	(1.50±0.31) ×10^{-11}	(3.57±0.74) ×10^{-13}
Total	-	(4.87±0.24) ×10^{-7}	(-7.45±0.47) ×10^{-11}

Table 9.10: *Fitted results for the weak, $\Delta I = 1/2$ kaon decay matrix elements using the kaon mass $m_K^{(s2)}$. The column $M_i^{\rm lat}$ shows the complete result from each operator. The column $M_i'^{\rm lat}$ shows the result when the disconnected graphs are omitted while the 4th and 5th columns show the contributions of each operator the real and imaginary parts of the physical decay amplitude A_0. These results are obtained using a source-sink separation $\Delta = 16$, and a fit range $5 \leq t \leq 11$.*

i	$M_i^{1/2,\rm lat}$	ReA_0(GeV)	ImA_0(GeV)
1	-0.0019(25)	$(1.2\pm1.3)\times10^{-7}$	0
2	0.00225(93)	$(5.4\pm1.9)\times10^{-7}$	0
3	-0.0011(63)	$(0.6\pm2.6)\times10^{-9}$	$(0.3\pm1.4)\times10^{-12}$
4	0.0031(50)	$(6.5\pm8.4)\times10^{-9}$	$(2.1\pm2.8)\times10^{-11}$
5	-0.0065(59)	$(0.7\pm1.0)\times10^{-9}$	$(3.9\pm5.4)\times10^{-12}$
6	-0.0170(71)	$(-1.52\pm0.62)\times10^{-9}$	$(-9.1\pm3.7)\times10^{-11}$
7	0.0108(20)	$(6.1\pm2.2)\times10^{-11}$	$(1.03\pm0.37)\times10^{-13}$
8	0.0371(36)	$(-4.81\pm0.46)\times10^{-10}$	$(-2.34\pm0.23)\times10^{-12}$
9	-0.0023(18)	$(4.4\pm2.8)\times10^{-14}$	$(-2.9\pm1.9)\times10^{-12}$
10	0.0018(18)	$(2.7\pm2.1)\times10^{-11}$	$(-6.4\pm4.9)\times10^{-13}$
Total	-	$(6.5\pm1.5)\times10^{-7}$	$(-6.8\pm3.9)\times10^{-11}$
i	$M_i'^{1/2,\rm lat}$	ReA_0'(GeV)	ImA_0'(GeV)
1	-0.00117(50)	$(8.3\pm2.6)\times10^{-8}$	0
2	0.00213(20)	$(5.13\pm0.40)\times10^{-7}$	0
3	0.0003(13)	$(0.2\pm5.4)\times10^{-10}$	$(0.1\pm3.0)\times10^{-12}$
4	0.0036(10)	$(7.5\pm1.8)\times10^{-9}$	$(2.46\pm0.58)\times10^{-11}$
5	-0.0076(12)	$(8.3\pm2.1)\times10^{-10}$	$(4.3\pm1.1)\times10^{-12}$
6	-0.0213(11)	$(-1.879\pm0.095)\times10^{-8}$	$(-1.128\pm0.057)\times10^{-11}$
7	0.01430(47)	$(9.21\pm0.47)\times10^{-11}$	$(1.547\pm0.080)\times10^{-13}$
8	0.04415(99)	$(-5.69\pm0.13)\times10^{-10}$	$(-2.771\pm0.064)\times10^{-12}$
9	-0.00194(37)	$(3.73\pm0.58)\times10^{-14}$	$(-2.44\pm0.38)\times10^{-12}$
10	0.00137(37)	$(2.19\pm0.44)\times10^{-11}$	$(5.2\pm1.0)\times10^{-13}$
Total	-	$(5.84\pm0.32)\times10^{-7}$	$(-8.94\pm0.47)\times10^{-11}$

corresponding to the actual finite volume kinematics. In the present case there is no corresponding infinite-volume decay into two pions below threshold and an unphysical increase of m_π to compensate for the finite volume $\pi - \pi$ attraction will introduce an $O(1/L^3)$ error in the decay amplitude of the same size as that which the Lellouch-Lüscher treatment corrects. Thus, for this $\Delta I = 1/2$ decay amplitude, the finite volume corrections are not included, and instead the free-field value for the factor F is used in Eq. (9.9).

Although it is not possible to consistently apply the Lellouch-Lüscher finite volume correction factor to improve the result for the $I = 0$, $K \to \pi\pi$ decay amplitude, it might still be possible to use the quantisation condition of Eq. (9.8) to determine the $I = 0$ $\pi - \pi$ scattering phase shift $\delta_0(k)$. Even though Eq. (9.8) can be analytically continued to imaginary values of the momentum k, its application for large negative k^2 is uncertain since the function $\phi(k)$ becomes ill defined. In fact, the value of k^2 sits very close to a singular point of $\phi(q)$. We believe this happens because the condition on the interaction range $R \ll L/2$ used to derive the quantization condition in Eq. (9.8) is not well satisfied for our small volume. This impediment to determining $\delta_0(p)$ will naturally disappear once we work with lighter pions in a larger volume.

The results for $\mathrm{Re}A_0$ and $\mathrm{Im}A_0$ are summarized in Tab. 9.11 and the individual contribution from each of the operators at $am_s = 0.066$ is detailed in the last two columns of Tab. 9.8. Within a large uncertainty Tab. 9.8 shows that the largest contribution to $\mathrm{Re}A_0$ comes from operator Q_2, and that to $\mathrm{Im}A_0$ from Q_6 as found, for example, in Refs. [20, 21].

Since the choice $m_K^{(s0)}$ for the kaon mass is not precisely equal to the energy of the $I = 0$ $\pi\pi$ state, a simple linear interpolation between $m_K^{(0)}$ and $m_K^{(s1)}$ is carried out to obtain an energy conserving matrix element, which is shown in the last row of Tab 9.11. In terms of physical units, therefore, our full calculation gives the energy conserving, $K^0 \to \pi\pi$, $\Delta I = 1/2$, complex decay amplitude A_0 for $m_K = 766$ MeV

Table 9.11: *Amplitudes for $\Delta I = 1/2$ $K^0 \to \pi\pi$ decay in units of GeV. The energy conserving amplitudes are obtained by a simple linear interpolation between $m_K^{(s0)}$=0.42599 and $m_K^{(s1)}$=0.50729 to the energy of two-pion state. As in the previous tables, the $\prime$ indicates results from which the disconnected graphs have been omitted.*

m_K	Re$A_0(\times 10^{-8})$	Re$A_0'(\times 10^{-8})$	Im$A_0(\times 10^{-12})$	Im$A_0'(\times 10^{-12})$
$m_K(s0)$	36.0(78)	42.3(20)	-21(21)	-66.1(43)
$m_K(s1)$	45(10)	48.8(24)	-41(26)	-74.6(47)
$m_K(s2)$	65(15)	58.4(32)	-68(39)	-89.4(63)
Energy conserving	38.0(82)	43.4(21)	-25(22)	-67.5(44)

Table 9.12: *Comparison of results between 400 and 800 configurations.*

# of configurations	Re$A_0(\times 10^{-8})$	Re$A_0'(\times 10^{-8})$	Im$A_0(\times 10^{-12})$	Im$A_0'(\times 10^{-12})$
400	27.2(72)	36.5(20)	-17(17)	-52.2(46)
800	36.0(78)	42.3(20)	-21(21)	-66.1(43)

and $m_\pi = 422$ MeV:

$$\mathrm{Re}A_0 = 3.80(82) \times 10^{-7}\mathrm{GeV} \quad (9.15)$$

$$\mathrm{Im}A_0 = -2.5(2.2) \times 10^{-11}\mathrm{GeV}. \quad (9.16)$$

These complete results can be compared with those obtained when the disconnected graphs are neglected given in Tab. 9.11 and the experimental value for $\mathrm{Re}A_0 = 3.3201(14) \times 10^{-7}$ GeV. As in the case of ReA_2, the larger value obtained in this calculation is likely the result of the unphysically heavy kaon and pion.

9.3 Discussion and Conclusions

Comparing the results of ReA_2 in Tab. 9.7 and ReA_0 in Tab. 9.11, the $\Delta I = 1/2$ enhancement ratio ReA_0/ReA_2 is found to be roughly 7-9. This comparison is degraded by the threshold kinematics which, since the $I = 0$ and $I = 2$ two-pion states have different energies in a finite volume, causes this calculation to use a different kaon mass in the calculations of A_2 and A_0 in order to have energy conserving decays in each case. These two energy conserving amplitudes have a ratio of 38.0/4.911 = 7.7, while if energy conservation is ignored and the same $m_K^{(1)}$ value for kaon mass are used, the ratio becomes 45.0/4.911 = 9.2. Of course, both

estimates are far from the experimental ratio of 22.5 suggesting that the 422 MeV pion mass, 736 and 877 MeV kaon masses and small lattice volume are far from physical.

For completeness, the measure of direct CP violation ϵ'/ϵ defined in Eq. (2.22) is evaluated. Using the threshold kinematics, the kaon mass $m_K^{(1)}$ and substituting the experimental value for ϵ, the result is $\mathrm{Re}(\epsilon'/\epsilon) = (2.7 \pm 2.6) \times 10^{-3}$. If the experimental value of $\omega = \mathrm{Re}A_2/\mathrm{Re}A_0$ is used instead, the result is $\mathrm{Re}(\epsilon'/\epsilon) = (1.11 \pm 0.91) \times 10^{-3}$.

This calculation is sufficiently far from physical kinematics that it is not appropriate to compare these results with experiment.[1] Instead, the objective of this calculation is to show how well the method performs. $\mathrm{Re}A_0$, the key element needed to explain the $\Delta I = 1/2$ rule, has been calculated successfully, with a 25% statistical error. Table 9.12 compares the results for $\mathrm{Re}A_0$ obtained on a sub-sample of 400 and all 800 configurations and shows that the statistical errors on the quantities measured scale approximately as $1/\sqrt{N}$. Therefore, we believe that the non-zero signal for $\mathrm{Re}A_0$ is real and that this statistical error could be reduced to 10 percent by quadrupling the size of our sample to 3200 configurations. It is interesting to note the results for primed (disconnected graphs omitted) and unprimed (all graphs included) quantities contributing to $\mathrm{Re}A_0$ have similar values suggesting that the disconnected graphs, while contributing significantly to the statistical error, have an effect on the final result for $\mathrm{Re}A_0$ at or below 25%.

In contrast, the result for $\mathrm{Im}A_0$ has an 80% error. Thus, it is not clear whether the size of the result will survive a quadrupling of the sample with its statistical error reducing to a 40% error or whether the result itself will shrink, remaining statistically consistent with zero. Considering the substantial systematic errors associated with the small volume and the fact that the kinematics are far from the physical, this trial calculation is presented as a guideline for future work and a proof of method rather than giving accurate numbers to compare with experiment.

[1] A further unphysical aspect of these kinematics is the inequality of the strange quark mass used in the fermion determinant and the self contractions appearing in the eye graphs ($m_s = 0.032$) and strange quark masses used in the valence propagator of the K meson ($m_s = 0.066$, 0.99 and 0.165).

From the observation of the around-the-world effect, the conclusion is that it is important to use the average of quark propagators obeying periodic and anti-periodic boundary conditions to extend the lattice size in the time direction. In addition, explicit subtraction of the divergent mixing term $\overline{s}\gamma^5 d$ is necessary even for kinematics which are literally energy conserving because the around-the-world path and possibly other excited state matrix elements are far off shell and can be substantially enhanced by such a divergent contribution. Finally, future work should be done using a much larger lattice which can contain two pions without any worry about finite size effects.

The focus of this chapter is on developing techniques capable of yielding statistically meaningful results from the challenging lattice correlation functions involved in the amplitude A_0. However, there are other important problems that will also require careful attention if physically meaningful results are to be obtained for this amplitude with an accuracy of better than 20%. Two important issues are associated with operator mixing. As discussed in Chapter 5.2, a proper treatment of the non-perturbative renormalisation of the four independent $(8,1)$ four-quark operators requires that additional operators containing gluonic variables (some of which are not gauge invariant) be included. While including such operators is in principle possible and the subject of active research, controlling such mixing using RI/MOM methods offers significant challenges.

A second problem is operator mixing induced by the residual chiral symmetry breaking of the DWF formulation. The mixing of such wrong-chirality operators should be suppressed by a factor of order $m_{\rm res}$. However, the $K \to \pi\pi$ matrix elements of the important $(8,1)$ four-quark operators are themselves suppressed by at least one power of m_K^2, a suppression that is absent from similar matrix elements of the induced, wrong-chirality operators. Therefore, such mixing has been ignored in this study because its effect on the matrix elements of interest are expected to be of order $m_{\rm res}/m_s \approx 0.08$, suggesting that these effects will be smaller than the 25% statistical errors. To perform a more accurate calculation in the future, these mixing effects may be further suppressed by adopting a gauge action with smaller residual chiral symmetry breaking. For example, this ratio reduces to 0.04 for the

IDSDR gauge action used in Chapter 8 and to 0.023 for those ensembles with the smallest lattice spacing created to date using the Iwasaki gauge action [51]. When greater accuracy is required either an improved fermion action, larger L_s or explicit subtraction of wrong-chirality mixing must be employed.

As lattice calculations move closer to the physical pion mass a further important difficulty must be overcome: giving physical relative momentum to the two pions. This can be accomplished while keeping the two-pion state in which we are interested as the ground state, if the kaon is given non-zero spatial momentum relative to the lattice. In this case the lowest energy final state can be arranged to have one pion at rest while the other pion carries the kaon momentum, as in the $\Delta I = 3/2$ calculation of Ref. [75]. However, this requires the momentum carried by the initial kaon and final pion to be 739 MeV, which is 5.4 times larger than the physical pion mass. Such a large spatial momentum will likely make the calculation extremely noisy. For the $\Delta I = 3/2$ calculation, it is possible to use anti-periodic boundary conditions in one or more spatial directions for one of the light quarks so that each pion necessarily carries the physical, 206 MeV momentum present in the actual decay while the kaon can be at rest [8, 76]. This is the strategy which was adopted in the previous chapter. However, this approach cannot be used in the case of the $I = 0$ final state being studied in this chapter. Instead, the use of G-parity boundary conditions [77] may be the solution to this problem.

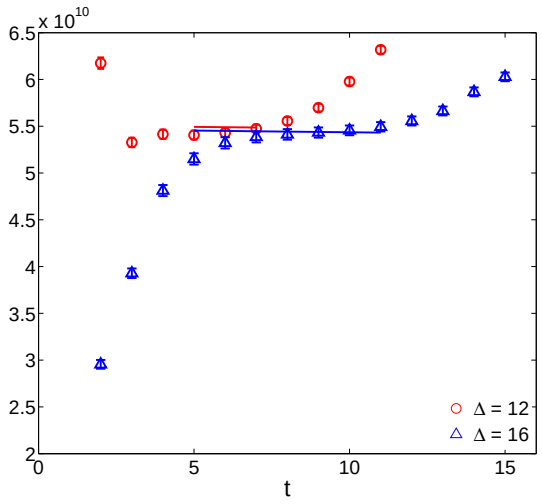

(a) Comparison of $C_{2,1}(12,t)\cdot e^{12E_{\pi\pi}}$ with $C_{2,1}(16,t)\cdot e^{16E_{\pi\pi}}$.

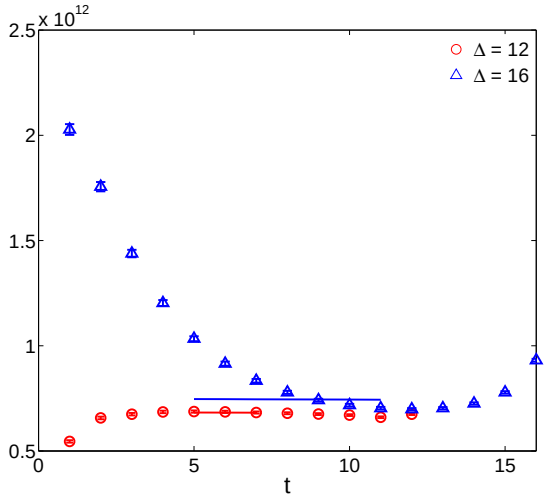

(b) Comparison of $C_{2,7}(12,t)\cdot e^{12E_{\pi\pi}}$ with $C_{2,7}(16,t)\cdot e^{16E_{\pi\pi}}$.

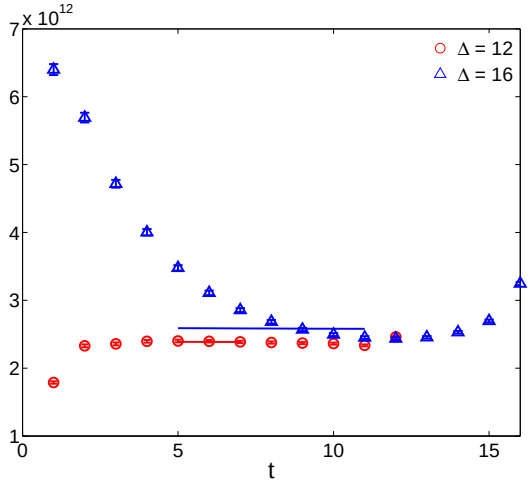

(c) Comparison of $C_{2,8}(12,t)\cdot e^{12E_{\pi\pi}}$ with $C_{2,8}(16,t)\cdot e^{16E_{\pi\pi}}$.

Figure 9.4: $\Delta I = 3/2$ $K \to \pi\pi$ *correlation functions with ams* $=$ 0.099. *The fit regions are 5-7 for* $\Delta = 12$ *and 5-11 for* $\Delta = 16$.

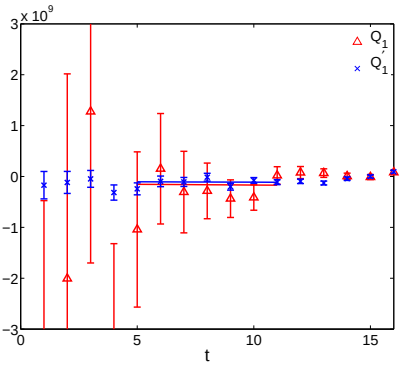

(a) $C_{0,1}(t,16)$

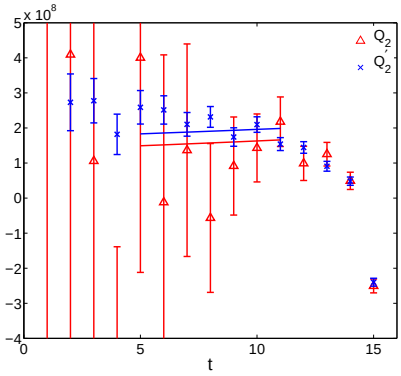

(b) $C_{0,2}(t,16)$

Figure 9.5: *$K \to \pi\pi$ correlation functions with $\Delta = 16$ and $am_s = 0.066$ with current-current operators.*

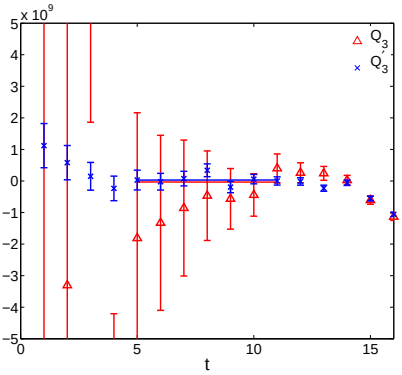

(a) $C_{0,3}(t,16)$

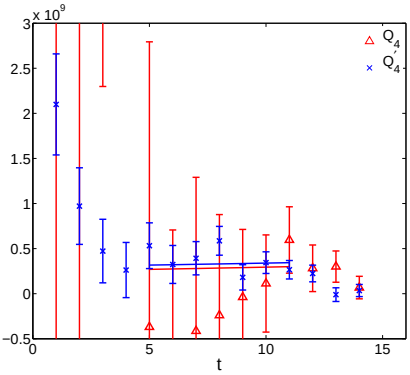

(b) $C_{0,4}(t,16)$

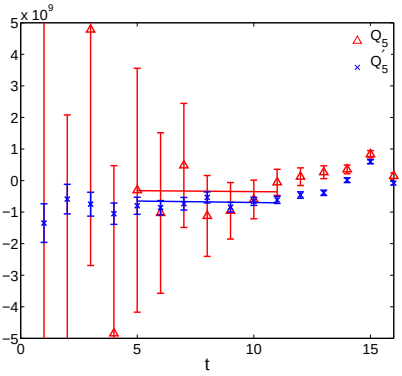

(c) $C_{0,5}(t,16)$

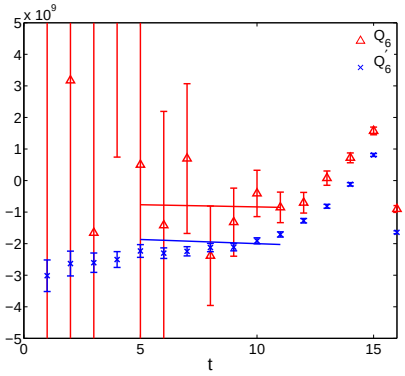

(d) $C_{0,6}(t,16)$

Figure 9.6: *$K \to \pi\pi$ correlation functions with $\Delta = 16$ and $am_s = 0.066$ with QCD-penguin operators.*

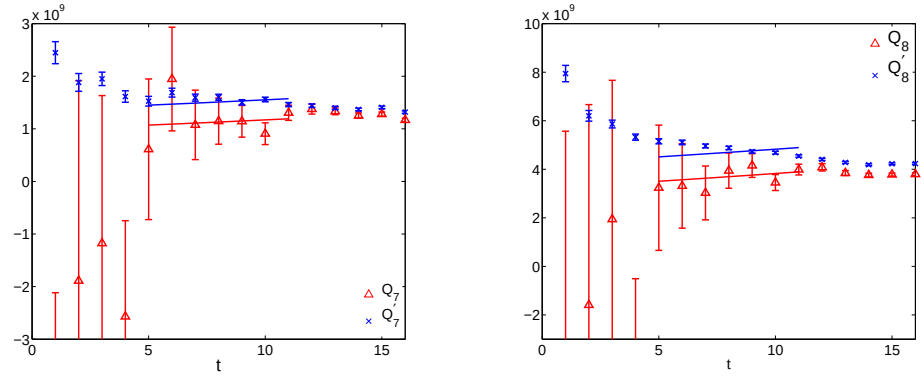

(a) $C_{0,7}(t, 16)$

(b) $C_{0,8}(t, 16)$

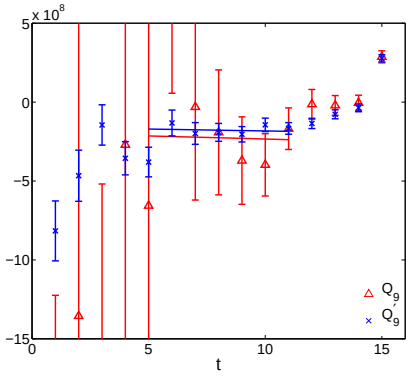

(c) $C_{0,9}(t, 16)$

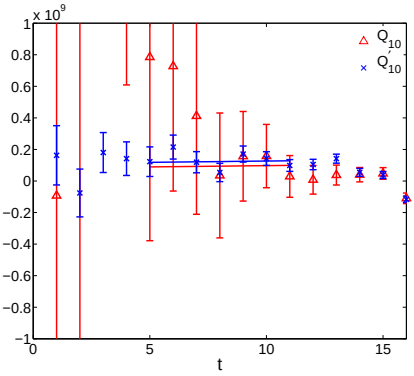

(d) $C_{0,10}(t, 16)$

Figure 9.7: *$K \to \pi\pi$ correlation functions with $\Delta = 16$, $am_s = 0.066$, and electroweak-penguin operators. Triangles indicate all four types of contraction are included, while crosses indicate that type4 diagrams have been omitted.*

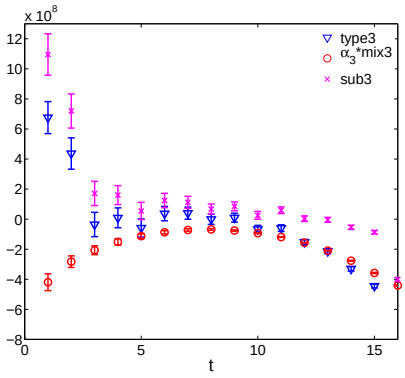

(a) $C_{0,2}(t,16)$ type3, subtraction of divergent term

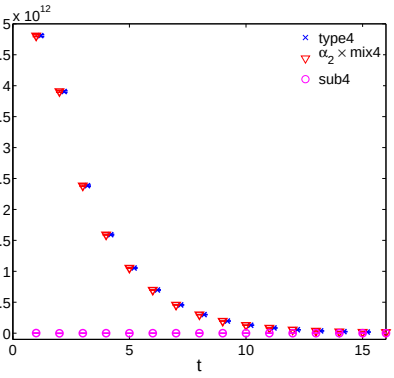

(b) $C_{0,2}(t,16)$ type4, subtraction of divergent term

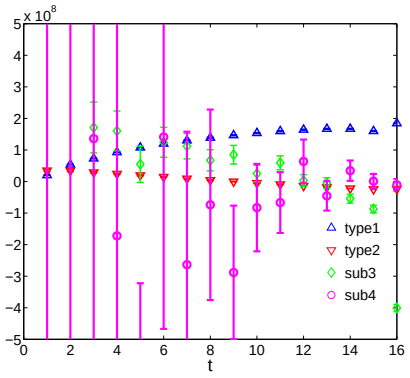

(c) Contributions to $C_{0,2}(t,16)$

Figure 9.8: *Terms contributing to* $C_{0,2}(t,16)$.

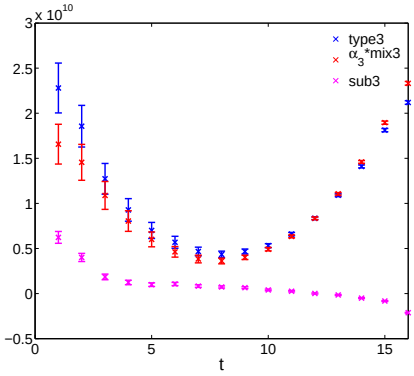

(a) $C_{0,6}(t,16)$ type3, subtraction of divergent term

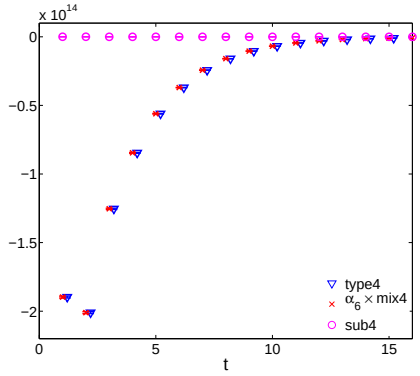

(b) $C_{0,6}(t,16)$ type4, subtraction of divergent term

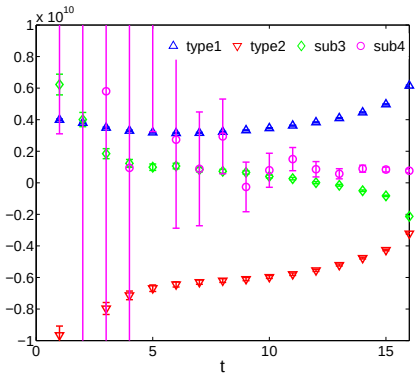

(c) Contributions to $C_{0,6}(t,16)$

Figure 9.9: *Terms contributing to* $C_{0,6}(t,16)$.

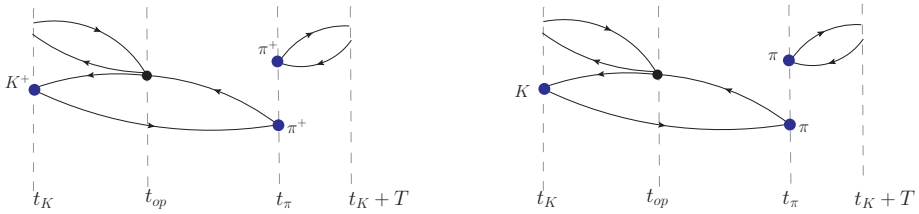

(a) (b)

Figure 9.10: *Leading around the world diagrams for type1* $K \to \pi\pi$ *decays.*

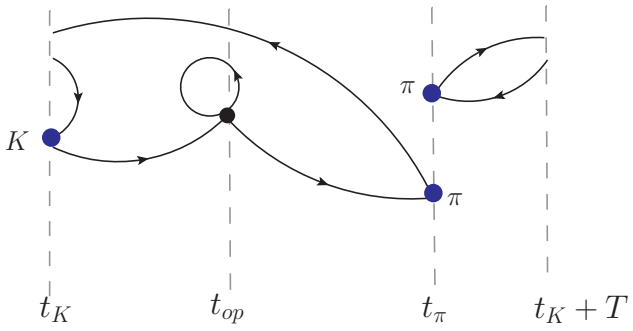

(a)

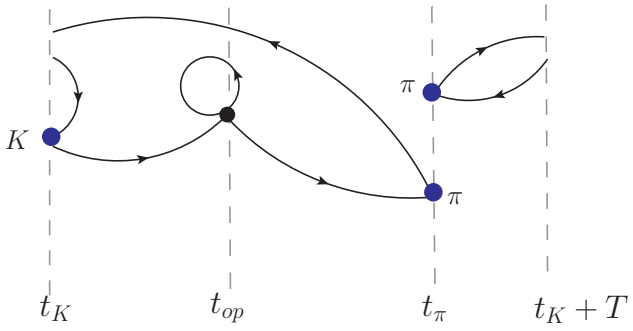

(b)

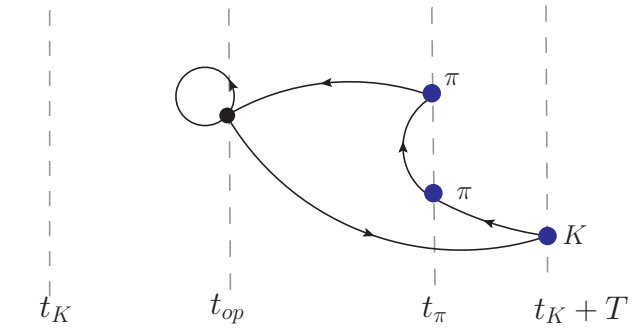

(c)

Figure 9.11: *Leading around the world diagrams for type3 $K \to \pi\pi$ decays.*

Chapter 10

Conclusions

This final chapter draws together the main conclusions from chapters 8 and 9.

In chapter 9, a first direct calculation of $\mathrm{Re}A_0$ was made, albeit at unphysical kinematics. The result, obtained at threshold and with a pion mass of ~ 420 MeV is $\mathrm{Re}A_0 = 3.80(82) \times 10^{-7}$ GeV. The imaginary part of the $\Delta I = 1/2$ decay amplitude was found to be $\mathrm{Im}A_0 = -2.5(2.2) \times 10^{-11}$ GeV. It has been demonstrated that it is possible to successfully evaluate the real part of the $\Delta I = 1/2$ decay amplitude. The unphysical kinematics mean, however, that it is not meaningful to compare this result with experiment. Improved statistical techniques, such as those proposed in [78] are needed in order to evaluate the imaginary part of $\mathrm{Im}A_0$ successfully. Further advancements, such as G-parity boundary conditions, must still be made before a calculation of A_0 may be made at physical kinematics.

The main result of this thesis was presented in chapter 8, where the $\Delta I = 3/2$ decay amplitude was evaluated at nearly-physical kinematics. All aspects of this calculation, including the operator renormalisation, finite volume corrections using the Lellouch-Lüscher and the momentum of the final-state pions is understood, and a full account of the remaining systematic errors was given. This calculation representes a major breakthrough. It is the first time that a direct determination of

ImA_2 had been made. The final result, evaluated at the simulated quark masses, is

$$\mathrm{Re}A_2 = 1.381(46)_{\mathrm{stat}}(258)_{\mathrm{syst}}\,10^{-8}\,\mathrm{GeV}, \quad \mathrm{Im}A_2 = -6.54(46)_{\mathrm{stat}}(120)_{\,\mathrm{syst}}\,10^{-13}\,\mathrm{GeV}\,. \tag{10.1}$$

With further advances in super-computing capabilities and continued research into G-parity boundary conditions, it should soon be possible to make a calculation of A_0 with a similar degree of precision and control over systematic uncertainties.

Appendix A

Expressions for $K \to \pi\pi$ contractions

A.1 $K^+ \to \pi^+\pi^+$ Contractions

$$D^+_{L\chi,1} = \Big\langle \mathrm{Tr}\Big\{\gamma_5 S^s(\vec{x}_{\rm op}, t_{\rm op}; t_K)^\dagger\ \gamma_L S^l_{\rm cos}(\vec{x}_{\rm op}, t_{\rm op}; t_\pi) S^l_W(t_K; t_\pi)^\dagger\Big\} \times \mathrm{Tr}\Big\{ S^l(\vec{x}_{\rm op} t_{\rm op}; t_\pi)^\dagger \gamma_5\gamma_\chi S^l_{\rm cos}(\vec{x}_{\rm op}, t_{\rm op}; t_\pi)\Big\}\Big\rangle \tag{A.1}$$

$$D^+_{L\chi,2} = \Big\langle \mathrm{Tr}\Big\{\gamma_5 S^s(\vec{x}_{\rm op}, t_{\rm op}; t_K)^\dagger\ \gamma_L S^l_{\rm cos}(\vec{x}_{\rm op}, t_{\rm op}; t_\pi) S^l_W(t_K; t_\pi)^\dagger\ \gamma_5\gamma_\chi \times S^l_{\rm cos}(\vec{x}_{\rm op}, t_{\rm op}; t_\pi)\ S^l(\vec{x}_{\rm op} t_{\rm op}; t_\pi)^\dagger\Big\}\Big\rangle \tag{A.2}$$

$$\tilde{D}^+_{LR,1} = \Big\langle \mathrm{Tr}_c\Big\{\mathrm{Tr}_s\Big[\gamma_L S^l_{\rm cos}(\vec{x}_{\rm op}, t_{\rm op}; t_\pi) S^l_W(t_K; t_\pi)^\dagger \gamma_5 S^s(\vec{x}_{\rm op}, t_{\rm op}; t_K)^\dagger \gamma_5\Big] \times \mathrm{Tr}_s\Big[S^l_{\rm cos}(\vec{x}_{\rm op}, t_{\rm op}; t_\pi)\ S^l(\vec{x}_{\rm op} t_{\rm op}; t_\pi)^\dagger \gamma_5\gamma_R\Big]\Big\}\Big\rangle \tag{A.3}$$

$$\tilde{D}^+_{LR,2} = \Big\langle \mathrm{Tr}_s\Big\{\mathrm{Tr}_c\Big[\gamma_L S^l_{\rm cos}(\vec{x}_{\rm op}, t_{\rm op}; t_\pi) S^l(\vec{x}_{\rm op} t_{\rm op}; t_\pi)^\dagger\ \gamma_5\Big] \mathrm{Tr}_c\Big[\gamma_R\ S^l_{\rm cos}(\vec{x}_{\rm op}, t_{\rm op}; t_\pi) S^l_W(t_K; t_\pi)^\dagger \gamma_5 S^s(\vec{x}_{\rm op}, t_{\rm op}; t_K)^\dagger \gamma_5\Big]\Big\}\Big\rangle \tag{A.4}$$

A.2 $K^0 \to \pi\pi$ Contractions

$$D_{LL,1}, D_{LR,1} = \pm \Big\langle \mathrm{Tr}\left\{\gamma_\mu(1-\gamma_5) S^l(\vec{x}_{\mathrm{op}}, t_{\mathrm{op}}; t_\pi) S^l(\vec{x}_{\mathrm{op}}, t_{\mathrm{op}}; t_\pi)^\dagger\right\} \times \mathrm{Tr}\left\{\gamma^\mu(1 \mp \gamma_5) S^l(\vec{x}_{\mathrm{op}}, t_{\mathrm{op}}; t_\pi)\gamma^5 S^l_W(t_\pi; t_K) S^s(\vec{x}_{\mathrm{op}}, t_{\mathrm{op}}; t_K)^\dagger\right\}\Big\rangle \tag{A.5}$$

$$\tilde{D}_{LL,1}, \tilde{D}_{LR,1} = \pm \Big\langle \mathrm{Tr}_c\left\{\mathrm{Tr}_s\left[\gamma_\mu(1-\gamma_5) S^l(\vec{x}_{\mathrm{op}}, t_{\mathrm{op}}; t_\pi)\gamma_5 S^l_W(t_\pi; t_K) S^s(\vec{x}_{\mathrm{op}}, t_{\mathrm{op}}; t_K)^\dagger\right] \times \mathrm{Tr}_s\left[S^l(\vec{x}_{\mathrm{op}}, t_{\mathrm{op}}; t_\pi) S^l(\vec{x}_{\mathrm{op}}, t_{\mathrm{op}}; t_\pi)^\dagger \gamma^\mu(1 \mp \gamma_5)\right]\right\}\Big\rangle \tag{A.6}$$

$$D_{LL,2}, D_{LR,2} = \pm \Big\langle \mathrm{Tr}\left\{\gamma_\mu(1-\gamma_5) S^l(\vec{x}_{\mathrm{op}}, t_{\mathrm{op}}; t_\pi) S^l(\vec{x}_{\mathrm{op}}, t_{\mathrm{op}}; t_\pi)^\dagger \gamma_\mu(1 \mp \gamma_5) S^l(\vec{x}_{\mathrm{op}}, t_{\mathrm{op}}; t_\pi) \gamma_5 S^l_W(t_\pi; t_K) S^s(\vec{x}_{\mathrm{op}}, t_{\mathrm{op}}; t_K)^\dagger\right\}\Big\rangle \tag{A.7}$$

$$\tilde{D}_{LL,2}, \tilde{D}_{LR,2} = \pm \Big\langle \mathrm{Tr}_s\left\{\mathrm{Tr}_c\left[S^l(\vec{x}_{\mathrm{op}}, t_{\mathrm{op}}; t_\pi) S^l(\vec{x}_{\mathrm{op}}, t_{\mathrm{op}}; t_\pi)^\dagger \gamma_\mu(1 \mp \gamma_5)\right] \times \mathrm{Tr}_c\left[S^l(\vec{x}_{\mathrm{op}}, t_{\mathrm{op}}; t_\pi)\gamma_5 S^l_W(t_\pi; t_K) S^s(\vec{x}_{\mathrm{op}}, t_{\mathrm{op}}; t_K)^\dagger \gamma_\mu(1-\gamma_5)\right]\right\}\Big\rangle \tag{A.8}$$

$$D_{LL,3}, D_{LR,3} = \pm \Big\langle \mathrm{Tr}\left\{S^s(\vec{x}_{\mathrm{op}}, t_{\mathrm{op}}; t_K)^\dagger \gamma_\mu(1-\gamma_5) S^l(\vec{x}_{\mathrm{op}}, t_{\mathrm{op}}; t_K)\right\} \times \left\{\gamma_\mu(1 \mp \gamma_5) S^l(\vec{x}_{\mathrm{op}}, t_{\mathrm{op}}; t_\pi)\gamma_5 S^l_W(t_\pi; t_\pi) S^l(\vec{x}_{\mathrm{op}}, t_{\mathrm{op}}; t_\pi)^\dagger\right\}\Big\rangle \tag{A.9}$$

$$\tilde{D}_{LL,3}, \tilde{D}_{LR,3} = \pm \Big\langle \mathrm{Tr}_c\left\{\mathrm{Tr}_s\left[\gamma_\mu(1-\gamma_5) S^l(\vec{x}_{\mathrm{op}}, t_{\mathrm{op}}; t_K) S^s(\vec{x}_{\mathrm{op}}, t_{\mathrm{op}}; t_K)^\dagger\right] \times \mathrm{Tr}_s\left[S^l(\vec{x}_{\mathrm{op}}, t_{\mathrm{op}}; t_\pi)\gamma_5 S^l_W(t_\pi; t_\pi) S^l(\vec{x}_{\mathrm{op}}, t_{\mathrm{op}}; t_\pi)^\dagger \gamma_\mu(1 \mp \gamma_5)\right]\right\}\Big\rangle \tag{A.10}$$

$$D_{LL,4}, D_{LR,4} = \pm \Big\langle \mathrm{Tr} \Big\{ S^s(\vec{x}_{\mathrm{op}}, t_{\mathrm{op}}; t_K)^\dagger \gamma_\mu (1-\gamma_5) S^l(\vec{x}_{\mathrm{op}}, t_{\mathrm{op}}; t_\pi) \gamma_5 S^l_W(t_\pi; t_\pi) \\ S^l(\vec{x}_{\mathrm{op}}, t_{\mathrm{op}}; t_\pi)^\dagger \gamma_\mu (1 \mp \gamma_5) S^l(\vec{x}_{\mathrm{op}}, t_{\mathrm{op}}; t_K) \Big\} \Big\rangle \tag{A.11}$$

$$\tilde{D}_{LL,4}, \tilde{D}_{LR,4} = \pm \Big\langle \mathrm{Tr}_s \Big\{ \mathrm{Tr}_c \Big[S^l(\vec{x}_{\mathrm{op}}, t_{\mathrm{op}}; t_K) S^s(\vec{x}_{\mathrm{op}}, t_{\mathrm{op}}; t_K)^\dagger \Big] \\ \mathrm{Tr}_c \Big[\gamma_\mu (1-\gamma_5) S^l(\vec{x}_{\mathrm{op}}, t_{\mathrm{op}}; t_\pi) \gamma_5 S^l_W(t_\pi; t_\pi) S^l(\vec{x}_{\mathrm{op}}, t_{\mathrm{op}}; t_\pi)^\dagger \gamma_\mu (1 \mp \gamma_5) \Big] \Big\} \Big\rangle \tag{A.12}$$

$$D^{(l)}_{LL,5}, D^{(l)}_{LR,5} = \pm \Big\langle \mathrm{Tr} \Big\{ \gamma_\mu (1 \mp \gamma_5) S^l_R(\vec{x}_{\mathrm{op}}, t_{\mathrm{op}}; t_{\mathrm{op}}) \Big\} \eta(x_{\mathrm{op}})^* \times \mathrm{Tr} \Big\{ \gamma^\mu (1-\gamma_5) S^l(x_{\mathrm{op}}, t_\pi) \times \\ S^l_W(t_\pi, t_\pi)^\dagger S^l_W(t_\pi; t_K) S^s(\vec{x}_{\mathrm{op}}, t_{\mathrm{op}}; t_K)^\dagger \Big\} \Big\rangle \tag{A.13}$$

$$\tilde{D}^{(l)}_{LL,5}, \tilde{D}^{(l)}_{LR,5} = \pm \Big\langle \mathrm{Tr}_c \Big\{ \mathrm{Tr}_s \Big[S^l(x_{\mathrm{op}}, t_\pi) S^l_W(t_\pi, t_\pi)^\dagger S^l_W(t_\pi; t_K) S^s(\vec{x}_{\mathrm{op}}, t_{\mathrm{op}}; t_K)^\dagger \gamma^\mu (1-\gamma_5) \Big] \times \\ \mathrm{Tr}_s \Big[S^l_R(\vec{x}_{\mathrm{op}}, t_{\mathrm{op}}; t_{\mathrm{op}}) \eta(x_{\mathrm{op}})^* \gamma_\mu (1 \mp \gamma_5) \Big] \Big\} \Big\rangle \tag{A.14}$$

$$D^{(s)}_{LL,5}, D^{(s)}_{LR,5} = \pm \Big\langle \mathrm{Tr} \left\{ \gamma_\mu (1 \mp \gamma_5) S^s_R(x_{\mathrm{op}}, t_{\mathrm{op}}) \right\} \eta(x_{\mathrm{op}})^* \times \mathrm{Tr} \Big\{ \gamma^\mu (1-\gamma_5) S^l(x_{\mathrm{op}}, t_\pi) \times \\ S^l_W(t_\pi; t_\pi)^\dagger S^l(t_\pi; t_K) S^s(x_{\mathrm{op}}, t_K)^\dagger \Big\} \Big\rangle \tag{A.15}$$

$$\tilde{D}^{(s)}_{LL,5}, \tilde{D}^{(s)}_{LR,5} = \pm \Big\langle \mathrm{Tr}_c \Big\{ \mathrm{Tr}_s \Big[S^l(x_{\mathrm{op}}, t_\pi) S^l_W(t_\pi, t_\pi)^\dagger S^l_W(t_\pi; t_K) S^s(\vec{x}_{\mathrm{op}}, t_{\mathrm{op}}; t_K)^\dagger \gamma^\mu (1-\gamma_5) \Big] \times \\ \mathrm{Tr}_s \Big[S^s_R(\vec{x}_{\mathrm{op}}, t_{\mathrm{op}}; t_{\mathrm{op}}) \eta(x_{\mathrm{op}})^* \gamma_\mu (1 \mp \gamma_5) \quad \Big] \Big\} \Big\rangle \tag{A.16}$$

$$D^{(l)}_{LL,6}, D^{(l)}_{LR,6} = \pm \Big\langle \mathrm{Tr} \Big\{ S^l_R(x_{\rm op}, t_{\rm op}) \eta(x_{\rm op})^* \gamma^\mu (1 \mp \gamma_5) \times S^l(\vec{x}_{\rm op}, t_{\rm op}; t_\pi) S^l_W(t_\pi, t_\pi)^\dagger S^l_W(t_\pi; t_K) S^s(x_{\rm op}, t_K)^\dagger \gamma^\mu (1 - \gamma_5) \Big\} \Big\rangle \tag{A.17}$$

$$\tilde{D}^{(l)}_{LL,6}, \tilde{D}^{(l)}_{LR,6} = \pm \Big\langle \mathrm{Tr}_s \Big\{ \mathrm{Tr}_c \Big[S^l_R(x_{\rm op}, t_{\rm op}) \eta(x_{\rm op})^* \gamma^\mu (1 \mp \gamma_5) \Big] \times \mathrm{Tr}_c \Big[S^l(\vec{x}_{\rm op}, t_{\rm op}; t_\pi) S^l_W(t_\pi, t_\pi)^\dagger S^l_W(t_\pi; t_K) S^s(x_{\rm op}, t_K)^\dagger \gamma^\mu (1 - \gamma_5) \Big] \Big\} \Big\rangle \tag{A.18}$$

$$D^{(s)}_{LL,6}, D^{(s)}_{LR,6} = \pm \langle \mathrm{Tr} \{ S^s_R(x_{\rm op}, t_{\rm op}) \eta(x_{\rm op})^* \ \gamma^\mu (1 - \gamma_5) \times S^l(\vec{x}_{\rm op}, t_{\rm op}; t_\pi) S^l_W(t_\pi, t_\pi)^\dagger S^l_W(t_\pi; t_K) S^s(x_{\rm op}, t_K)^\dagger \gamma^\mu (1 \mp \gamma_5) \Big\} \Big\rangle \tag{A.19}$$

$$\tilde{D}^{(s)}_{LL,6}, \tilde{D}^{(s)}_{LR,6} = \pm \langle \mathrm{Tr}_s \{ \mathrm{Tr}_c [S^s_R(x_{\rm op}, t_{\rm op}) \eta(x_{\rm op})^* \gamma^\mu (1 \mp \gamma_5)] \times \mathrm{Tr}_c \Big[S^l(\vec{x}_{\rm op}, t_{\rm op}; t_\pi) S^l_W(t_\pi, t_\pi)^\dagger S^l_W(t_\pi; t_K) S^s(x_{\rm op}, t_K)^\dagger \gamma^\mu (1 - \gamma_5) \Big] \Big\} \Big\rangle \tag{A.20}$$

$$D^{(l)}_{LL,7}, D^{(l)}_{LR,7} = \pm \Big\langle \mathrm{Tr} \Big\{ S^l_R(x_{\rm op}, t_{\rm op}) \eta(x_{\rm op})^* \gamma^\mu (1 \mp \gamma_5) \Big\} \times \mathrm{Tr} \Big\{ S^l(\vec{x}_{\rm op}, t_{\rm op}; t_K) S^s(x_{\rm op}, t_K)^\dagger \gamma^\mu (1 - \gamma_5) \Big\} \mathrm{Tr} \Big\{ S^l_W(t_\pi, t_\pi)^\dagger S^l_W(t_\pi, t_\pi) \Big\} \Big\rangle \tag{A.21}$$

$$\tilde{D}^{(l)}_{LL,7}, \tilde{D}^{(l)}_{LR,7} = \pm \Big\langle \mathrm{Tr}_c \Big\{ \mathrm{Tr}_s \Big[S^l_R(x_{\rm op}, t_{\rm op}) \eta(x_{\rm op})^* \gamma^\mu (1 \mp \gamma_5) \Big] \times \mathrm{Tr}_s \Big[S^l(\vec{x}_{\rm op}, t_{\rm op}; t_K) S^s(x_{\rm op}, t_K)^\dagger \gamma^\mu (1 - \gamma_5) \Big] \Big\} \times \mathrm{Tr} \Big\{ S^l_W(t_\pi, t_\pi)^\dagger S^l_W(t_\pi, t_\pi) \Big\} \Big\rangle \tag{A.22}$$

$$D^{(s)}_{LL,7}, D^{(s)}_{LR,7} = \pm \Big\langle \mathrm{Tr}\left\{ S^s_R(x_{\rm op}, t_{\rm op})\eta(x_{\rm op})^* \gamma^\mu (1 \mp \gamma_5) \quad \right\} \times \\ \mathrm{Tr}\left\{ S^l(\vec{x}_{\rm op}, t_{\rm op}; t_K) S^s(x_{\rm op}, t_K)^\dagger \gamma^\mu (1-\gamma_5) \right\} \times \mathrm{Tr}\left\{ S^l_W(t_\pi, t_\pi)^\dagger S^l_W(t_\pi, t_\pi) \right\} \Big\rangle \tag{A.23}$$

$$\tilde{D}^{(s)}_{LL,7}, \tilde{D}^{(s)}_{LR,7} = \pm \langle \mathrm{Tr}_c \left\{ \mathrm{Tr}_s \left[S^s_R(x_{\rm op}, t_{\rm op})\eta(x_{\rm op})^* \gamma^\mu (1 \mp \gamma_5) \right] \times \right. \\ \left. \mathrm{Tr}_s \left[S^l(\vec{x}_{\rm op}, t_{\rm op}; t_K) S^s(x_{\rm op}, t_K)^\dagger \gamma^\mu (1-\gamma_5) \right] \right\} \times \mathrm{Tr}\left\{ S^l_W(t_\pi, t_\pi)^\dagger S^l_W(t_\pi, t_\pi) \right\} \Big\rangle \tag{A.24}$$

$$D^{(l)}_{LL,8}, D^{(l)}_{LR,8} = \pm \Big\langle \mathrm{Tr}\left\{ S^l(\vec{x}_{\rm op}, t_{\rm op}; t_K) S^s(x_{\rm op}, t_K)^\dagger \gamma^\mu (1-\gamma_5) S^l_R(x_{\rm op}, t_{\rm op})\eta(x_{\rm op})^* \times \right. \\ \left. \gamma^\mu (1 \mp \gamma_5) \right\} \times \mathrm{Tr}\left\{ S^l_W(t_\pi, t_\pi)^\dagger S^l_W(t_\pi, t_\pi) \right\} \Big\rangle \tag{A.25}$$

$$\tilde{D}^{(l)}_{LL,8}, \tilde{D}^{(l)}_{LR,8} = \pm \Big\langle \mathrm{Tr}_s \left\{ \mathrm{Tr}_c \left[S^l(\vec{x}_{\rm op}, t_{\rm op}; t_K) S^s(x_{\rm op}, t_K)^\dagger \gamma^\mu (1-\gamma_5) \right] \times \right. \\ \left. \mathrm{Tr}_c \left[S^l_R(x_{\rm op}, t_{\rm op})\eta(x_{\rm op})^* \gamma^\mu (1 \mp \gamma_5) \right] \right\} \times \mathrm{Tr}\left\{ S^l_W(t_\pi, t_\pi)^\dagger S^l_W(t_\pi, t_\pi) \right\} \Big\rangle \tag{A.26}$$

$$D^{(s)}_{LL,8}, D^{(s)}_{LR,8} = \pm \Big\langle \mathrm{Tr}\left\{ S^l(\vec{x}_{\rm op}, t_{\rm op}; t_K) S^s(x_{\rm op}, t_K)^\dagger \gamma^\mu (1 \mp \gamma_5) S^s_R(x_{\rm op}, t_{\rm op})\eta(x_{\rm op})^* \times \right. \\ \left. \gamma^\mu (1-\gamma_5) \right\} \times \mathrm{Tr}\left\{ S^l_W(t_\pi, t_\pi)^\dagger S^l_W(t_\pi, t_\pi) \right\} \Big\rangle \tag{A.27}$$

$$\tilde{D}^{(s)}_{LL,8}, \tilde{D}^{(s)}_{LR,8} = \pm \Big\langle \mathrm{Tr}_s \left\{ \mathrm{Tr}_c \left[S^l(\vec{x}_{\rm op}, t_{\rm op}; t_K) S^s(x_{\rm op}, t_K)^\dagger \gamma^\mu (1 \mp \gamma_5) \right] \times \right. \\ \left. \mathrm{Tr}_c \left[S^s_R(x_{\rm op}, t_{\rm op})\eta(x_{\rm op})^* \gamma^\mu (1-\gamma_5) \right] \right\} \times \mathrm{Tr}\left\{ S^l_W(t_\pi, t_\pi)^\dagger S^l_W(t_\pi, t_\pi) \right\} \Big\rangle \tag{A.28}$$

Appendix B

Quotient Plots for $\Delta I = 3/2$ $K \to \pi\pi$ Matrix Elements

The quotient defined in Eq. (8.4) is plotted for $t_K - t_{\pi\pi} = 20, 28$ and 32. These plots are intended to supplement those shown in Fig. 8.4.

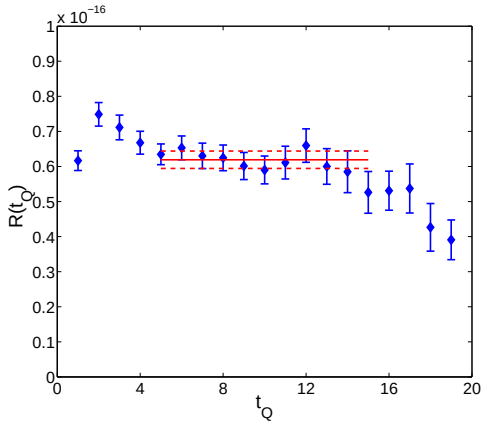

(a) $(27, 1)$ operator

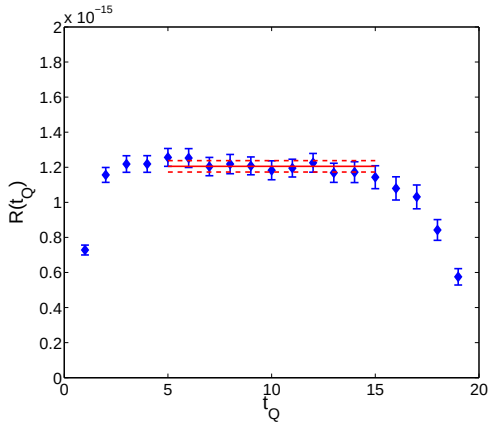

(b) $(8, 8)$ operator

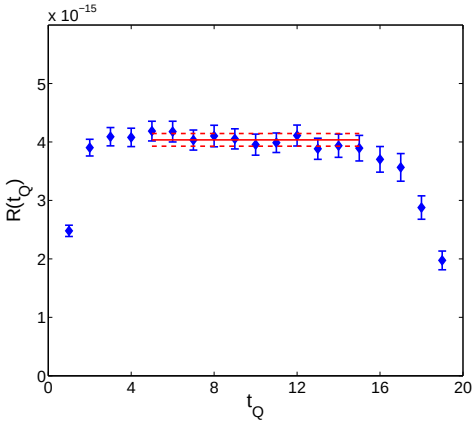

(c) $(8, 8)$mix operator

Figure B.1: *The ratios defined in Eq. (8.4) for* $p = \sqrt{2}\pi/L$. *The two-pion source is at* $t = 0$ *while the kaon source is at* $t_K = 20$. *The dashed line shows the error on the fit*

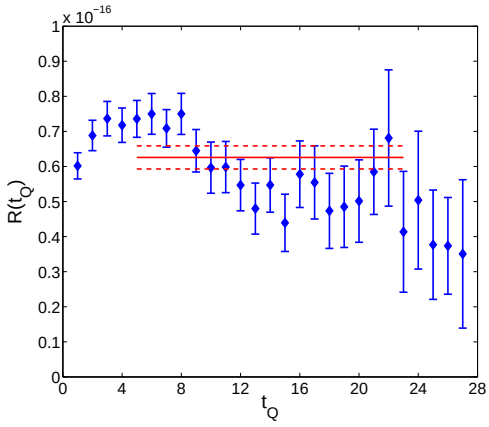

(a) $(27, 1)$ operator

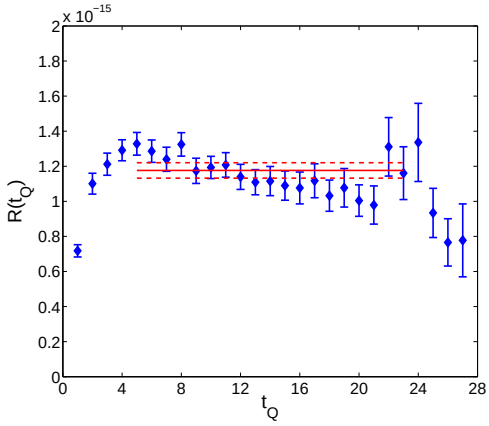

(b) $(8, 8)$ operator

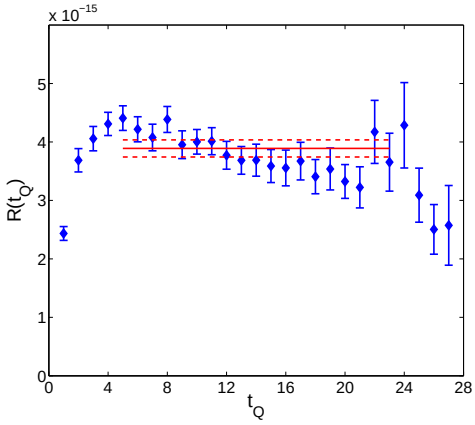

(c) $(8, 8)$mix operator

Figure B.2: *The ratios defined in Eq. (8.4) for* $p = \sqrt{2}\pi/L$*. The two-pion source is at* $t = 0$ *while the kaon source is at* $t_K = 28$*. The dashed line shows the error on the fit*

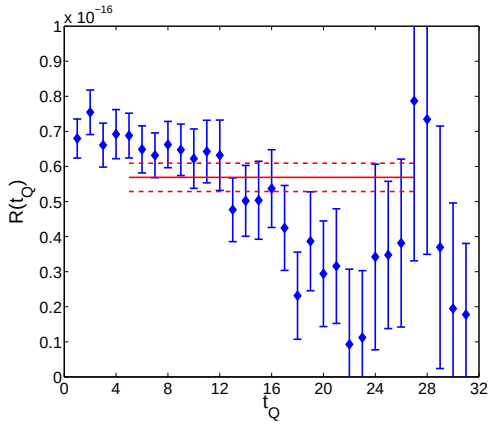

(a) $(27, 1)$ operator

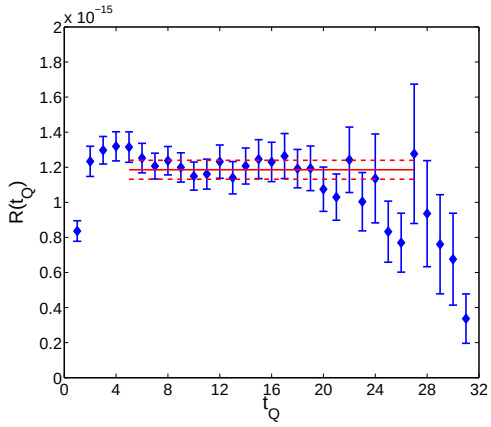

(b) $(8, 8)$ operator

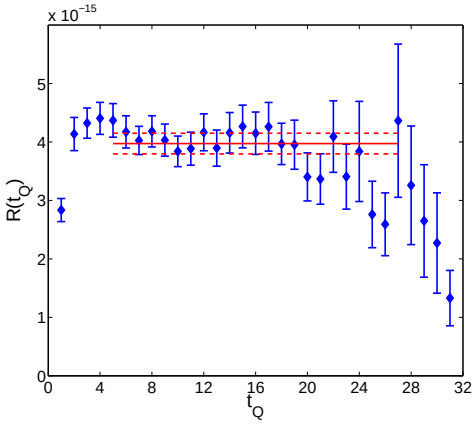

(c) $(8, 8)$mix operator

Figure B.3: *The ratios defined in Eq. (8.4) for* $p = \sqrt{2}\pi/L$. *The two-pion source is at* $t = 0$ *while the kaon source is at* $t_K = 32$. *The dashed line shows the error on the fit*

Bibliography

[1] J. F. Donoghue, E. Golowich, and B. Holstein, *Dynamics of the Standard Model*. Cambridge Monographs on Particle Physics, Nuclear Physics and Cosmology, 1994.

[2] C. Gattringer and C. B. Lang, *Quantum Chromodynamics on the Lattice*. Lecture Notes in Physics, 1999.

[3] **Particle Data Group** Collaboration, K. Nakamura et al., *The review of particle physics*, *J. Phys. G* **37** (2010) 075021.

[4] G. Buchalla, A. J. Buras, and M. E. Lautenbacher, *Weak decays beyond leading logarithms*, *Rev.Mod.Phys.* **68** (1996) 1125–1144, [hep-ph/9512380].

[5] M. Lightman, *Delta I Equals Three Halfs Kaon To Two Pion Decays Using Lattice Quantum Chromodynamics with Domain Wall Fermions*. PhD thesis, Columbia University, 2011.

[6] T. Blum, P. Boyle, N. Christ, N. Garron, E. Goode, et al., *The $K \to (\pi\pi)_{I=2}$ Decay Amplitude from Lattice QCD*, *Phys.Rev.Lett.* **108** (2012) 141601, [arXiv:1111.1699].

[7] T. Blum, P. Boyle, N. Christ, N. Garron, E. Goode, et al., *K to $\pi\pi$ Decay amplitudes from Lattice QCD*, *Phys.Rev.* **D84** (2011) 114503, [arXiv:1106.2714].

[8] E. Goode and M. Lightman, *Delta I=3/2 K to pi-pi decays with nearly physical kinematics*, *PoS* **LATTICE2011** (2011) 335, [arXiv:1111.4889].

[9] E. J. Goode and M. Lightman, $\Delta I = 3/2, Kto\pi\pi$ *Decays with a Nearly Physical Pion Mass*, *PoS* **LATTICE2010** (2010) 313, [arXiv:1101.2473].

[10] **RBC Collaboration, UKQCD Collaboration** Collaboration, M. Lightman and E. Goode, *Delta I=3/2, K to pi pi Decays with Light, Non-Zero Momentum Pions*, *PoS* **LAT2009** (2009) 254, [arXiv:0912.1667].

[11] J. Christenson, J. Cronin, V. Fitch, and R. Turlay, *Evidence for the 2 pi Decay of the k(2)0 Meson*, *Phys.Rev.Lett.* **13** (1964) 138–140.

[12] **NA31 Collaboration** Collaboration, H. Burkhardt et al., *First Evidence for Direct CP Violation*, *Phys.Lett.* **B206** (1988) 169.

[13] L. Gibbons, A. Barker, R. A. Briere, G. Makoff, V. Papadimitriou, et al., *Measurement of the CP violation parameter Re (epsilon-prime / epsilon)*, *Phys.Rev.Lett.* **70** (1993) 1203–1206.

[14] **NA48 Collaboration** Collaboration, V. Fanti et al., *A New measurement of direct CP violation in two pion decays of the neutral kaon*, *Phys.Lett.* **B465** (1999) 335–348, [hep-ex/9909022].

[15] **KTeV Collaboration** Collaboration, A. Alavi-Harati et al., *Measurements of direct CP violation, CPT symmetry, and other parameters in the neutral kaon system*, *Phys.Rev.* **D67** (2003) 012005, [hep-ex/0208007].

[16] M. Gaillard and B. W. Lee, *Delta I = 1/2 Rule for Nonleptonic Decays in Asymptotically Free Field Theories*, *Phys.Rev.Lett.* **33** (1974) 108.

[17] G. Altarelli and L. Maiani, *Octet Enhancement of Nonleptonic Weak Interactions in Asymptotically Free Gauge Theories*, *Phys.Lett.* **B52** (1974) 351–354.

[18] S. Li and N. H. Christ, *Chiral perturbation theory, $K \to \pi\pi$ decays and 2+1 flavor domain wall QCD*, *PoS* **LATTICE2008** (2008) 272, [arXiv:0812.1368].

[19] J. Laiho and R. S. Van de Water, *$K \to \pi\pi$ matrix elements from mixed action lattice QCD*, *PoS* **LATTICE2010** (2010) 312, [arXiv:1011.4524].

[20] **RBC Collaboration** Collaboration, T. Blum et al., *Kaon matrix elements and CP violation from quenched lattice QCD: 1. The three flavor case*, *Phys.Rev.* **D68** (2003) 114506, [hep-lat/0110075].

[21] **CP-PACS Collaboration** Collaboration, J. Noaki et al., *Calculation of nonleptonic kaon decay amplitudes from $K \to \pi$ matrix elements in quenched domain wall QCD*, *Phys.Rev.* **D68** (2003) 014501, [hep-lat/0108013].

[22] M. Golterman and E. Pallante, *Effects of quenching and partial quenching on penguin matrix elements*, *JHEP* **0110** (2001) 037, [hep-lat/0108010].

[23] M. Golterman and E. Pallante, *On the effects of (partial) quenching on penguin contributions to $K \to \pi\pi$*, *Phys.Rev.* **D69** (2004) 074503, [hep-lat/0212008].

[24] C. Aubin, N. Christ, C. Dawson, J. Laiho, J. Noaki, et al., *Systematic effects of the quenched approximation on the strong penguin contribution to epsilon-prime / epsilon*, *Phys.Rev.* **D74** (2006) 034510, [hep-lat/0603025].

[25] K. M. Watson, *The Effect of final state interactions on reaction cross-sections*, *Phys.Rev.* **88** (1952) 1163–1171.

[26] S. Gardner and G. Valencia, *The Impact of $|\Delta I = 5/2|$ transitions in $K \to \pi\pi$ decays*, *Phys.Rev.* **D62** (2000) 094024, [hep-ph/0006240].

[27] V. Cirigliano, J. F. Donoghue, and E. Golowich, *$K \to \pi\pi$ phenomenology in the presence of electromagnetism*, *Eur.Phys.J.* **C18** (2000) 83–95, [hep-ph/0008290].

[28] V. Cirigliano, A. Pich, G. Ecker, and H. Neufeld, *Isospin violation in epsilon-prime*, *Phys.Rev.Lett.* **91** (2003) 162001, [hep-ph/0307030].

[29] V. Cirigliano, G. Ecker, and A. Pich, *Reanalysis of pion pion phase shifts from $K \to \pi\pi$ decays*, *Phys.Lett.* **B679** (2009) 445–448, [arXiv:0907.1451].

[30] M. Kobayashi and T. Maskawa, *CP Violation in the Renormalizable Theory of Weak Interaction*, *Prog.Theor.Phys.* **49** (1973) 652–657.

[31] Y. Aoki, P. Boyle, N. Christ, C. Dawson, M. Donnellan, et al., *Non-perturbative renormalization of quark bilinear operators and B(K) using domain wall fermions*, *Phys.Rev.* **D78** (2008) 054510, [arXiv:0712.1061].

[32] C. Lehner and C. Sturm, *Matching factors for Delta S=1 four-quark operators in RI/SMOM schemes*, *Phys.Rev.* **D84** (2011) 014001, [arXiv:1104.4948].

[33] Y. Aoki, T. Blum, N. Christ, C. Cristian, C. Dawson, et al., *Domain wall fermions with improved gauge actions*, *Phys.Rev.* **D69** (2004) 074504, [hep-lat/0211023].

[34] D. B. Kaplan, *A Method for simulating chiral fermions on the lattice*, *Phys.Lett.* **B288** (1992) 342–347, [hep-lat/9206013].

[35] Y. Shamir, *Chiral fermions from lattice boundaries*, *Nucl.Phys.* **B406** (1993) 90–106, [hep-lat/9303005].

[36] V. Furman and Y. Shamir, *Axial symmetries in lattice QCD with Kaplan fermions*, *Nucl.Phys.* **B439** (1995) 54–78, [hep-lat/9405004].

[37] **RBC Collaboration, UKQCD Collaboration** Collaboration, D. J. Antonio et al., *Localization and chiral symmetry in three flavor domain wall QCD*, *Phys.Rev.* **D77** (2008) 014509, [arXiv:0705.2340].

[38] A. Hasenfratz, R. Hoffmann, and S. Schaefer, *Reweighting towards the chiral limit*, *Phys.Rev.* **D78** (2008) 014515, [arXiv:0805.2369].

[39] L. Del Debbio, L. Giusti, M. Luscher, R. Petronzio, and N. Tantalo, *QCD with light Wilson quarks on fine lattices. II. DD-HMC simulations and data analysis*, *JHEP* **0702** (2007) 082, [hep-lat/0701009].

[40] **LHPC Collaboration** Collaboration, J. Bratt et al., *Nucleon structure from mixed action calculations using 2+1 flavors of asqtad sea and domain wall valence fermions*, *Phys.Rev.* **D82** (2010) 094502, [arXiv:1001.3620].

[41] G. Martinelli, C. Pittori, C. T. Sachrajda, M. Testa, and A. Vladikas, *A General method for nonperturbative renormalization of lattice operators*, *Nucl.Phys.* **B445** (1995) 81–108, [hep-lat/9411010].

[42] C. Sturm, Y. Aoki, N. Christ, T. Izubuchi, C. Sachrajda, et al., *Renormalization of quark bilinear operators in a momentum-subtraction scheme with a nonexceptional subtraction point*, *Phys.Rev.* **D80** (2009) 014501, [arXiv:0901.2599].

[43] Y. Aoki, R. Arthur, T. Blum, P. Boyle, D. Brommel, et al., *Continuum Limit of B_K from 2+1 Flavor Domain Wall QCD*, *Phys.Rev.* **D84** (2011) 014503, [arXiv:1012.4178].

[44] M. Luscher, R. Sommer, P. Weisz, and U. Wolff, *A Precise determination of the running coupling in the SU(3) Yang-Mills theory*, *Nucl.Phys.* **B413** (1994) 481–502, [hep-lat/9309005].

[45] M. Luscher, P. Weisz, and U. Wolff, *A Numerical method to compute the running coupling in asymptotically free theories*, *Nucl.Phys.* **B359** (1991) 221–243.

[46] **RBC Collaboration, UKQCD Collaboration** Collaboration, R. Arthur and P. Boyle, *Step Scaling with off-shell renormalisation*, *Phys.Rev.* **D83** (2011) 114511, [arXiv:1006.0422].

[47] R. Arthur and P. A. Boyle, *Step Scaling with Off Shell Renormalization*, *PoS* **LATTICE2010** (2010) 244, [arXiv:1010.6140].

[48] P. Boyle and N. Garron, *Non-perturbative renormalization of kaon four-quark operators with nf=2+1 Domain Wall fermions*, *PoS* **LATTICE2010** (2010) 307, [arXiv:1101.5579].

[49] **RBC and UKQCD Collaborations** Collaboration, R. Arthur, P. Boyle, N. Garron, C. Kelly, and A. Lytle, *Opening the Rome-Southampton window for operator mixing matrices*, *Phys.Rev.* **D85** (2012) 014501, [arXiv:1109.1223].

[50] **RBC-UKQCD Collaboration** Collaboration, C. Allton et al., *Physical Results from 2+1 Flavor Domain Wall QCD and SU(2) Chiral Perturbation Theory*, *Phys.Rev.* **D78** (2008) 114509, [arXiv:0804.0473].

[51] **RBC Collaboration, UKQCD Collaboration** Collaboration, Y. Aoki et al., *Continuum Limit Physics from 2+1 Flavor Domain Wall QCD*, *Phys.Rev.* **D83** (2011) 074508, [arXiv:1011.0892].

[52] S. Li, *Kaon matrix elements and CP violation from lattice QCD with 2+1 flavors of domain wall fermions.* PhD thesis, Columbia University, 2008.

[53] M. Luscher, *Two particle states on a torus and their relation to the scattering matrix*, *Nucl.Phys.* **B354** (1991) 531–578.

[54] C. Kim, C. Sachrajda, and S. R. Sharpe, *Finite-volume effects for two-hadron states in moving frames*, *Nucl.Phys.* **B727** (2005) 218–243, [hep-lat/0507006].

[55] **CP-PACS Collaboration** Collaboration, T. Yamazaki et al., *$I = 2$ $\pi\pi$ scattering phase shift with two flavors of O(a) improved dynamical quarks*, *Phys.Rev.* **D70** (2004) 074513, [hep-lat/0402025].

[56] P. Boucaud, V. Gimenez, C. D. Lin, V. Lubicz, G. Martinelli, et al., *An Exploratory lattice study of $\Delta I = 3/2 K \to \pi\pi$ decays at next-to-leading order in the chiral expansion*, *Nucl.Phys.* **B721** (2005) 175–211, [hep-lat/0412029].

[57] C. Sachrajda and G. Villadoro, *Twisted boundary conditions in lattice simulations*, *Phys.Lett.* **B609** (2005) 73–85, [hep-lat/0411033].

[58] **RBC and UKQCD** Collaboration, R. Arthur et al., *Domain Wall QCD with Near-Physical Pions*, arXiv:1208.4412.

[59] L. Lellouch and M. Luscher, *Weak transition matrix elements from finite volume correlation functions*, *Commun.Math.Phys.* **219** (2001) 31–44, [hep-lat/0003023].

[60] W. Hoogland, S. Peters, G. Grayer, B. Hyams, P. Weilhammer, et al., *Measurement and Analysis of the pi+ pi+ System Produced at Small Momentum Transfer in the Reaction $\pi^+ p \to \pi^+ \pi + n$ at 12.5-GeV*, *Nucl.Phys.* **B126** (1977) 109.

[61] M. Losty, V. Chaloupka, A. Ferrando, L. Montanet, E. Paul, et al., *A Study of pi- pi- scattering from pi- p interactions at 3.93-GeV/c*, *Nucl.Phys.* **B69**

(1974) 185–204.

[62] A. Schenk, *Absorption and dispersion of pions at finite temperature*, *Nucl.Phys.* **B363** (1991) 97–116.

[63] G. Colangelo, J. Gasser, and H. Leutwyler, *$\pi\pi$ scattering*, *Nucl.Phys.* **B603** (2001) 125–179, [hep-ph/0103088].

[64] J. Laiho and A. Soni, *On lattice extraction of $K \to \pi\pi$ amplitudes to $O(p^4)$ in chiral perturbation theory*, *Phys.Rev.* **D65** (2002) 114020, [hep-ph/0203106].

[65] C. Aubin, J. Laiho, S. Li, and M. Lin, *$K \to \pi and K \to 0$ in 2+1 Flavor Partially Quenched Chiral Perturbation Theory*, *Phys.Rev.* **D78** (2008) 094505, [arXiv:0808.3264].

[66] **RBC Collaboration, UKQCD Collaboration** Collaboration, M. Lightman, *Physical matrix elements for $\Delta I = 3/2$ channel $K \to \pi\pi$ decays*, *PoS* **LATTICE2008** (2008) 273, [arXiv:0906.1847].

[67] C. Kim and C. Sachrajda, *$K \to (\pi\pi)_{I=2}$ decays and twisted boundary conditions*, *Phys.Rev.* **D81** (2010) 114506, [arXiv:1003.3191].

[68] A. J. Buras and D. Guadagnoli, *Correlations among new CP violating effects in Δ F = 2 observables*, *Phys.Rev.* **D78** (2008) 033005, [arXiv:0805.3887].

[69] A. J. Buras, D. Guadagnoli, and G. Isidori, *On epsilon$_K$ beyond lowest order in the Operator Product Expansion*, *Phys.Lett.* **B688** (2010) 309–313, [arXiv:1002.3612].

[70] **RBC and UKQCD Collaborations** Collaboration, N. H. Christ, *Computing the long-distance contribution to second order weak amplitudes*, *PoS* **LATTICE2010** (2010) 300.

[71] V. Cirigliano, J. F. Donoghue, E. Golowich, and K. Maltman, *Improved determination of the electroweak penguin contribution to ϵ'/ϵ in the chiral limit*, *Phys.Lett.* **B555** (2003) 71–82, [hep-ph/0211420].

[72] C. W. Bernard and A. Soni, *Review Of Weak Matrix Elements On The Lattice*, *Nucl. Phys. Proc. Suppl* **9** (1989).

[73] C. Dawson, G. Martinelli, G. Rossi, C. T. Sachrajda, S. R. Sharpe, et al., *New lattice approaches to the delta I = 1/2 rule*, *Nucl.Phys.* **B514** (1998) 313–335, [hep-lat/9707009].

[74] **RBC and UKQCD Collaborations** Collaboration, C. Allton et al., *2+1 flavor domain wall QCD on a (2 fm)^{83} lattice: Light meson spectroscopy with L(s) = 16*, *Phys.Rev.* **D76** (2007) 014504, [hep-lat/0701013].

[75] **RBC Collaboration, UKQCD Collaboration** Collaboration, T. Yamazaki, *On-shell Delta I = 3/2 kaon weak matrix elements with non-zero total momentum*, *Phys.Rev.* **D79** (2009) 094506, [arXiv:0807.3130].

[76] C. Kim, *$I = 2$ $\pi\pi$ scattering using G parity boundary condition*, *Nucl.Phys.Proc.Suppl.* **129** (2004) 197–199, [hep-lat/0311003].

[77] C.-h. Kim and N. H. Christ, *$K \to \pi\pi$ decay amplitudes from the lattice*, *Nucl.Phys.Proc.Suppl.* **119** (2003) 365–367, [hep-lat/0210003].

[78] Q. Liu, *Practical methods for a direct calculation of $\Delta I = 1/2$ K to $\pi\pi$ Decay*, *PoS* **LATTICE2011** (2011) 287, [arXiv:1110.2143].